Core-collapse supernovae and the equation of state

Kernkollaps-Supernovae und die Zustandsgleichung
Zur Erlangung des Grades eines Doktors der Naturwissenschaften (Dr. rer. nat.)
genehmigte Dissertation von M.Sc. Hannah Yasin, geb. in Frankfurt am Main
Tag der Einreichung: 18.12.2018, Tag der Prüfung: 06.02.2019
Darmstadt — D 17

1. Gutachten: Prof. Dr. Almudena Arcones Segovia
2. Gutachten: Prof. Achim Schwenk, Ph.D.

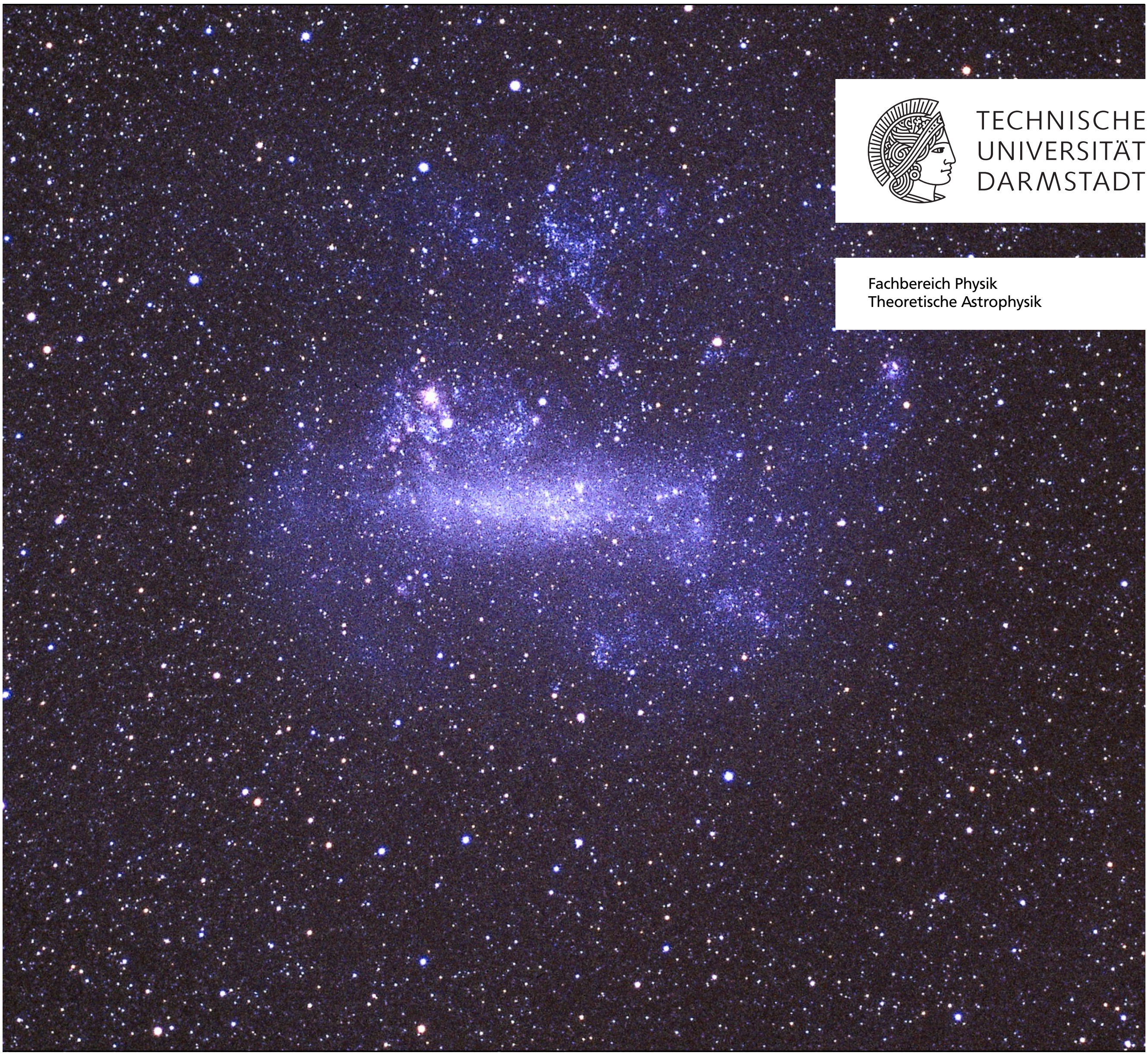

TECHNISCHE
UNIVERSITÄT
DARMSTADT

Fachbereich Physik
Theoretische Astrophysik

Core-collapse supernovae and the equation of state
Kernkollaps-Supernovae und die Zustandsgleichung

Genehmigte Dissertation von M.Sc. Hannah Yasin, geb. in Frankfurt am Main

1. Gutachten: Prof. Dr. Almudena Arcones Segovia
2. Gutachten: Prof. Achim Schwenk, Ph.D.

Tag der Einreichung: 18.12.2018
Tag der Prüfung: 06.02.2019

Darmstadt — D 17

Bitte zitieren Sie dieses Dokument als:
URN: urn:nbn:de:tuda-tuprints-88405
URL: http://tuprints.ulb.tu-darmstadt.de/8840

Dieses Dokument wird bereitgestellt von tuprints,
E-Publishing-Service der TU Darmstadt
http://tuprints.ulb.tu-darmstadt.de
tuprints@ulb.tu-darmstadt.de

Die Veröffentlichung steht unter folgender Creative Commons Lizenz:
Namensnennung – Keine kommerzielle Nutzung – Keine Bearbeitung 4.0 International
https://creativecommons.org/licenses/by-nc-nd/4.0/

मैत्री करुणा मुदितोपेक्षाणांसुखदुःख पुण्यापुण्यविषयाणां भावनातः चित्तप्रसादनम् ॥३३॥

Abstract

Core-collapse supernovae (CCSN) mark the end of the life of massive stars and are cosmic laboratories for physics at the extremes. Numerical simulations of these explosions are essential to understanding the complex mechanisms that are involved. All four fundamental interactions have to be taken into account, which requires the combined knowledge of astrophysics, nuclear physics, particle physics, and observations. A key ingredient in simulations is the equation of state (EOS), which determines the contraction behavior of the proto-neutron star (PNS), and thus impacts neutrino energies and explosion dynamics. However, the EOS for hot and dense matter is still not fully understood and CCSN simulations rely on phenomenological EOS models that differ in their underlying theory as well as nuclear physics input. In this thesis, we investigate the impact of uncertainties in the EOS in CCSN simulations. Further, we present an extension of the high-density EOS models to lower densities and temperatures, which enables us to perform long-time simulations of CCSN, following the shock evolution up to several seconds after bounce.

In the first part of this thesis, we present the first systematic study on the effect of different nuclear matter properties of the EOS in CCSN simulations. We investigate the impact of varying the nucleon effective mass, incompressibility, symmetry energy, and nuclear saturation point on the PNS contraction and its implication on the shock evolution. This allows us to examine possible reasons for differences in simulations with commonly used EOS models. We find that the contraction behavior of the PNS is mainly governed by the effective mass, which determines the thermal nucleonic contributions to the EOS. Larger effective masses result in smaller pressures at nuclear densities and a lower thermal index. This modifies the density, and thus the PNS contraction behavior, and consequently the shock propagation. We observe that variations in the symmetry energy impact the electron fraction, entropy, and temperature in the PNS interior. Our results suggest that differences among CCSN EOS mainly originate from their different nuclear matter properties. We verify that our models give reasonable modifications to the mass-radius relation of cold neutron stars and further investigate details of the explosion dynamics. Moreover, our EOS models are tested in different CCSN simulation codes, which yield similar results. Finally, we show that the choice of neutrino treatment impacts the PNS interior.

In the second part, we perform long-time CCSN simulations that follow the shock evolution several seconds after bounce, which requires a large simulation domain. To this end, we present a formalism for a high-density EOS transition to lower densities and temperatures. This formalism is tested for various EOS models and different progenitors in spherical symmetry. Additionally, we verify its functionality in cylindrical symmetry and for several neutrino transport schemes. With the transition, we perform the first long-time CCSN simulations in FLASH for exploding models, following the shock expansion up to five seconds after bounce. Different CCSN scenarios are investigated, varying the rotational profile and the explosion energetics by enhancing the neutrino energy deposition in the neutrino leakage scheme. We find that additional rotation and heating favors neutrino-driven winds, which impacts the diagnostic energy. Our results indicate that rotation decreases the mass accretion and reduces neutrino luminosities, as suggested in previous studies. Moreover, the results are compared to simulations performed with an M1 neutrino transport scheme. This allows us to analyze differences in the electron fraction, which need to be considered for future nucleosynthesis studies.

Cover picture: The Large Magellanic Cloud after SN1987A, Credit: ESO [1].

Zusammenfassung

Kernkollaps-Supernovae stellen das Lebensende massereicher Sterne dar und sind kosmische Labore für Physik unter extremen Bedingungen. Numerische Simulationen dieser Explosionen sind essentiell, um die zugrunde liegenden komplexen Mechanismen zu verstehen. Alle vier fundamentalen Wechselwirkungen müssen hierbei berücksichtigt werden, was das gebündelte Wissen der Astrophysik, Kernphysik, Teilchenphysik und Astronomie erfordert. Ein wesentlicher Bestandteil in Simulationen ist die Zustandsgleichung, welche das Kontraktionsverhalten des Protoneutronensterns bestimmt und somit die Neutrinoenergien und die Explosionsdynamik beeinflusst. Die Zustandsgleichung für die extremen Bedingungen in Supernovae ist jedoch noch nicht vollständig erforscht und Simulationen sind auf phänomenologische Zustandsgleichungsmodelle angewiesen, welche sich in ihrer zugrunde liegenden Theorie und in ihren kernphysikalischen Parametern unterscheiden. In dieser Dissertation untersuchen wir die Auswirkungen der Unsicherheiten in der Zustandsgleichung in Supernovasimulationen. Darüber hinaus stellen wir eine Erweiterung der Zustandsgleichungsmodelle hin zu niedrigeren Dichten und Temperaturen vor, die es uns ermöglicht, Langzeitsimulationen durchzuführen und die Ausbreitung der Stoßwelle mehrere Sekunden nach dem Kollaps zu verfolgen.

Im ersten Teil dieser Arbeit präsentieren wir die erste systematische Studie über die Wirkungsweise verschiedener Kernmaterieparameter der Zustandsgleichung in Supernovasimulationen. Wir untersuchen den Einfluss der effektiven Masse, der Inkompressibilität, der Symmetrieenergie und des nuklearen Sättigungspunktes auf die Kontraktion des Protoneutronensterns und die damit verbundenen Auswirkungen auf die Ausbreitung der Stoßwelle. Dies erlaubt es uns, mögliche Ursachen für Unterschiede in Simulationen mit häufig verwendeten Zustandsgleichungsmodellen zu ergründen. Wir beobachten, dass das Kontraktionsverhalten des Protoneutronensterns hauptsächlich von der effektiven Masse beeinflusst wird, welche die thermischen Beiträge zur Zustandsgleichung bestimmt. Eine größere effektive Masse führt zu einem geringeren Druck bei Kerndichten und einem niedrigeren thermischen Index. Dadurch wird die Dichte, und somit das Kontraktionsverhalten des Protoneutronensterns, und damit einhergehend die Stoßwellenausbreitung verändert. Weiterhin stellen wir fest, dass Variationen in der Symmetrieenergie den Elektronenanteil, die Entropie und die Temperatur im Inneren des Protoneutronensterns beeinflussen. Unsere Ergebnisse deuten darauf hin, dass Unterschiede zwischen Zustandsgleichungsmodellen hauptsächlich auf ihre verschiedenen Kernmaterieparameter zurückzuführen sind. Wir überprüfen, dass unsere Modelle sinnvolle Änderungen des Massen-Radius-Verhältnisses kalter Neutronensterne liefern und untersuchen außerdem Details der Explosionsdynamik. Darüber hinaus werden unsere Zustandsgleichungsmodelle in verschiedenen Simulationscodes getestet, mit vergleichbaren Ergebnissen. Abschließend zeigen wir, dass die Wahl des Neutrinotransportschemas das Innere des Protoneutronensterns beeinflusst.

Im zweiten Teil führen wir Langzeitsimulationen durch, welche die Ausbreitung der Stoßwelle mehrere Sekunden nach dem Kollaps verfolgen, was einen großen Simulationsbereich erfordert. Hierzu stellen wir einen Formalismus für eine Erweiterung unterschiedlicher Zustandsgleichungsmodelle für Kerndichten hin zu niedrigeren Dichten und Temperaturen vor. Dieser Formalismus wird für verschiedene Zustandsgleichungsmodelle und Vorläufersterne in sphärischer Symmetrie getestet. Darüber hinaus überprüfen wir die Funktionalität des Formalismus in zylindrischer Symmetrie und für verschiedene Neutrinotransportschemata. Mithilfe dieser Erweiterung führen wir die ersten Langzeitsimulationen in FLASH bis fünf Sekunden nach dem Kollaps durch. Es werden mehrere Supernovaszenarien untersucht, indem die Rotationsgeschwindigkeit des Sterns und die Explosionsenergetik variiert wird. Wir beobachten, dass erhöhte Neutrinoenergien und Rotationsgeschwindigkeiten neutrinogetriebene Winde begünstigen, was wiederum die Explosionsenergie beeinflusst. Unsere Ergebnisse deuten darauf hin, dass zusätzliche Rotation die Massenakkretion verringert und die Neutrinoleuchtkräfte reduziert, was auch bereits in früheren Arbeiten gezeigt wurde. Darüber hinaus vergleichen wir unsere Ergebnisse mit Simulationen, die mit einem M1-Neutrinotransportschema durchgeführt wurden. Dies ermöglicht es uns, Unterschiede im Elektronenanteil zu analysieren, die bei zukünftigen Nukleosyntheserechnungen berücksichtigt werden müssen.

Contents

List of Figures

List of Tables

"The nitrogen in our DNA, the calcium in our teeth, the iron in our blood, the carbon in our apple pies were made in the interiors of collapsing stars.
We are made of starstuff."
– Carl Sagan, Cosmos

1 Introduction

We know of more than a hundred elements that exist here on earth. The chemists Mendelejew and Meyer arranged them in the well known periodic table and people have studied them ever since. But where do these elements come from? While hydrogen, helium, and a small fraction of lithium were made in the Big Bang around 13.8 billion years ago, all elements heavier than hydrogen and helium are made in stars. It was Sir A. Eddington who first proposed in 1920 that nuclear fusion is the stellar energy source [2] and in 1939, H. Bethe provided detailed calculations that could explain the nuclear fusion reactions in the sun [3]. In stars that are at least ten times as heavy as the sun, central temperatures are high enough to produce elements up to iron. The fusion chain stops at iron, as it has the highest binding energy per nucleon and no further energy gain from fusion reactions is possible. But what about elements heavier than iron? In 1957, Burbidge *et al.* [4] and A. Cameron [5] presented different key processes that explained the nucleosynthesis of heavy elements via neutron capture processes, the so-called r-, and s-process (*r* for rapid neutron capture and *s* for slow neutron capture). However, the details in which astrophysical environments the specific nucleosynthesis processes take place are still topic of current research.

Stars are born in clouds of gas and dust. Their life span and stellar death depends on their initial birth mass, shown in Fig. 1.1. Lighter stars, like the sun, live for billions of years and become a white dwarf at the end of their life. Massive stars, at least ten times as heavy as the sun, live shorter than lighter stars, around millions of years. Most of them end their life as core-collapse supernovae, one of the most energetic events in the universe. Once a massive star has exhausted all its nuclear fuel, its core collapses under its own gravity. This collapse forms a neutron star and releases a shock wave that potentially disrupts the outer layers of the star, although a black hole formation is also possible. The explosion enriches the gas in the universe where new stars are formed. The possible existence of neutron stars, and the idea that they emerge from the collapse of massive stars, was proposed by Baade and Zwicky in 1934 [6], two years after the discovery of the neutron [7]. The observation of the first neutron star by J. Bell in 1968 [8], and the discovery of neutron stars in supernova remnants was considered observational proof that core-collapse supernovae are the birth places of neutron stars [9, 10].

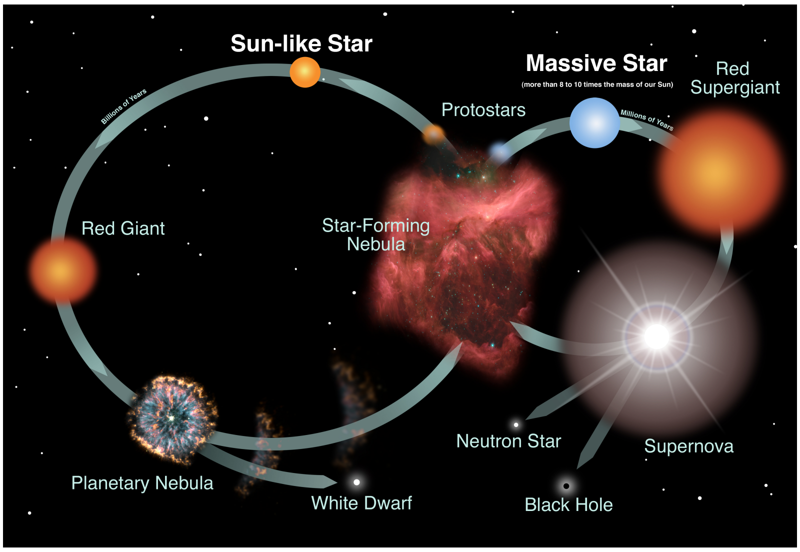

Figure 1.1.: Life cycles of light and massive stars, from Ref. [11].

The details how massive stars explode are still topic of current research and core-collapse supernova simulations are essential to understanding the underlying mechanisms. The modeling of these events is extremely complex, as all four fundamental forces, gravity along with the strong-, weak- and electromagnetic interaction, are relevant on completely different scales. The first supernova simulations were performed in spherical symmetry in the 1960s [12–14], where they observed that a "bounce" off the newly formed proto-neutron star releases a shock wave. But when the shock wave propagates outwards and heats the stellar material, almost all of its energy is drained and it stalls. In 1966, Colgate and White [15] proposed that neutrinos might play a crucial role for the explosion and in 1985, Bethe and Wilson [16] introduced the so-called "delayed neutrino-heating mechanism", where the shock wave is revived by neutrino energy deposition. The importance of neutrinos in supernovae was confirmed by the observation of a supernova in 1987, SN1987A, see Fig. 1.2, where 24 neutrinos were detected on earth [17]. Furthermore, asymmetries in the supernova remnant of SN1987A suggested that the explosion was not spherically symmetric, e.g., Refs. [18, 19]. This motivated the first multi-dimensional supernova simulations, which showed that multi-dimensional effects, such as convection and hydrodynamic instabilities, are highly relevant and can support the neutrino heating, e.g., Refs. [20–22]. Today, the field of core-collapse supernova simulations has advanced to three-dimensional simulations with detailed neutrino treatment and full general relativity (see, e.g., Refs. [23, 24]). The required resolution in simulations continues to challenge high-performance computers.

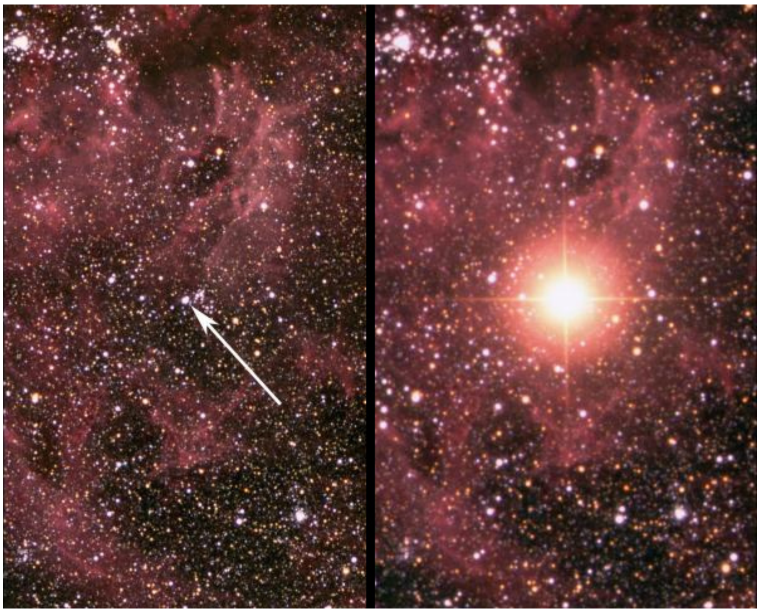

Figure 1.2.: Supernova 1987A after exploding in February 1987 (right), and an image taken before the explosion (left), from Ref. [25], modified.

The extreme conditions that occur in neutron stars also pose a challenge for nuclear physics. Here, densities exceed the nuclear saturation density and the strong interaction becomes highly relevant. As a result, the equation of state at such densities is still not fully understood and topic of current research (see, e.g., Ref. [26]). Constraints for the nuclear equation of state require a combined knowledge of modern theoretical calculations, nuclear experiments, and observations of neutron stars (see, e.g., Refs. [27–29]). The new multimessenger era that has started with the gravitational wave detection of neutron star mergers, and also black hole mergers, will further help to reduce uncertainties in the equation of state [30]. Currently, solely phenomenological equation of state models exist for supernova simulations, which differ in their underlying theory and nuclear physics input. The uncertainties in the nuclear matter properties affect the outcome of the supernova simulation significantly.

The aim of this thesis is to explore the role of the equation of state in core-collapse supernova simulations. We present the first systematic study on the impact of uncertainties in the equation of state in simulations. This allows us to examine possible reasons for differences in simulations with commonly used equations of state.
Further, we perform long-time supernova simulations which are essential to understand the conditions that are relevant for nucleosynthesis. Following the shock evolution several seconds after bounce requires a large simulation domain. To this end, we present an extension of the nuclear equation of state to lower densities and temperatures.

This thesis is structured as follows. An overview of core-collapse supernovae, including details of the explosion mechanism, is given in Chapter 2. The concept of core-collapse supernova simulations, as well as the numerical treatment of neutrinos is discussed in Chapter 3. We introduce fundamentals of the equation of state, as well as constraints and different equation of state models for hot and dense matter in Chapter 4. We investigate the impact of nuclear matter properties, and especially the role of the effective mass, in the equation of state in supernova simulations in Chapter 5. For the purpose of long-time simulations, we present a formalism for an equation of state transition from hot and dense matter to lower densities and temperatures in Chapter 6. Different long-time supernova simulation scenarios varying the rotational profile and the explosion energetics, by enhancing the neutrino energy deposition, are explored in Chapter 7. We conclude this thesis with a summary in Chapter 8 and provide technical simulation details in Appendix A.

2 Core-Collapse Supernovae

Core-collapse supernovae mark the end of the life of massive stars. They are one of the most energetic events in the universe and provide conditions extreme enough to produce elements up to silver, and maybe heavier.

The detailed mechanism of how these stars explode is still not fully understood and topic of current research. Over the last decades, advancements in hydrodynamic simulations of supernovae, as well as observations, have contributed to a better understanding of these events. Further, uncertainties in the underlying nuclear physics input, e.g., the equation of state, have been constrained significantly.

In this chapter, we introduce the different stages in the life of massive stars, from stellar evolution to supernova remnants. The final collapse and the explosion of the star are discussed in detail. We focus on the neutrino-driven explosion mechanism and shortly summarize recent findings from hydrodynamic simulations. This chapter follows Refs. [17, 31–33].

2.1 Stellar evolution

Stars spend their entire life in hydrostatic equilibrium. They are composed of gas, and for most of their life, hydrogen burning stabilizes them against gravity. The gas pressure P from the thermal movement of ions, electrons, and photons equilibrates the gravitational force [34]:

$$\frac{dP}{dr} = -\frac{GM(r)\rho(r)}{r^2}, \tag{2.1}$$

where M is the enclosed mass of the star, G represents the gravitational constant, and ρ denotes its density at radius r. The duration of the hydrogen burning depends on the mass of the star, which can be related to its central temperature T_c [31]:

$$\frac{T_c^3}{\rho_c} \propto M^2, \tag{2.2}$$

implying that heavier stars reach higher central temperatures. This results in a faster burning of the available hydrogen, which is also accelerated by the CNO cycle, and thus a shorter life. For a star of around $15\,M_\odot$, with $M_\odot$ being the mass of the sun, hydrogen burning lasts approximately 11 million years, with $T_c \sim 3.5 \cdot 10^7\,\mathrm{K}$ and $\rho_c \sim 5.8\,\mathrm{g\,cm^{-3}}$ [35].

The nuclear fusion in its center lets the star age. After millions of years, a large fraction of the hydrogen is converted to helium. At this point, the star is composed of a helium core, surrounded by an outer, still actively burning shell of hydrogen. The pressure support diminishes, due to the ongoing heat transfer, and is not able to counterbalance gravity any further. To compensate this loss, the star contracts. When the density in the core increases, matter sinks deeper into the gravitational potential and half of the freed gravitational potential energy is transformed into thermal energy (Virial theorem). The star becomes hotter.

If the temperature in the center is high enough ($\sim 2 \cdot 10^8\,\mathrm{K}$), the next burning stage can be reached. This means that the kinetic energy of ions is large enough to overcome the Coulomb barrier, enabling a fusion from helium to carbon and oxygen. The helium burning phase lasts shorter than the hydrogen burning (approximately 2 million years for a $15\,M_\odot$ star [35]). When the helium fuel is exhausted, pressure decreases and the star contracts again. Depending on its central temperature, either the next burning stage can be reached or the star settles into a new, stable configuration as a white dwarf, where the core is stabilized by the pressure of degenerate electrons, independent of the temperature.

Stars that are heavier than $10\,M_\odot$ reach central temperatures that are high enough ($> 3 \cdot 10^9\,\mathrm{K}$), such that further burning stages take place, up to silicon burning. This terminates nuclear fusion, as iron group nuclei have the highest binding energy per nucleon and no further energy gain from fusion reactions is possible. At this point, the star is composed of an iron core in the center, surrounded by outer layers from previous burning stages, shown in Fig. 2.1.

The duration of the burning phases becomes shorter with every stage, for several reasons. Firstly, the energy production rates increase as temperatures in the center become hotter. Also, there is less material available to burn. Finally, the gained energy per nucleon decreases. While hydrogen burning releases around 7 MeV per reaction, the total energy gain from helium to iron burning only yields 2 MeV [17]. The duration of silicon burning is shorter than a year (a few weeks for a star around 15 $M_\odot$) [35].

Additionally, neutrino losses start to play an important role. In the first burning stage, four protons are converted into one helium atom. This means that two protons have to be transformed into two neutrons, which releases two neutrinos. Neutrinos are weakly interacting particles that can leave the system without any further interaction. For hydrogen and helium burning, the energy loss due to neutrinos is relatively small. However, at late burning stages, when temperatures reach $\sim 10^9$ K, neutrino-antineutrino pairs become abundant. They are created in thermal processes and escape, representing the dominant energy loss.

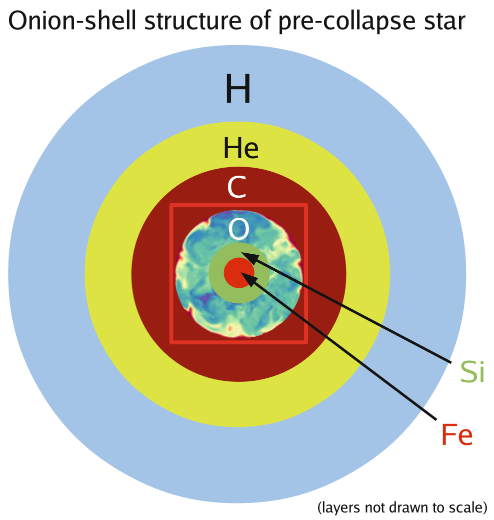

Figure 2.1.: Shell structure of a massive star, from Ref. [32].

Note that this picture of stellar evolution is not complete. Stellar evolution including stellar winds, that possibly occur for massive stars, as well as the effects of convection, rotation, and magnetic fields inside the star, is still topic current research. A review can be found, e.g., in Ref. [36].

2.2 Core collapse

At the end of their life, massive stars are composed of an iron core that is surrounded by lighter shells from previous burning stages, see Fig. 2.1. After millions of years, the fuel in the center of the star is exhausted and additional neutrino losses drain away energy from the system. At this point, pressure from degenerate electrons stabilizes the star against the gravitational collapse.

This configuration still resembles a hydrostatic equilibrium. The pressure is dominated by relativistic electrons with an adiabatic index of $\sim 4/3$. The baryonic mass of the degenerate core ranges between $1.3-2\,M_\odot$ with central densities around $\rho_c \sim 10^9-10^{10}\,\mathrm{g\,cm^{-3}}$, and central temperatures approximately equal to $T_c \sim 10^{10}$ K. The entropy is relatively small, $S_c \sim 1\,k_\mathrm{B}\,\mathrm{baryon}^{-1}$, where k_B is the Boltzmann constant, and the electron fraction Y_e, the number of electrons per baryon, ranges between $0.45-0.5$ [32]. The degenerate core is only stabilized as long as its mass does not exceed the critical Chandrasekhar limit M_ch [33]:

$$M_\mathrm{ch} \approx 1.4523\,(2\,Y_e)^2\,M_\odot\,. \tag{2.3}$$

Note that additional thermal pressure supports the degenerate core, so it may exceed the Chandrasekhar mass for a short period of time. The mass of the core is already close to the Chandrasekhar limit when nuclear burning stops, and additional silicon burning in the surrounding shell increases the mass of the core even further. Thus, the central density keeps growing and thus the Fermi energy of electrons rises. This makes them energetic enough to react with ions, denoted with mass number A and proton number Z, releasing an electron neutrino:

$$e^- + (A,Z) \rightarrow (A,Z-1) + \nu_e\,. \tag{2.4}$$

This electron capture reduces the electron fraction and the Chandrasekhar mass decreases, see Eq. (2.3). The neutrinos simply leave the system, causing a huge loss of energy for the star. Additionally, photodissociation of iron nuclei into alpha particles, neutrons, and protons decreases the pressure even further. The free protons that are released by the photodissociation can also capture electrons:

$$e^- + p \rightarrow n + \nu_e \,, \tag{2.5}$$

accelerating the energy loss. The star contracts to compensate the loss, which increases the central temperature, resulting in free nucleons and thus more electron captures on protons. The combined effects of the photodissociation and electron capture reduce the adiabatic index below 4/3, the critical value for gravitational stability.

The final contraction leads to the gravitational collapse of the star, see Fig. 2.2. The outer layers start falling inwards and the core shrinks to a few hundred kilometers within a tenth of a second, increasing the density in the center. Before the collapse, neutrinos are able to escape but as the density in the core increases, reaching values of $\rho \sim 10^{12}\,\mathrm{g\,cm^{-3}}$, neutrinos are trapped, see Fig. 2.3, conserving the entropy of the core.

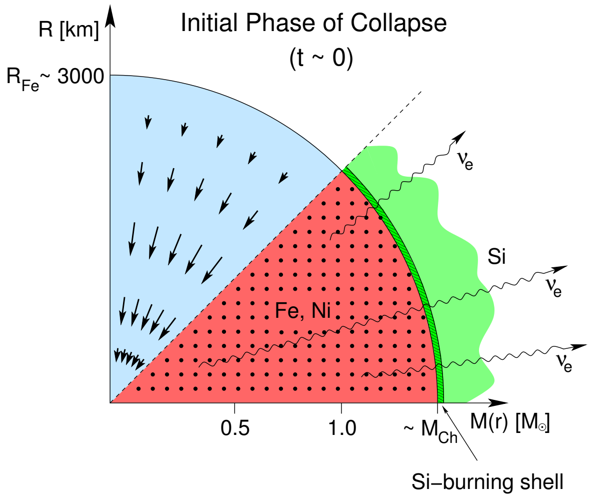

Figure 2.2.: Initial phase of collapse. The size of the iron core is a few thousands of kilometers, from Ref. [37].

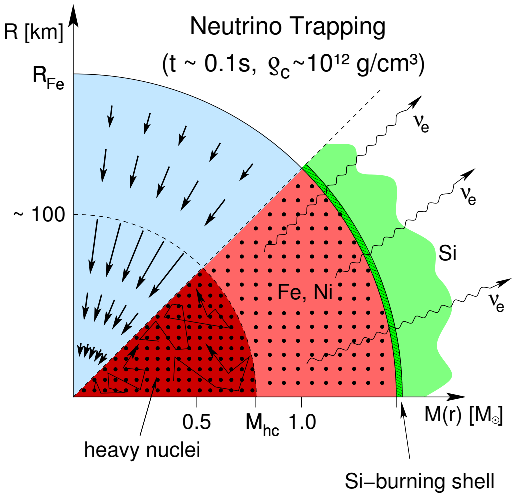

Figure 2.3.: The inner core shrinks, densities rise, neutrinos are trapped, from Ref. [37].

2.3 Bounce and shock formation

The collapse stops as soon as densities in the center reach nuclear saturation density $\rho_0 \sim 2.7 \cdot 10^{14}\,\mathrm{g\,cm^{-3}}$ [32]. Nuclei are packed so tightly that a phase transition to uniform matter (unbound neutrons, unbound protons, and electrons) occurs. The repulsive part of the strong interaction prevents further compression and a proto-neutron star (PNS) forms in the center of the star. The internal pressure of the free nucleons supports a new, stable configuration. The equation of state stiffens, due to the repulsive part of the strong interaction, and the adiabatic index rises again above 4/3. The PNS has a mass of around $0.5\,M_\odot$ and an electron fraction of roughly 0.25, as a result of previous neutrino losses [32].

Hoyle and Fowler speculated in 1960 [38] that the gravitational collapse would increase the temperature, such that enough energy could be released, triggering a successful explosion. Spherically symmetric core-collapse supernova (CCSN) simulations by Colgate and Johnson [12] and Colgate *et al.* [13] found that a "bounce" off the PNS releases a shock wave. As no further compression of the uniform matter inside the PNS is possible, matter bounces off the core, see Fig. 2.4, resulting in pressure waves that combine to a shock front that starts propagating outwards. However, when the shock meets matter that is still falling onto the PNS, almost all of its energy is drained, implying the supporting pressure behind the shock front vanishes. Inside the shock, temperature and entropy rise, creating highly energetic photons. These photons dissociate the iron group nuclei into neutrons and protons, which causes a huge energy loss. The kinetic energy of the shock is converted into the rest mass energy of the nucleons. Again, electron capture reactions can take place, see Eq. (2.5), creating a large amount of neutrinos. The neutrinos are trapped at first, but as the shock wave propagates further, densities decrease. The stellar medium becomes transparent for neutrinos, which then escape. This results in a so-called neutrino burst, see Fig. 2.5, within the first milliseconds after bounce. The photodissociation and the neutrino burst cause a significant energy loss for the shock. It stalls and turns into a so-called accretion shock, where matter is still falling onto the PNS. At this point, the shock is still located within the iron core.

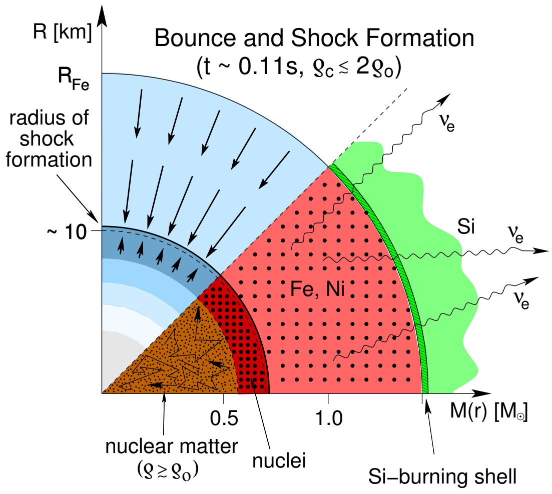

Figure 2.4.: Matter bounces off the core, resulting in a shock wave that starts propagating outwards, from Ref. [37].

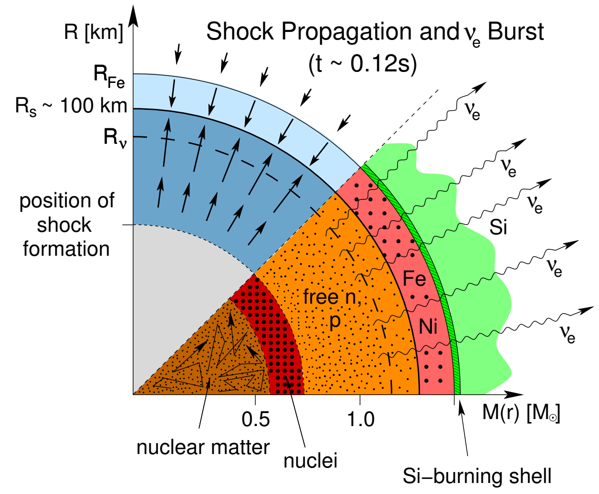

Figure 2.5.: The shock photodissociates iron group nuclei into free nucleons. Electron captures on protons result in a neutrino burst, from Ref. [37].

2.4 Explosion

The shock loses a significant amount of energy due to the photodissociation of iron group nuclei and the resulting burst of neutrinos. It stalls at approximately 100 − 200 km, turning into an accretion shock. The position of the shock R_s approximately follows [31]:

$$R_s \propto \frac{\left(L_\nu \langle E_\nu^2 \rangle\right)^{4/9} R_{\mathrm{NS}}^{16/9}}{\dot{M}^{2/3} M_{\mathrm{NS}}^{1/3}} \propto \frac{R_{\mathrm{NS}}^{8/3} (k_{\mathrm{B}} T_\nu)^{8/3}}{\dot{M}^{2/3} M_{\mathrm{NS}}^{1/3}} \propto \frac{L_\nu^{4/3}}{\dot{M}^{2/3} M_{\mathrm{NS}}^{1/3} (k_{\mathrm{B}} T_\nu)^{8/3}}, \tag{2.6}$$

where L_ν and $\langle E_\nu^2 \rangle$ denote the total neutrino energy luminosity and mean squared neutrino energy, respectively. Further, R_{NS} and M_{NS} represent radius and mass of the PNS. The accretion rate $\dot{M}$ refers to the accretion rate at the shock surface. Finally, T_ν depicts the neutrino temperature. The question how the shock wave can be revived is still under debate and topic of current research (see, e.g., Refs. [31, 39, 40]). In the following, we focus on the neutrino-heating mechanism.

In 1966, Colgate and White [15], and also D. Arnett [41], proposed that neutrinos might play a crucial role in the revival of the shock wave. They found that a large fraction of the gravitational binding energy of the PNS is carried away by neutrinos. This suggests that neutrinos can transport energy from the interior of the PNS. The reservoir of gravitational binding energy from the collapse can thus be transformed into internal and thermal energy. In 1985, Bethe and Wilson [16] introduced the so-called "delayed neutrino-heating mechanism". They observed late explosions, where the shock was revived because a fraction of neutrinos deposit energy behind the shock front. After bounce, neutrinos carry away energy from the PNS. The temperature in the postshock layer, the region between the surface of the PNS and the stalled shock, decreases as the density drops. The PNS cools by emitting neutrinos that can mostly escape without any further interaction. The cooling rate q_ν^- can be estimated via [32]:

$$q_\nu^- \approx 145 \cdot \left(\frac{k_{\mathrm{B}} T}{2\,\mathrm{MeV}}\right)^6, \tag{2.7}$$

where T denotes the temperature of the stellar medium. As the PNS cools, it contracts further. This hardens the neutrino spectra, meaning they have higher energies when streaming away from the so-called neutrinosphere, the position where neutrinos thermally decouple.

However, the stellar medium between the PNS and the shock radius is not completely transparent for neutrinos. A small fraction is absorbed by neutrons and protons in the postshock layer. This deposits energy, referred to as neutrino heating q_ν^+, which can be approximated via [32]:

$$q_\nu^+ \approx 110 \cdot \left(\frac{L_{\nu_e,52} \langle E^2_{\nu_e,15} \rangle}{r_7^2 \, s_{r,\nu_e}} Y_n + \frac{L_{\bar{\nu}_e,52} \langle E^2_{\bar{\nu}_e,15} \rangle}{r_7^2 \, s_{r,\bar{\nu}_e}} Y_p \right), \tag{2.8}$$

where $L_{\nu,52}$ and $\langle E^2_{\nu,15} \rangle$ denote the neutrino energy luminosity in units of $10^{52}\,\mathrm{erg\,s^{-1}}$ and mean squared neutrino energy divided by $(15\,\mathrm{MeV})^2$ respectively. The radius r_7 denotes the position in 10^7 cm and $s_{r,\nu}$ is the so-called flux factor, which is approximately $s_{r,\nu} \sim 0.25$ at the neutrinosphere. Further, $\bar{\nu}_e$ refers to the electron antineutrino, and Y_n and Y_p denote the neutron and proton fraction, respectively. A detailed derivation of the heating and cooling rates can be found, e.g., in Ref. [42].

Depending on the position between the PNS and the shock radius, either neutrino cooling or neutrino heating is dominant. This results from the different radial dependencies in Eqs. (2.7) and (2.8). Since the temperature follows a radial dependence with $T \propto r^{-1}$, cooling decreases with r^{-6}. Neutrino heating, however, follows a radial dependence of r^{-2}.

This allows the definition of a so-called gain radius, where heating and cooling are equal [16]. Up to the gain radius, cooling is dominant, indicated as the "cooling layer" in Fig. 2.6. Between the gain radius and the shock, heating dominates, referred to as "gain layer" in Fig. 2.6. Here, neutrinos deposit energy with a heating efficiency, $(q_\nu^+ - q_\nu^-)/L_\nu$, of roughly $5-10\,\%$ [32]. The gain radius R_g can be estimated as [16, 42]:

$$R_g \propto R_{\mathrm{NS}} \propto L_\nu^{1/2}/(k_{\mathrm{B}} T_\nu)^2 \,. \tag{2.9}$$

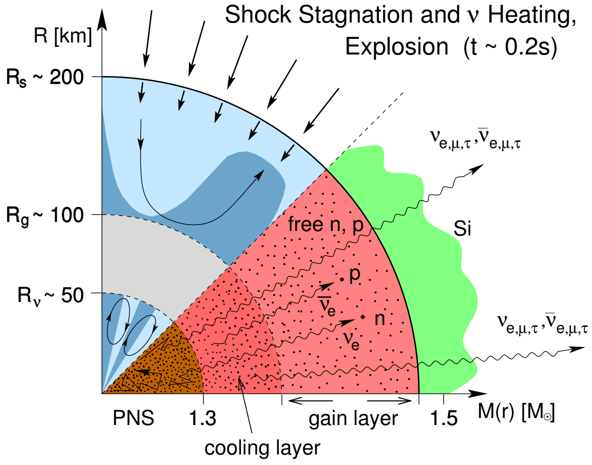

Figure 2.6.: The shock stalls, a fraction of neutrinos deposit energy behind the shock, from Ref. [37].

The success of the shock revival depends on whether enough material can be heated, while matter from the outer layers of the star is still being accreted onto the PNS. This also depends on the mass of the star, as heavier stars have higher mass accretion rates, which impedes the outward propagation of the stalled shock.

The residence time of matter in the gain layer can be estimated by a so-called advection time t_{adv} [31]:

$$t_{\mathrm{adv}} = \int_{R_g}^{R_s} \frac{dr}{|v_r|} \sim \beta \frac{R_s}{|v_0|} \sim \beta \frac{R_s^{3/2}}{\sqrt{GM_{\mathrm{NS}}}}, \tag{2.10}$$

where v_r represents the radial velocity of the matter accreted onto the PNS and β denotes the relative change of density at the shock radius R_s. The derivation follows from the mass infall rate $\dot{M} = 4\pi R_s^2 |v_0| \rho_0$ with $v_0 = -\sqrt{2GM_{\mathrm{NS}}/R_s}$. Simultaneously, higher mass accretion rates also enhance the neutrino luminosity. This intensifies the neutrino heating behind the shock, see Eq. (2.8). The time that is required to deposit energy t_{heat} is given by [31]:

$$t_{\mathrm{heat}} \sim \frac{|\epsilon_g|}{q_\nu^+} \propto \frac{M_{\mathrm{NS}} R_g}{L_\nu \langle \epsilon_\nu^2 \rangle}, \tag{2.11}$$

where ϵ_g denotes the gravitational energy near the gain radius. The energy deposition depends on neutrino luminosities and energies, but also on the duration that matter is exposed to neutrinos. A successful explosion requires that the heating time scale is shorter than the advection times scale, $t_{\text{adv}} > t_{\text{heat}}$, for a more detailed discussion see, e.g., Ref. [43]. This can also be formulated in terms of a critical luminosity $L_{\nu,c}$ [44], where $t_{\text{adv}} = t_{\text{heat}}$, see Refs. [31, 43]:

$$L_{\nu,c}(\dot{M}) \propto \beta^{-2/5} \dot{M}^{2/5} M_{\text{NS}}^{4/5} , \tag{2.12}$$

implying that a mass accretion rate that is too strong can prevent the shock expansion. If, however, the pressure behind the shock is larger than the ram pressure of the accreted matter, the shock can expand, resulting in a successful explosion. Note that Eqs. (2.6) – (2.12) are approximated expressions, a more detailed discussion can be found, e.g., in Refs. [32, 42, 43].

Matter expands as soon as it has absorbed enough energy to escape the gravitational potential of the PNS. The shock heats the stellar plasma, triggering explosive nucleosynthesis (see, e.g., Ref. [45]). The propagation of the shock wave may take days until it reaches the surface of the star and the supernova blast becomes visible [17].

The PNS cools by emitting neutrinos, and contracts to a few tens of kilometers. Simultaneously, matter is still accreted onto the surface of the PNS. Some of the emitted neutrinos deposit energy in the accreted matter. This can form a so-called neutrino-driven wind, an outflow that is driven from the surface of the PNS, which exhibits relatively high entropy [46]. As the wind expands and cools, neutrons and protons recombine to alphas and also to other possible nuclei (see, e.g., Refs. [47, 48]). A review for nucleosynthesis in neutrino-driven winds can be found, e.g., in Ref. [49].

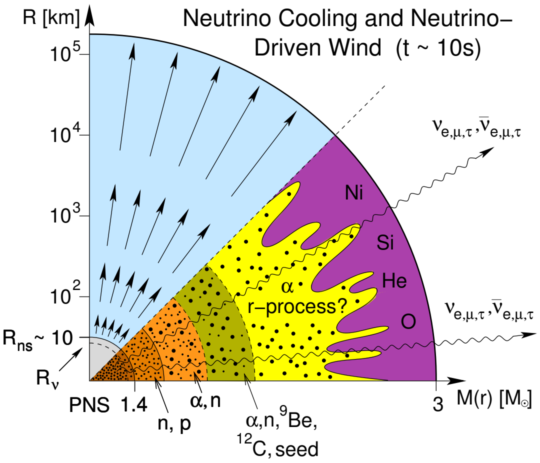

Figure 2.7.: The PNS cools by emitting neutrinos, a neutrino-driven wind can form, from Ref. [37].

2.5 Current status

The first CCSN simulations by Bethe and Wilson were modeled assuming spherical symmetry with a relatively simple treatment of neutrinos [14, 16]. However, modern one-dimensional simulations with a sophisticated neutrino treatment cannot reproduce the results from Bethe and Wilson, and only obtain successful explosions for light progenitors, i.e., electron-capture supernovae [50, 51], but not for stars heavier than 8.8 $M_\odot$ [31].

Asymmetries in the remnant of SN1987A, Fig. 2.8, suggest that spherical symmetry is broken during the explosion [18, 19]. A strong mixing of different elements is visible that can be related to hydrodynamic instabilities. Shortly after the observation of SN1987A, first simulations, assuming axisymmetry, were performed, e.g., Refs. [20–22]. These simulations demonstrated that multidimensional effects develop, i.e., a convective overturn, which can support a successful explosion. Energy deposition by neutrinos in the postshock layer creates a negative entropy gradient, which makes the heated layer convectively unstable, and thus Rayleigh-Taylor instabilities develop. Cold matter sinks onto the surface of the PNS, closer to the gain radius, where it can get heated by neutrinos. Simultaneously, hot matter is expanding away from the PNS, supporting the pressure behind the shock. Further, a so-called standing shock accre-

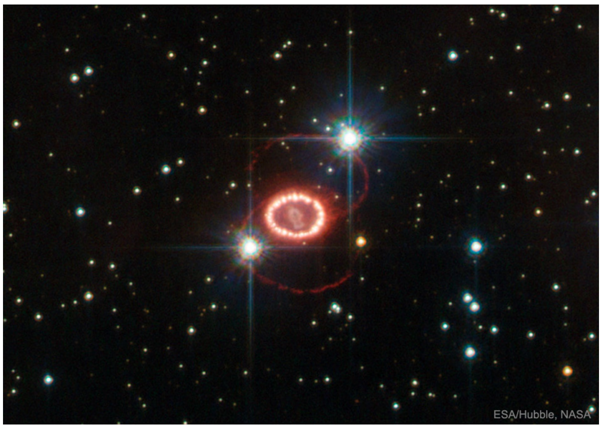

Figure 2.8.: SN1987A, from Ref. [52].

tion instability (SASI) [53–55] can grow between the shock and the PNS. This leads to a deformation and violent sloshing motion of the shock front that supports neutrino heating by enlarging the gain region. At first, these perturbations are relatively small, but as the shock expands, the perturbations grow, resulting in high asymmetries.

All of the mentioned multidimensional effects are not able to trigger a successful explosion by themselves, but yield additional, turbulent pressure behind the shock that supports the neutrino-driven explosion mechanism. Additionally, rotation and magnetic fields influence the explosion dynamics. However, modern three-dimensional simulations with a sophisticated neutrino transport have not been able to finally establish that the neutrino-heating mechanism is robust enough yet, especially for more massive progenitors (see, e.g., Ref. [32]). The question of how core-collapse supernovae explode stays a topic of intense research, where the coming years with new computational resources will give further insight into this field.

2.6 Supernova remnants

Proto-neutron stars are formed when massive stars collapse. They mostly cool by emitting neutrinos, and turn into a neutron star only a few seconds after their birth. However, the PNS may also collapse into a black hole. Recent studies suggest that there is no clear, linear correlation between the birth mass of the star and its remnant [56–58].

Neutron stars are compact objects with extremely high densities, around $5-10$ times nuclear saturation density [59]. Their radii are around 12 km and their masses range from $1.3 \sim 2\,M_\odot$ [59]. The possible existence of a neutron star was proposed shortly after the discovery of the neutron in 1932 [7]. Baade and Zwicky [6], and simultaneously L. Landau [60], hypothesized that such objects might exist. They speculated that neutron stars could be the remnants of supernovae. It was not until 1967 that J. Bell discovered the first neutron star [8]. Analyzing output data from radio telescopes, she found a series of regular pulses of a 1.3 s period, which come from a rapidly rotating neutron star, now known as "pulsar". The discovery of pulsars in the Crab nebula, Fig. 2.9, and Vela nebula, Fig. 2.10, both supernova remnants, is considered observational proof that neutron stars originate from core-collapse supernovae [9, 10].

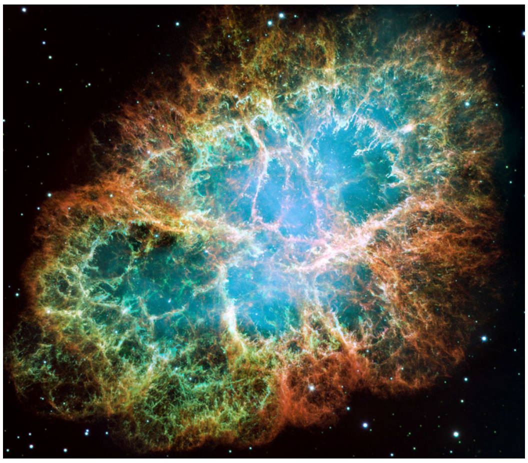

Figure 2.9.: Crab nebula, from Ref. [61].

Figure 2.10.: Vela nebula, from Ref. [62].

The detailed composition and structure of neutron stars, as well as the equation of state of dense matter, are still topic of current research (see, e.g., Ref. [59] and Sec. 4.3). In order to estimate density, mass, temperature, and composition of a neutron star, the relativistic stellar structure equations, the so-called Tolman-Oppenheimer-Volkoff equations [63], and the equation of state need to be solved consistently. This yields a mass-radius relation of neutron stars, which can be compared to observations (see, e.g., Refs. [26, 28, 29, 64, 65]). Especially masses of pulsars can be measured with great precision, but equally accurate measurements of neutron star radii have not been obtained so far. Altogether, neutron stars represent a challenge for astrophysicist, astronomers, and nuclear physicists. A more detailed discussion can be found in Chapter 4.

3 Simulating Core-Collapse Supernovae

Core-collapse supernova (CCSN) simulations are essential to understanding the complex mechanisms that are involved. This is a computationally demanding, numerical challenge, where all four fundamental interactions need to be considered. In addition, there are uncertainties in the underlying physics, e.g., the equation of state for hot and dense matter. Ideally, CCSN simulations are performed on a three-dimensional grid with high resolution, including general relativity, magnetic fields, rotation, and a full, seven-dimensional Boltzmann transport for neutrinos. Simulations that include all of these points have only become feasible recently, and still take several months of computing time on high-performance machines. It is therefore quite common to make certain approximations depending on the study that is conducted, e.g., a reduction of spatial dimensions or simplifications in the neutrino treatment. The scales that are modeled in CCSN simulations require sophisticated grid structures, with a resolution that is good enough to capture relevant features and moreover not produce any numerical artifacts, but simultaneously computationally feasible.

In this chapter, we briefly describe the concept of modeling CCSN simulations and introduce two different simulation codes, FLASH and GR1D, that are used throughout this thesis. We further discuss the treatment of neutrinos and give an overview of the schemes that are applied in this work. A brief description of equation of state tables, that are used in simulations, concludes this chapter.

3.1 Equations of hydrodynamics

Matter in core-collapse supernova (CCSN) simulations is treated as an ideal fluid and modeled using the Eulerian equations of hydrodynamics [66]. These equations can be derived from the Boltzmann equation, which describes the statistical behavior of a thermodynamic system, when imposing mass, momentum, and energy conservation, outlined in the following. Note that this section solely aims to give a rough overview, a detailed discussion and derivation can be found, e.g., in Ref. [67]. We employ the Newtonian formulation, based on Refs. [67–69].

Considering a particle distribution function $f(\boldsymbol{x},\boldsymbol{u},t)$, the probability of finding a particle with position $\boldsymbol{x}$ and velocity $\boldsymbol{u}$ in the phase space volume $\mathrm{d}^3\mathrm{x}\,\mathrm{d}^3\mathrm{u}$ at time t is given by $f(\boldsymbol{x},\boldsymbol{u},t)\,\mathrm{d}^3\mathrm{x}\,\mathrm{d}^3\mathrm{u}$. The distribution function is normalized such that the total number of particles N in the system is obtained via:

$$\int\int f(\boldsymbol{x},\boldsymbol{u},t)\,\mathrm{d}^3\mathrm{x}\,\mathrm{d}^3\mathrm{u} = N\,. \tag{3.1}$$

The Boltzmann equation characterizes the time evolution of the distribution function $f(\boldsymbol{x},\boldsymbol{u},t)$, including the diffusion of particles, an external force $\boldsymbol{g}$ acting on the particles, e.g., a gravitational potential with $\boldsymbol{g} = -\nabla\Phi$, and particle collisions:

$$\frac{\partial f}{\partial t} + \boldsymbol{u}\cdot\nabla f + \boldsymbol{g}\cdot\frac{\partial f}{\partial \boldsymbol{u}} = \left(\frac{\partial f}{\partial t}\right)_{\mathrm{coll}}, \tag{3.2}$$

where the collision term on the right hand side represents a multidimensional, nonlinear integral. Assuming that a quantity χ is conserved in an allowed collision processes, the integrated product $\chi\cdot(\partial f/\partial t)_{\mathrm{coll}}$ over $\mathrm{d}^3\mathrm{u}$ vanishes:

$$\int \chi\cdot\left(\frac{\partial f}{\partial t}\right)_{\mathrm{coll}} \mathrm{d}^3\mathrm{u} = 0\,. \tag{3.3}$$

The mass conservation equation is obtained by multiplying Eq. (3.2) with mass m and integrating over $\mathrm{d}^3\mathrm{u}$, which results in:

$$\frac{\partial}{\partial t}\int mf(\boldsymbol{x},\boldsymbol{u},t)\,\mathrm{d}^3\mathrm{u}+\nabla\cdot\int \boldsymbol{u}mf(\boldsymbol{x},\boldsymbol{u},t)\,\mathrm{d}^3\mathrm{u}=0\,, \tag{3.4}$$

where the third term in Eq. (3.2) vanishes assuming $f \to 0$ for $\boldsymbol{u} \to \infty$. The collisional term disappears due to local mass conservation, Eq. (3.3). Identifying the density as $\rho(\boldsymbol{x},t) = \int mf(\boldsymbol{x},\boldsymbol{u},t)\,\mathrm{d}^3\mathrm{u}$ and introducing the mass-weighted average of a quantity $\langle Q\rangle = \rho^{-1}\int Qmf(\boldsymbol{x},\boldsymbol{u},t)\,\mathrm{d}^3\mathrm{u}$, the mass conservation equation, or continuity equation, can be written as:

$$\frac{\partial\rho}{\partial t}+\boldsymbol{\nabla}\cdot(\rho\boldsymbol{v})=0\,, \tag{3.5}$$

with $\boldsymbol{v} = \langle\boldsymbol{u}\rangle$ being the mean fluid velocity. The continuity equation describes the change of density ρ due to a flow with velocity $\boldsymbol{v}$. Equivalently, the equations for momentum conservation (multiplying by $m\boldsymbol{u}$) and energy conversation (multiplying by $m\boldsymbol{u}^2$) with a gravitational potential read [68, 69]:

$$\frac{\partial\rho\boldsymbol{v}}{\partial t}+\boldsymbol{\nabla}\cdot(\rho\boldsymbol{v}\otimes\boldsymbol{v})+\nabla P=-\rho\nabla\Phi\,, \tag{3.6}$$

$$\frac{\partial\rho E}{\partial t}+\boldsymbol{\nabla}\cdot[(\rho E+P)\,\boldsymbol{v}]=-\rho\boldsymbol{v}\cdot\nabla\Phi\,, \tag{3.7}$$

where P denotes the pressure, Eq. (3.6) contains the dyadic product, and the gravitational potential is written on the right hand side. The total energy E is the sum of the internal energy e_{int} and kinetic energy:

$$E=e_{\mathrm{int}}+\frac{1}{2}\boldsymbol{v}^2\,. \tag{3.8}$$

In total, we obtain three equations with four unknowns, P, E, ρ, and $\boldsymbol{v}$. The system of equations is closed applying an equation of state (EOS), which provides a relation of pressure and energy, further discussed in Sec. 3.5 and Chapter 4. Writing the Eulerian equations of hydrodynamics in the so-called conservative form allows a clear representation of external source terms [70, 71]:

$$\frac{\partial}{\partial t}\boldsymbol{U}+\nabla\cdot\boldsymbol{F}=-\boldsymbol{S}\nabla\Phi\,, \tag{3.9}$$

with the state vector $\boldsymbol{U}$, flux vector $\boldsymbol{F}$, and source vector $\boldsymbol{S}$, that follow for the equations above as:

$$\boldsymbol{U}=\begin{bmatrix}\rho\\ \rho\boldsymbol{v}\\ \rho E\end{bmatrix}, \qquad \boldsymbol{F}=\begin{bmatrix}\rho\boldsymbol{v}\\ \rho\boldsymbol{v}\otimes\boldsymbol{v}+P\\ (\rho E+P)\boldsymbol{v},\end{bmatrix}, \qquad \boldsymbol{S}=\rho\begin{bmatrix}0\\ \mathbb{1}\\ \boldsymbol{v}\end{bmatrix}, \tag{3.10}$$

where $\mathbb{1}$ denotes the unitary matrix, and the external gravitational potential is contained in the source vector. In CCSN simulations, source terms can include, e.g., a gravitational field, neutrino momentum and energy, magnetic fields, viscosity.

The system of equations is a partial differential equation problem. We solve it on a numerical grid with specific boundary conditions, where initial data, e.g., from a pre-collapse progenitor star, is mapped and evolved. The details of the grid structure vary with different CCSN simulation codes, where some employ a relativistic formulation of the hydrodynamic equations (see, e.g., Refs. [72–74]). In the following, we introduce two different CCSN simulation codes, Newtonian and relativistic, that are used throughout this thesis.

3.2 FLASH

The FLASH code is a publicly available simulation code [75], originally based on Ref. [76], that is administrated by the FLASH center at the University of Chicago [77, 78]. It is a Newtonian, modular, parallelized code with adaptive mesh refinement that can model various compressible flow problems by solving the hydrodynamic equations.

In our simulation setup, neutrinos contribute to the momentum and energy conversation equations via:

$$\frac{\partial \rho \boldsymbol{v}}{\partial t} + \boldsymbol{\nabla} \cdot (\rho \boldsymbol{v} \otimes \boldsymbol{v}) + \nabla P = -\rho \nabla \Phi + Q_M \,, \tag{3.11}$$

$$\frac{\partial \rho E}{\partial t} + \boldsymbol{\nabla} \cdot [(\rho E + P)\, \boldsymbol{v}] = -\rho \boldsymbol{v} \cdot \nabla \Phi + Q_E + \boldsymbol{v} Q_M \,, \tag{3.12}$$

where Q_E and Q_M denote the neutrino energy and momentum source terms, respectively. Various neutrino treatments are implemented in FLASH, see Ref. [79] for more details and a comparison to other codes. The neutrino schemes utilized in this work are discussed in Sec. 3.4. Depending on the study, we include a gravitational potential that is either calculated as a Newtonian monopole, or approximated with an effective general relativity potential [80, 81], for details of the implementation see Ref. [82].

Stellar matter is composed of various types of nuclei, such that an additional conservation equation arises:

$$\frac{\partial \rho X_i}{\partial t} + \boldsymbol{\nabla} \cdot (\rho X_i \boldsymbol{v}) = R_i \,, \tag{3.13}$$

where X_i denotes the mass fraction of species i and R_i represents nuclear reaction rates. Conservation of mass requires that $\sum_i X_i = 1$ and $\sum_i R_i = 0$. If nuclear statistical equilibrium holds, the composition is determined by density, temperature, and the electron fraction Y_e, see also Sec. 4.2, and Eq. (3.13) becomes:

$$\frac{\partial \rho Y_e}{\partial t} + \boldsymbol{\nabla} \cdot (\rho Y_e \boldsymbol{v}) = Q_N \,, \tag{3.14}$$

with Q_N being an additional source term due to weak reactions.

The system of equations is solved on a Cartesian grid, and different kinds of solvers are available (see, e.g., Refs. [83–86]). The grid structure supports any geometry that can be translated onto a uniform grid, e.g., Cartesian, cylindrical, spherical. FLASH utilizes an adaptive mesh refinement (AMR) that is based on PARAMESH [87]. The AMR divides the computational domain into blocks, where each block contains a fixed amount of cells. If a finer resolution is needed, blocks are bisected into subblocks in each coordinate direction. The criteria for refinement or de-refinement can be modified by the user, e.g., based on density, pressure or entropy gradients. An illustration of the adaptive refinement is shown in Fig. 3.1.

Each block has a number of guard cells at each of its boundaries that is filled with data from the corresponding neighbor cells to evolve the hydrodynamic equations. At block intersections with different refinement levels, interpolations fill the additional guard cells. PARAMESH ensures conservation of fluxes entering or leaving the cell. In the case of different refinement levels at the boundary, the sum of all subfluxes is equal to the total flux. The inner and outer boundaries of the whole domain can be chosen to be reflective, e.g., for the proto-neutron star in the center, outflowing, or defined individually by the user.

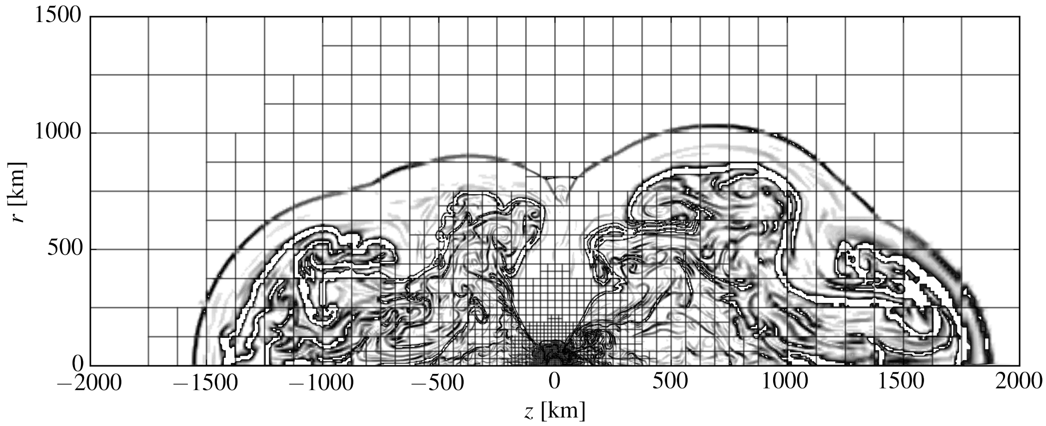

Figure 3.1.: Example for adaptive mesh refinement in a two-dimensional CCSN simulation. The resolution in the proto-neutron star region in the center is high, while the outer blocks that the shock has not reached yet are coarse. Thanks to Carlos Mattes for providing the plot routine.

3.3 GR1D

GR1D is a publicly available [88] CCSN simulation code [74, 89]. It is a spherically symmetric code that is based on a general relativistic (GR) formulation of the hydrodynamic equations. The GR framework allows to model the formation of a black hole. For readability, we chose $G = c = M_\odot = 1$ in this section.

The equations of hydrodynamics are solved on a radial-gauge, polar-slicing metric $g_{\alpha\beta} = \mathrm{diag}(-\alpha^2, X^2, r^2, r^2 \sin^2\theta)$, with the lapse $\alpha = \exp(\Phi)$ and $X = 1/[1-2m(r)/r]^{1/2}$. The metric is based on Refs. [90, 91], and the conservation equations are evolved using a piecewise parabolic method solver [83]. GR1D does not have adaptive mesh refinement, but the domain can be divided into two different subgrids with an equally spaced, high-resolution grid in the center of the star, and logarithmically spaced cells in the outer layers.

The relativistic hydrodynamic equations in the chosen metric and conservative formulation read [89]:

$$\frac{\partial}{\partial t}\boldsymbol{U} + \frac{1}{r^2}\frac{\partial}{\partial r}\left[\frac{\alpha r^2}{X}\boldsymbol{F}(\boldsymbol{U})\right] = -\boldsymbol{S}\,. \tag{3.15}$$

Note that in the relativistic case, $\boldsymbol{U}$, $\boldsymbol{F}$, and $\boldsymbol{S}$ take a metric-dependent form compared to Eq. (3.10). In the primitive form, the continuity equation is written as:

$$\frac{\partial D}{\partial t} + \frac{1}{r^2}\frac{\partial}{\partial r}\cdot\frac{\alpha r^2}{X}(Dv) = 0\,, \tag{3.16}$$

where $D = \rho W X$ with the Lorentz factor $W = 1/[1-v^2]^{1/2}$ and fluid velocity $v = W v^r$. This represents Eq. (3.5) with corresponding spherical coordinates and metric. The momentum evolution is calculated via:

$$\frac{\partial S^r}{\partial t} + \frac{\partial}{\partial r}\cdot\frac{\alpha r^2}{X}(S^r v + P) = \alpha X\left[(S^r v - \tau - D)(8\pi r P + m/r^2) + \frac{Pm}{r^2} + \frac{2P}{X^2 r}\right] + \alpha W(v Q_E + Q_M)\,, \tag{3.17}$$

with $S^r = \rho h W^2 v$, enthalpy $h = 1 + \epsilon + P/\rho$, and $\tau = \rho h W^2 - P - D$. Further, an additional geometrical source term arises on the right hand side compared to Eq. (3.6). The energy conservation equation reads:

$$\frac{\partial \tau}{\partial t} + \frac{\partial}{\partial r}\cdot\frac{\alpha r^2}{X}[(\tau + P)\,v] = \alpha W(Q_E + v Q_M)\,. \tag{3.18}$$

The evolution of the electron fraction is written as:

$$\frac{\partial DY_e}{\partial t} + \frac{\partial}{\partial r} \cdot \frac{\alpha r^2}{X} \left(DY_e v \right) = Q_N \,. \tag{3.19}$$

The system of equations is closed with an EOS, discussed in Sec. 3.5. The code offers two different neutrino treatments, either a neutrino leakage [89] with a deleptonization from Ref. [92], or an M1 neutrino transport scheme [74], see also Sec. 3.4. GR1D and FLASH are discussed in a global comparison of six CCSN simulation codes from different groups, see Ref. [93], where considerable agreement among the various codes is found.

3.4 Neutrinos

Neutrinos play a crucial role in CCSN. They carry a significant amount of the gravitational energy, cool the proto-neutron star, and possibly revive the stalled shock wave. Neutrinos are solely subject to the weak interaction, and for densities below $\rho \sim 10^{12}\,\mathrm{g\,cm^{-3}}$, they can escape the supernova plasma with almost no interaction. Inside the proto-neutron star, neutrinos are trapped and local thermal equilibrium with matter can be assumed. We consider neutrinos to be massless particles.

The different conditions that are encountered in CCSN make it quite challenging to model the propagation of neutrinos. The seven-dimensional neutrino distribution function $f_\nu(x^\mu, p^\alpha)$ has to be evolved for all neutrino species, which includes electron ν_e, muon ν_μ, and tau ν_τ neutrinos with their corresponding antiparticles. The distribution function depends on time ($x^0 = t$), three-dimensional spatial points ($x^j = \boldsymbol{x}$), and the neutrino energy and propagation angles ($p^0 = \epsilon_\nu = |\boldsymbol{p}|$ and $p^k = \boldsymbol{p}$). The evolution of the neutrino distribution function is described by the relativistic collisional Boltzmann transport equation [74, 94], see also Sec. 3.1:

$$p^\alpha \left(\frac{\partial f_\nu}{\partial x^\alpha} - \Gamma^\beta_{\alpha\gamma} p^\gamma \frac{\partial f_\nu}{\partial p^\beta} \right) = \left(\frac{d f_\nu}{d t} \right)_{\mathrm{coll}} , \tag{3.20}$$

where Γ denotes the Christoffel symbols. The collision term is computed differently, depending on whether neutrinos are diffusing out of the proto-neutron star or escaping the system. The treatment of the transition from the trapped regime to the free-streaming region is highly relevant, as it influences neutrino rates and thus the electron fraction.

Neutrino interactions with matter include neutrino absorption, emission, and scattering reactions. An overview is shown in Fig. 3.2. Charged current reactions dominate for electron type neutrinos, since the corresponding lepton that is created, the electron, is much lighter compared to the muon or tau. Therefore, the required threshold energy of the electron type neutrino is smaller. Neutrino scattering, as well as thermal pair processes, are relevant for all neutrino flavors. In our simulation setup, neutrino-neutrino reactions as well as neutrino oscillations are not included.

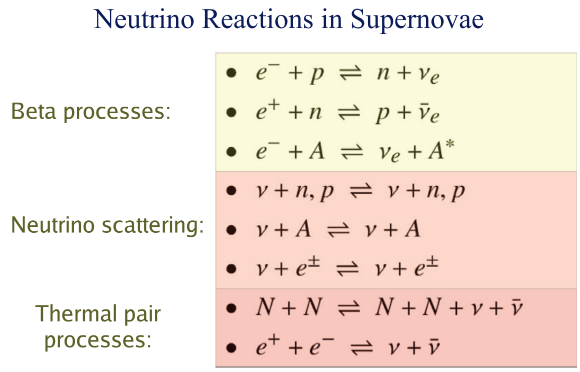
Neutrino Reactions in Supernovae

Beta processes:	• $e^- + p \rightleftharpoons n + \nu_e$ • $e^+ + n \rightleftharpoons p + \bar{\nu}_e$ • $e^- + A \rightleftharpoons \nu_e + A^*$
Neutrino scattering:	• $\nu + n, p \rightleftharpoons \nu + n, p$ • $\nu + A \rightleftharpoons \nu + A$ • $\nu + e^\pm \rightleftharpoons \nu + e^\pm$
Thermal pair processes:	• $N + N \rightleftharpoons N + N + \nu + \bar{\nu}$ • $e^+ + e^- \rightleftharpoons \nu + \bar{\nu}$

Figure 3.2.: Neutrino absorption, emission, and scattering processes, from Ref. [95], modified.

Neutrino treatments in simulations range from solving the full Boltzmann transport equation, e.g., Refs. [96–98], applying moment expansion schemes, e.g., Refs. [74, 99], to the isotropic diffusion source approximation IDSA [100], and neutrino leakage schemes, e.g., Refs. [42, 101, 102], with or without energy dependence. In energy dependent models, the distribution of neutrino energies is discretized in "energy bins". This means that the Boltzmann equation, Eq. (3.20), has to be evolved for each energy bin. Energy independent schemes, also referred to as "gray schemes", consider one average neutrino energy. This average neutrino energy is usually inaccurate and high-energy neutrinos in the gain region are overestimated. Leakage schemes, although not full transport methods, capture the qualitative behavior of neutrinos and are computationally advantageous. We introduce a moment expansion scheme, M1, and a gray neutrino leakage in the following.

3.4.1 M1

The relativistic collisional Boltzmann transport equation, Eq. (3.20), implies the evolution of a seven-dimensional distribution function with a non-trivial collision term, on top of the hydrodynamic modeling. This is a computationally demanding task that, in three-dimensional simulations, has only become feasible in recent years (see, e.g., Refs. [24, 73, 103, 104]). The M1 transport scheme reduces the full Boltzmann transport by removing the full angular dependence in the neutrino distribution function, expanding it as a series of moments. In the following, we discuss the concept of M1 in spherical symmetry, considering an expansion in the zeroth and first moment. A full overview can be found, e.g., in Refs. [105, 106]. We consider neutrinos to be massless particles and express the neutrino distribution function f_ν in Eq. (3.20) in terms of a specific intensity $\mathcal{I} = \epsilon_\nu^3 c/(hc)^3 f_\nu$, with speed of light c and Planck constant h. In spherical symmetry, and without an external force field, the transport equation is reduced to [80, 107–109]:

$$\frac{1}{c}\frac{\partial}{\partial t}\mathcal{I} + \mu\frac{\partial}{\partial r}\mathcal{I} + \frac{1-\mu^2}{r}\frac{\partial}{\partial \mu}\mathcal{I} = \mathcal{C} = \kappa(\mathcal{S}-\mathcal{I}), \tag{3.21}$$

where $\mu = \cos\theta$ is the angle between the propagation and radial direction r. The collision term $\mathcal{C}$ is expressed in terms of the neutrino opacity κ and source function $\mathcal{S}$. The neutrino distribution function f_ν, or in our case $\mathcal{I}$, is expanded as a series of moments, denoted as $\mathcal{J},\mathcal{H},\mathcal{K},\mathcal{L},\ldots$, in spherical symmetry leading to [80]:

$$\{\mathcal{J},\mathcal{H},\mathcal{K},\mathcal{L},\ldots\}(r,\epsilon,t) = \frac{1}{2}\int_{-1}^{+1} d\mu\,\mu^{\{0,1,2,3,\ldots\}}\mathcal{I}(r,\epsilon,\mu,t), \tag{3.22}$$

where the angular dependence μ vanishes by taking the integral. This reduces the degrees of freedom, in the case of spherical symmetry from four to three dimensions. Expressing the specific intensity $\mathcal{I}$ as a series of the first two moments and performing a solid angle integration, Eq. (3.21) becomes:

$$\frac{1}{c}\frac{\partial}{\partial t}\mathcal{J} + \frac{1}{r^2}\frac{\partial}{\partial r}(r^2\mathcal{H}) = C^0 = \kappa(\mathcal{S}-\mathcal{J}), \qquad 0^{\text{th}} \text{ moment} \tag{3.23}$$

$$\frac{1}{c}\frac{\partial}{\partial t}\mathcal{H} + \frac{1}{r^2}\frac{\partial}{\partial r}(r^2\mathcal{K}) + \frac{3\mathcal{K}-\mathcal{J}}{r} = C^1 = -\kappa\mathcal{H}. \qquad 1^{\text{st}} \text{ moment} \tag{3.24}$$

Note that the equation for the n^{th} moment includes the $n^{\text{th}}+1$ moment. The collision term on the right hand side is related to the neutrino source terms, Q_E and Q_M, in the hydrodynamic equations via [80]:

$$Q_E = -4\pi\int_0^\infty d\epsilon C^0(\epsilon), \qquad \text{and} \qquad Q_M = -\frac{4\pi}{c}\int_0^\infty d\epsilon C^1(\epsilon). \tag{3.25}$$

The moments $\mathcal{J},\mathcal{H},\mathcal{K}$ in Eqs. (3.23) – (3.24) are the fluid-frame moments of the neutrino. To include the source terms in the conservation equations, they need to be related to the laboratory frame, where we denote the corresponding neutrino moments with E,F,P. In spherical symmetry, the zeroth neutrino moment in the laboratory frame in GR1D and FLASH, or any other similar metric, follows from Eq. (3.23) [74, 82]:

$$\frac{\partial}{\partial t}E + \frac{1}{r^2}\frac{\partial}{\partial r}[\alpha r^2 F^r] - \partial_\epsilon[\epsilon(R^t + O^t)] = G^t + C^0, \tag{3.26}$$

with the lapse $\alpha = \exp(\Phi)$. The superscript t denotes the zeroth component, i.e., the time component, of the vectors. The term $\partial_\epsilon[\epsilon(R^t + O^t)]$ appears due to redshift and observer motions, and G^t is a geometrical source term. Neighboring energy bins are coupled explicitly in GR1D and FLASH.

In the laboratory frame, the collisional term C^0 in Eq. (3.23), with $\mathcal{S} = \eta/\kappa$, is related via [74, 82]:

$$C^0 = \alpha\big(W[\eta - \kappa_a \mathcal{J}] - [\kappa_a + \kappa_s]\mathcal{H}^t\big)\,, \tag{3.27}$$

where W denotes the Lorentz factor and η denotes the neutrino emissivity. Further, κ_a and κ_s represent the neutrino absorption and scattering opacities, respectively. To solve Eq. (3.26), the fluid frame energy density $\mathcal{J}$ and momentum density $\mathcal{H}$ have to be expressed in terms of E and F. However, the n^{th} moment equation contains the $n^{\text{th}} + 1$ moment, in the case of Eq. (3.24) the moment $\mathcal{K}$, and a closure is necessary. In GR1D and FLASH, the closure is taken from Refs. [106, 110], with an interpolation between the optically thick and thin regime:

$$\mathcal{K}^{ij} = \frac{3(1-\chi)}{2}\mathcal{K}^{ij}_{\text{thick}} + \frac{3\chi - 1}{2}\mathcal{K}^{ij}_{\text{thin}}\,, \tag{3.28}$$

where different assumptions can be made for $\mathcal{K}_{\text{thick}}$ and $\mathcal{K}_{\text{thin}}$. In the optically thick regime, radiation is isotropic, i.e., $\mathcal{K}^{ij}_{\text{thick}} = \mathcal{J}/(3(1+W^2v^2))$ with radial velocity v. In the free streaming regime, $\mathcal{K}^{ij}_{\text{thin}} = \mathcal{J}(\mathcal{H}^i\mathcal{H}^j/\mathcal{H}^2)$. Further, χ is taken to be the Minerbo closure [111, 112]:

$$\chi = \frac{1}{3} + \frac{2}{15}(3f^2 - f^3 + 3f^4)\,, \qquad \text{with} \qquad f = (\mathcal{H}^2/\mathcal{J}^2)^{1/2}\,. \tag{3.29}$$

A discussion of closures can be found, e.g., in Ref. [113]. The neutrino energy source term Q_E enters the Eulerian equations of hydrodynamics, here given in discretized form [82]:

$$\Delta[\rho E] = \Delta[\rho e_{\text{int}}] + \Delta[\rho e_{\text{kin}}] = -4\pi\alpha\Delta t\sum_{\nu,\epsilon}\Delta\epsilon\big(W[\eta - \kappa_a\mathcal{I}] - [\kappa_a + \kappa_s]\mathcal{H}^t\big)\,, \tag{3.30}$$

which corresponds to inserting Eq. (3.27) in Eq. (3.25). Note that the energy deposition by neutrinos is included in the internal energy via $e_{\text{int}} = e_{\text{int}} + Q$. For additional computational benefit, neutrino opacities in GR1D and FLASH are not calculated within the simulation, but interpolated using neutrino opacity tables. These tables depend on the EOS, and routines to create them are available from Ref. [114], see Ref. [74]. The neutrino cross sections in the routines are taken from Refs. [99, 115, 116].

3.4.2 Leakage

The gray neutrino leakage scheme does not evolve the neutrino distribution function and cannot be considered a transport method. Local neutrino energies and emission rates are estimated, and the emitted energy is then subtracted from the system. Leakage schemes do not obtain neutrino-heating self-consistently and require an additional treatment of the deleptonization during collapse. However, they reproduce global neutrino effects and are computationally beneficial.

The energy emission rates $Q_\nu = d\epsilon_\nu/dt$ and lepton emission rates $R_\nu = d(Y_e)_\nu/dt$ are divided into two regions. A diffusive regime, where neutrinos are trapped and escape on a diffusion timescale, and a free streaming regime. Effective emission rates $S_{\nu,\text{eff}}$ are interpolated via [42, 117]:

$$S_{\nu,\text{eff}} = \frac{S_{\nu,\text{free}} \times S_{\nu,\text{diff}}}{S_{\nu,\text{free}} + S_{\nu,\text{diff}}}\,, \tag{3.31}$$

where $S_\nu = \{Q_\nu, R_\nu\}$. In the diffusive regime, the optical depth of neutrinos needs to be estimated to find the location of the neutrinosphere, i.e., the position where neutrinos decouple from matter. This includes absorption reactions, $\nu_e + n \rightarrow e^- + p$ and $\bar{\nu}_e + p \rightarrow e^+ + n$, and elastic scattering reactions. For both regimes, emission rates from electron capture on protons, and positron capture on neutrons (the first two equations in Fig. 3.2) are included, as well as electron-positron annihilation and nucleon-nucleon bremsstrahlung. The rates are calculated from the local thermodynamic properties of matter.

As leakage schemes cannot reproduce neutrino heating, it is common to include a heating term Q_ν via [42, 117]:

$$Q_\nu = f_{\mathrm{heat}} \frac{L_\nu(r)}{4\pi r^2} \left\langle \frac{1}{F_\nu} \right\rangle \sigma_\nu \frac{\rho \cdot X_{\mathrm{n,\,p}}}{m_u} e^{-2\tau_\nu}\,, \tag{3.32}$$

where ν can either be ν_e or $\bar{\nu}_e$. The factor f_{heat} denotes a so-called heating factor that allows to enhance the neutrino energy deposition to trigger an artificial explosion. Further, L_ν represents the neutrino luminosity and F_ν is the flux factor that takes the propagation direction of the neutrino into account ($F_\nu \sim 0.25$ at the neutrinosphere). The term $\rho \cdot X_{\mathrm{n,\,p}}/m_u$, with atomic mass unit m_u, calculates the number density of either neutrons in the case of ν_e, or protons for $\bar{\nu}_e$. Heating in the diffusive regime is reduced using the optical depth τ_ν. The cross section σ_ν is simplified as [117]:

$$\sigma_\nu = \frac{1 + 3g_A^2}{4} \sigma_0 \frac{\langle \epsilon^2 \rangle_\nu}{m_e^2 c^4} B_\nu\,, \tag{3.33}$$

where g_A denotes the axial vector coupling constant and $\sigma_0 \sim 2.76 \cdot 10^{-44}\,\mathrm{cm}^2$. The mean squared energies of the neutrinos $\langle \epsilon^2 \rangle$ are taken at the neutrinosphere, m_e is the mass of the electron, and B_ν considers final state blocking. For a full expression of the neutrino cross sections see, e.g., Ref. [116].

In the hydrodynamic equations, energy conservation includes the neutrino heating term via [117]:

$$\frac{\partial \rho E}{\partial t} + \nabla \cdot [(\rho E + P)\,\boldsymbol{v}] = -\rho \boldsymbol{v} \cdot \nabla \Phi + Q_\nu\,. \tag{3.34}$$

The leakage schemes in FLASH and GR1D follow the original work by Refs. [42, 102, 118]. The neutrino leakage in GR1D is implemented by Ref. [89], the leakage in FLASH is described in Refs. [117, 119].

As a result of the simplified treatment, some resulting quantities are inaccurate. This includes the neutrino energy, but also the evolution of the electron fraction, and thus entropy and temperature. We discuss resulting differences between an M1 transport scheme and a gray neutrino leakage in Sec. 5.7.

Deleptonization

Neutrino schemes that do not evolve the neutrino distribution function require an additional treatment of the deleptonization in the pre-collapse phase. FLASH and GR1D employ a deleptonization scheme from Ref. [92], which utilizes a parametrization of the electron fraction. We introduce the concept of Ref. [92] in the following.

The underlying idea is to parametrize the profile of the electron fraction as a function of density, and then evolve the electron fraction using that parametrized fit, which is computationally advantageous. This replaces the actual evolution of the electron fraction within the neutrino transport. The profile of the electron fraction as a function of density is calculated via:

$$Y_e(x) = \frac{1}{2}(Y_2 + Y_1) + \frac{x}{2}(Y_2 - Y_1) + Y_c[1 - |x| + 4|x|(|x| - 1/2)(|x| - 1)]\,, \tag{3.35}$$

where Y_c denotes a correction factor. Further, Y_1 and Y_2 correspond to the electron fraction at density ρ_1 and ρ_2, and x is given by:

$$x(\rho) = \max\left[-1, \min\left(1, \frac{2\log\rho - \log\rho_2 - \log\rho_1}{\log\rho_2 - \log\rho_1}\right)\right]. \tag{3.36}$$

The electron fraction Y_1 at density ρ_1, and electron fraction Y_2 at ρ_2, can either be modified by the user, or default values ($Y_1 = 0.5$ with $\rho_1 \sim 2 \cdot 10^7\,\mathrm{g\,cm^{-3}}$ and $Y_2 = 0.275$ with $\rho \sim 2 \cdot 10^{13}\,\mathrm{g\,cm^{-3}}$) can be applied.

The evolution of the electron fraction along the profile $\bar{Y}_e(\rho)$ is taken as:

$$\frac{\delta Y_e}{\delta t} = \frac{\min\left\{0, \bar{Y}_e[\rho(t+\delta t)] - Y_e(t)\right\}}{\delta t}, \tag{3.37}$$

where the minimum function ensures that the electron fraction decreases monotonically. We illustrate how the parametrized profile (denoted as "fit") compares to a profile that is obtained from a simulation with a full neutrino transport ("data") in Fig. 3.3. The fit captures the main features that emerge with the full transport.

At high densities, $\rho \sim 10^{14}\,\mathrm{g\,cm^{-3}}$, however, the electron fraction from the full transport simulation increases again, which the parametrization does not reproduce due to the minimum function applied in Eq. (3.37). This region represents the center of the proto-neutron star (PNS), where neutrons become degenerate and as a result, the electron fraction increases again. This implies that the central value of Y_e cannot be reproduced accurately. As a consequence, changes in the entropy in the center of the PNS are not captured as well, which affects the temperature in the PNS interior. We discuss the implications in Sec. 5.7. Nonetheless, the deleptonization scheme is able to reproduce the majority of the profile with significantly reduced computational effort.

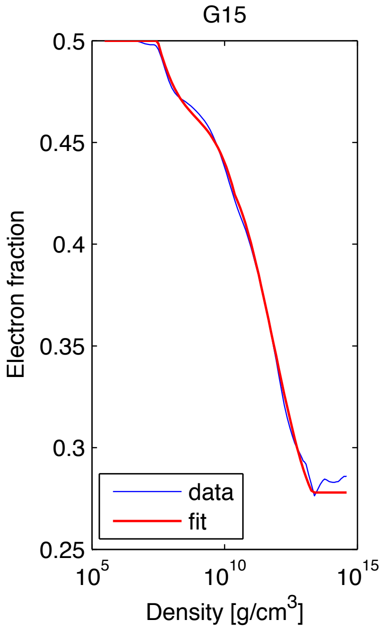

Figure 3.3.: Electron fraction profile fit at bounce, from Ref. [92].

3.5 Equation of state tables

The EOS closes the system of hydrodynamic equations. With more than a billion calls to the EOS per second (simulation time), it is quite significant that the evaluation of pressure and internal energy is as efficient as possible. However, nuclear EOS models that calculate the EOS for extreme conditions are computationally expensive. It is therefore quite common to utilize a tabulated EOS instead of an actual calculation, as interpolations are computationally faster.

The EOS tables contain thermodynamic quantities, including pressure P, internal energy E, entropy S, and chemical potentials μ for neutrons, protons, electrons, and neutrinos, as a function of density ρ, temperature T, and electron fraction Y_e. Pressure and internal energy are usually stored logarithmically. As the internal energy can become negative when the binding energy is the dominant contribution, one has to shift all internal energy values such that they are positive and the logarithm can be applied.

The composition of matter, including mass fractions X_i for the considered species i, depends on the conditions of the stellar plasma and is evaluated within the EOS as well. Different EOS assume different compositions besides neutrons and protons, e.g., the Lattimer & Swesty EOS [120] includes α particles and a single nucleus that is representative for all heavy nuclei, while EOS by Ref. [121] and others explicitly include light particles, e.g., deuterons. It is useful to introduce an average mass number $\bar{A}$ and average proton number $\bar{Z}$ that is calculated via $\bar{A} = \left(\sum_i X_i/A_i\right)^{-1}$ and $\bar{Z} = \bar{A}\sum_i Z_i Y_i$. To further reduce computational costs, EOS tables also tabulate the adiabatic index, the speed of sound, and certain derivatives that appear in the hydrodynamic equations.

Usually, these tables range around $\rho \sim 10^3 - 10^{16}\,\mathrm{g\,cm^{-3}}$, $T \sim 0.01 - 250\,\mathrm{MeV}$, and $Y_e \sim 0.01 - 0.6$. Density and temperature are logarithmically spaced with more than 250 values for the density, and around 150 values for temperature. The electron fraction is equally spaced with around 60 values. This means that each table variable stores more than two million values, with at least 15 table variables. The boundaries of the EOS also limit the computational domain, as values below and above table limits cannot be evaluated. A formalism how to simulate beyond the lower limits in EOS tables is introduced in Chapter 6.

EOS tables that are applicable in GR1D and FLASH are available from Ref. [89] and Ref. [122] at Ref. [123] for various EOS models. The tables from Ref. [89] include a transition from the nuclear EOS model to the Helmholtz

EOS, see Sec. 4.5. The transition density varies for different tables, as discussed in Ref. [89]. Further, Ref. [89, 124] offers an open-source code that creates an EOS table for a given nuclear EOS input. It adds the contributions from electrons, positrons, and photons to the nuclear EOS input if necessary, and further calculates the adiabatic index, speed of sound and relevant derivatives. Recently, additional EOS tables have been published by Ref. [122, 125], including an open-source code that computes individual EOS tables based on Skyrme density functional theory with arbitrary Skyrme parameters as input.

4 Equation of State

The equation of state (EOS) is a crucial component in core-collapse supernova (CCSN) simulations. The wide ranges of density and temperature in CCSN are quite challenging when developing a valid and consistent description for all conditions that occur. While the EOS for moderate densities and temperatures is well described within theories, the EOS for dense matter is still not fully understood. The strong interaction has to be considered when densities reach nuclear density, and the nuclear many-body problem poses an additional challenge. To this day, solely phenomenological EOS models exist for the application in CCSN simulations.

In this chapter, we introduce fundamentals of the EOS and discuss the different conditions and characteristics of matter in CCSN. Recent developments regarding an EOS for hot and dense matter are shortly summarized, including constraints for the nuclear EOS from observations, theory, and experiments. We discuss phenomenological models that have been widely used in simulations, and present individual contributions to the EOS from different constituents of matter. The first section follows Refs. [67, 126].

4.1 General considerations

The equation of state (EOS) describes the relation between thermodynamic variables. It is derived from the thermodynamic potential, which fully specifies the state of matter in thermodynamic equilibrium. An example for such a potential is the internal energy $U(S, V, N)$ with natural variables entropy S, volume V, and particle number N. Its total differential for a system with different particle species i reads:

$$\mathrm{d}U = T\mathrm{d}S - P\mathrm{d}V + \sum_i \mu_i \mathrm{d}N_i \,, \tag{4.1}$$

with temperature T, pressure P and chemical potential μ. In most cases, the temperature rather than the entropy of the system is known or can be measured. It is therefore useful to express the thermodynamic potential in terms of temperature, volume, and particle number. Using a Legendre transformation with respect to entropy, the internal energy is transformed into the free energy $F(T, V, N)$ with natural variables T, V, and N:

$$F = U - T \cdot S \,. \tag{4.2}$$

The free energy is the thermodynamic potential to the canonical ensemble, which is a system with fixed particle number, and constant volume in thermodynamic equilibrium with an external heat bath at fixed temperature.

The macroscopic thermodynamic quantities can be related to a microscopic description by expressing the properties of single particles in terms of probability distributions. In the case of the canonical ensemble, the probability distribution p_n is given by a Boltzmann distribution:

$$p_n = \frac{1}{Z} \exp\left(-\frac{E_n}{k_\mathrm{B} T}\right) , \tag{4.3}$$

with the partition function $Z(T, V, N)$, which contains the number of all possible states in the system and acts as normalization for the probability. Further, k_B refers to the Boltzmann constant and E_n depicts the particular energy states in the system. In the quantum statistical mechanics description, the partition function reads:

$$Z = \mathrm{Tr}\left(\exp\left(-\frac{\hat{H}}{k_\mathrm{B} T}\right)\right) , \tag{4.4}$$

where $\hat{H}(V,N)$ denotes the Hamiltonian of the system, and Tr refers to the trace. In the thermodynamic limit, the energy expectation value $\bar{E} = \langle \hat{H} \rangle$ of the system becomes the internal energy. The partition function is then determined by the ground state, meaning $Z = \exp(-E_0/k_\mathrm{B}T) = \exp(-F/k_\mathrm{B}T)$. The free energy follows as:

$$F(T,V,N) = -k_\mathrm{B}T\ln(Z)\,, \tag{4.5}$$

which links the microscopic description (partition function, quantum statistical mechanics) to the macroscopic description (thermodynamic potential).

In the context of core-collapse supernova simulations, it is common to express the free energy in terms of temperature, density, and particle density or particle fraction. The density is related to the volume via $\rho = m/V$, and the particle density follows from $n_i = N_i/V$. Pressure, entropy, and chemical potential are calculated from the free energy with:

$$P = \rho^2 \frac{dF}{d\rho}\bigg|_{T,n_i}\,, \qquad S = -\frac{dF}{dT}\bigg|_{\rho,n_i}\,, \qquad \text{and} \qquad \mu_i = \frac{dF}{dn_i}\bigg|_{\rho,T,n_{j\neq i}}\,. \tag{4.6}$$

Note that in the thermodynamic limit, ratios of extensive quantities behave as an intensive quantity. We further define the abundance $Y_i = n_i/n$, where n denotes the total particle density.

4.2 Application in core-collapse supernovae

In core-collapse supernova (CCSN) simulations, matter is treated as a fluid and modeled using a hydrodynamic description of the system. The broad range of conditions reached in CCSN simulations is challenging for a consistent construction of the EOS. The proto-neutron star (PNS) in the center exhibits densities up to $\rho \sim 10^{15}\,\mathrm{g\,cm^{-3}}$ and temperatures around $T \sim 10^{12}\,\mathrm{K}$, while outer layers of the progenitor star are moderately dense, with $\rho \sim 10^5\,\mathrm{g\,cm^{-3}}$ and $T \sim 10^8\,\mathrm{K}$, or less. Additionally, isospin asymmetries arise and the electron fraction spans from $Y_e \sim 0.05$, close to the neutrinosphere inside the PNS, to $Y_e \sim 0.55$ and more. A visual representation of CCSN conditions is shown in Fig. 4.1. The plot indicates every combination of density, temperature, and electron fraction (color coded) that is reached within the first second of a CCSN simulation, for details see Appendix A. Blue-green colored regions represent neutron-rich conditions.

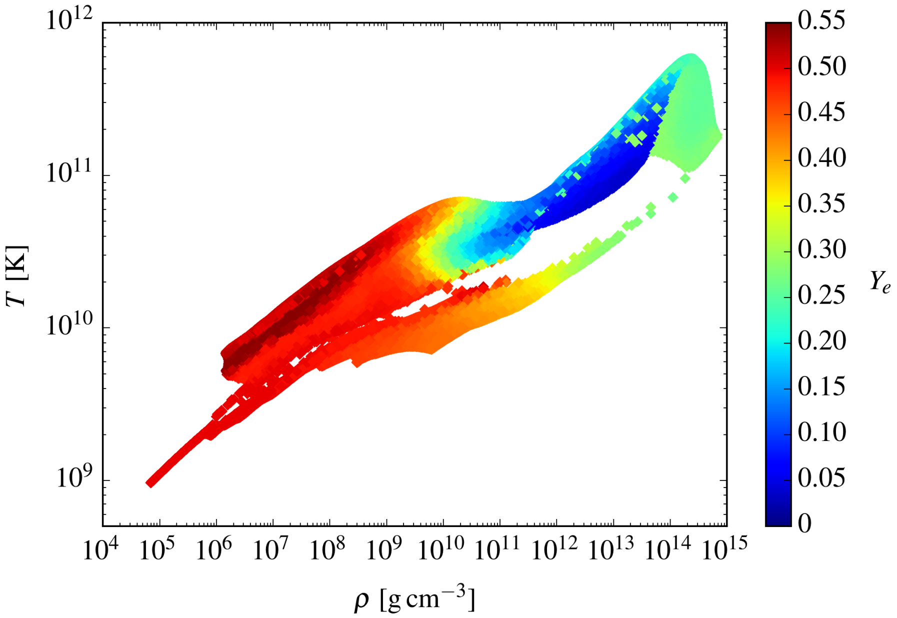

Figure 4.1.: Visual representation of CCSN conditions, for simulation details see Appendix A. Thanks to Carlos Mattes for providing the plot routine.

The characteristics of matter vary quite drastically in the different regions. While uniform matter (unbound neutrons, protons, and electrons) is present inside the PNS, outer layers are composed of non-uniform matter, which includes nuclei. In many cases, EOS models are solely suitable for a particular regime, choosing the relevant degrees of freedom for that specific purpose. Further, uncertainties arise for hot and dense matter. Ab initio calculations considering the strong interaction in the presence of high isospin asymmetries, as well as the nuclear many-body problem are topic of current research, for a recent review see, e.g., Refs. [127–129].

The construction of an EOS requires that matter is in thermodynamic equilibrium. In CCSN simulations, this can be formulated in terms of a local thermal equilibrium [130]. Further, chemical equilibrium can be assumed if the timescale of the hydrodynamic evolution is larger than possible reaction timescales of the constituents of matter. This is usually valid for regions with temperatures above $T \sim 0.5\,\mathrm{MeV}$ [131], where one defines a nuclear statistical equilibrium (NSE):

$$\mu_i = Z_i \mu_p + (A_i - Z_i)\mu_n \,, \tag{4.7}$$

with Z_i representing the proton number and A_i denoting the mass number. The indices n and p correspond to the chemical potentials of neutrons and protons, respectively.

While equilibrium for the strong and the electromagnetic interaction can be assumed, this may not always be valid for weak reactions [120]. Usually, neutrinos are not considered in the EOS. Nevertheless, some EOS variables, e.g., electron number densities, are subject to neutrino interactions. To connect neutrinos to the EOS, they are modeled within a so-called neutrino transport, see Sec. 3.4, which is coupled to the hydrodynamics, and therefore also to the EOS.

4.3 Dense matter

The interior of the PNS exceeds nuclear densities. Matter is uniform, meaning it consist of free neutrons, protons, and electrons. The mean free path of the particles becomes relatively small, and the strong interaction between the nucleons determines the behavior of the system. An exact treatment of the nuclear many-body problem at finite temperatures and isospin asymmetries is still topic of current research. Ab initio calculations are only available for certain regimes, e.g., pure neutron matter, a detailed discussion can be found, e.g., in Refs. [127–129]. However, no ab initio calculation is able to construct an EOS that is applicable for the whole range of conditions in CCSN.

Therefore, CCSN simulations rely on phenomenological approaches, like Skyrme-type interactions or meson-exchange forces in a relativistic mean-field approximation. These effective interactions contain nuclear parameters, which are obtained from joined efforts of experiments and theory. We discuss two EOS models that have been widely used in CCSN simulations in more detail in the next section (Lattimer & Swesty, Shen *et al.*).

Even though the EOS for high densities is still not fully understood, there are different types of constraints that have become available in recent years. To illustrate this, we consider an idealized system of cold nuclear matter with $T = 0$, and expand the energy per particle E/A in terms of an isospin asymmetry parameter $\beta = (n_n - n_p)/n$:

$$\frac{E}{A}(n,\beta) = \frac{E}{A}(n,0) + E_{\mathrm{sym}}(n)\beta^2 + \mathcal{O}(\beta^4)\,, \tag{4.8}$$

where E_{sym} denotes the symmetry energy. Further expanding the first two terms in a relative density replacement $x = (n - n_0)/3n_0$ with saturation density n_0 results in:

$$\frac{E}{A}(n,0) = -B + \frac{1}{2}Kx^2 + \dots\,, \qquad \text{and} \qquad E_{\mathrm{sym}}(n) = J + Lx + \frac{1}{2}K_{\mathrm{sym}}x^2 + \dots\,, \tag{4.9}$$

with binding energy B and incompressibility K. The symmetry energy contains the symmetry energy coefficient J, sometimes also referred to as S_ν, the slope parameter L, and the curvature parameter K_{sym}. The nuclear matter properties n_0, B, K, and E_{sym} can be obtained from experimental measurements or theoretical calculations.

Note that these nuclear parameters are highly correlated. Recent work by Ref. [27] analyzes and combines all available constraints from theory, experiments, and observations consistently, see also Refs. [26, 64, 65, 127, 132, 133]. They find that the symmetry energy parameters J and L exhibit a strong linear correlation, which is used to confine these two nuclear matter properties, see Fig. 4.2. Experimental data compiled from nuclear masses, neutron skin measurements, giant dipole resonances ("GDR"), dipole polarizability, and heavy ion collisions ("HIC") yield a region where all these limits overlap. Additionally, neutron matter calculations, from chiral effective field theory ("H") and quantum Monte Carlo ("G"), and observations of neutron stars, illustrated by the dashed purple rectangle ("Astrophysics"), constrain J and L further. A detailed review can be found, e.g., in Refs. [26, 132, 134]. Note that this analysis has certain limitations, as some experimental measurements are performed for certain isotopes and not for the whole range of nuclei, i.e., the dipole polarizability or neutron skin thickness. However, the work by Ref. [27] illustrates how combined data from theory, experiments, and observations can help to constrain the EOS. The results are summarized in Tab. 4.1, together with parameters employed in the widely used Lattimer & Swesty and Shen *et al.* EOS, and calculations from chiral effective field theory (χEFT), see Tab. 4.1.

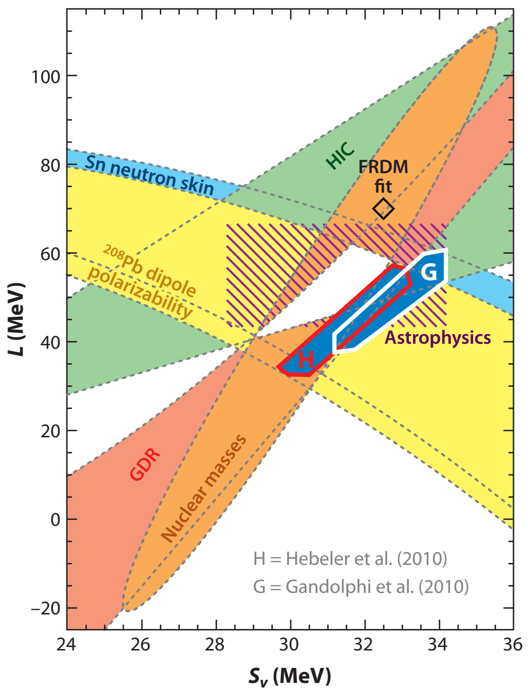

Figure 4.2.: Constraints for the symmetry energy parameters J and L, details see text, from Ref. [27, 132].

Neutron star (NS) observations provide additional, strong constraints for the EOS, as observed NS masses can be used as point of reference for EOS models. Computing the unique mass-radius (MR) relation for cold NS ($T \sim 0$), by solving the Tolman-Oppenheimer-Volkoff equations in β-equilibrium [63], yields a maximum mass for every EOS model, which can then be compared to observations. Especially masses of pulsars can be measured with great precision. In recent years, two massive NS with $M_{\mathrm{NS}} = (1.928 \pm 0.017)\,M_\odot$ [29, 135] and $M_{\mathrm{NS}} = (2.01 \pm 0.04)\,M_\odot$ [28] have been observed. An EOS model that is not able to support this maximum mass is not consistent with observations and can therefore be ruled out. This is illustrated in Fig. 4.3 and Fig. 4.4. Note that accurate measurements of NS radii that could constrain the EOS further have not been obtained so far.

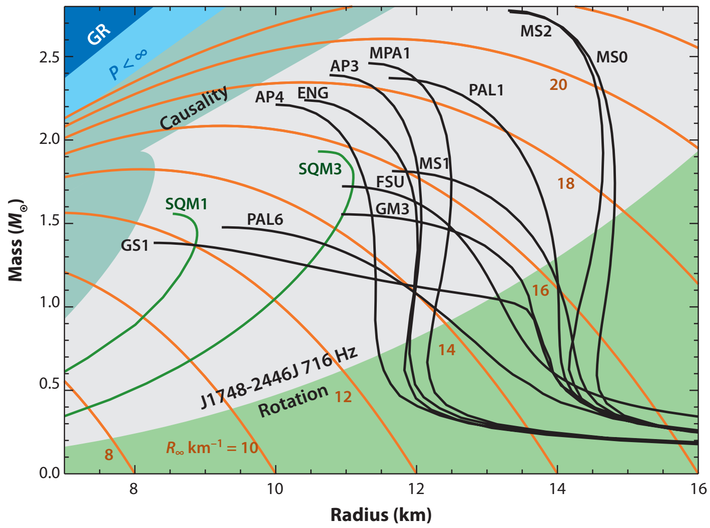

Figure 4.3.: Overview of several constraints for the MR relation of cold NS, details see text, from Ref. [64, 132].

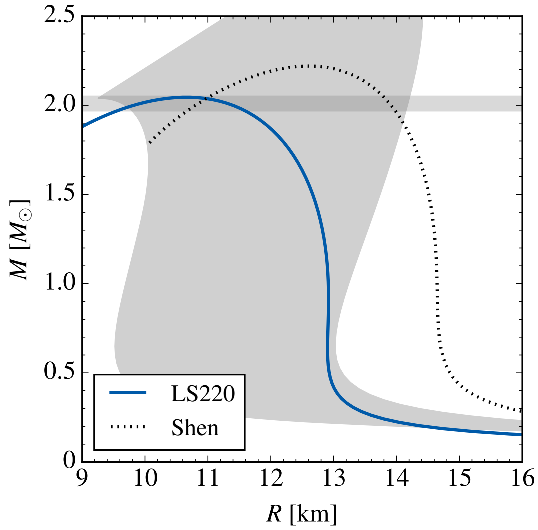

Figure 4.4.: MR relation for the LS220 and Shen EOS, chiral EFT with polytropes provides an uncertainty band [65, 127].

EOS	n_0 [fm^{-3}]	B [MeV]	K [MeV]	J [MeV]	L [MeV]	m^*	M_{NS} [$M_\odot$]	$R_{1.4\mathrm{M_{NS}}}$ [km]
LS220	0.155	16.00	220.0	28.61	73.7	1	2.06	12.2
Shen	0.145	16.26	281.2	36.89	110.8	0.634	2.22	14.6
χEFT	$0.157-0.171$	$15.29-16.43$	$175-254$	$28.4-35.7$	$32.4-69.8$	$\sim 0.8-1.0$		$9.7-13.9$
LL2013				$29.0-32.7$	$40.5-61.9$			$10.7-13.1$

Table 4.1.: Nuclear matter properties adopted in the Lattimer & Swesty EOS (LS220) [120] and Shen EOS [136]. Chiral effective field theory (χEFT) values from Refs. [65, 127, 129, 137–141]. Lattimer & Lim (LL2013) [27] combine constrains from theory, experiments, and observations. Experimental limits are not added in this table, an overview can be found, e.g., in Refs. [26, 64, 121, 132–134, 142]. Further, we add the effective mass value (m^*), the maximum mass (M_{NS}), and the radius for a NS with $M_{\mathrm{NS}} = 1.4\,M_\odot$ ($R_{1.4\mathrm{M_{NS}}}$).

There are additional constraints for the mass-radius relation shown in Fig. 4.3. Certain regions can be ruled out by relativistic limits ("GR"), finite pressure arguments ("$P < \infty$"), and causality, which means that the speed of sound must be smaller than speed of light [64, 132]. Also, the highest observed pulsar frequency ("Rotation") gives a lower limit [64, 132].

Further insights into the EOS can be gained from theoretical calculations. One example is chiral EFT, e.g., Refs. [127, 129, 137–139, 141, 143, 144]. Calculations for pure neutron matter can determine pressure or energy per particle, including theoretical uncertainties. These values can then be compared to pure neutron matter results from phenomenological models. Chiral EFT combined with a polytropic expansion provides an uncertainty band for the radii of NS, assuming different NS masses, illustrated in Fig. 4.4 with Refs. [65, 127].

Most of the EOS models that are available for CCSN do not fulfill all of the criteria that are mentioned above. However, tremendous progress has been made in recent years. More constraints from theory, experiments, and observations are forthcoming and new EOS models that attempt to fulfill these constraints are being developed. The multi-messenger era that has started with the first detection of a NS merger by the LIGO-VIRGO collaboration [145] will provide further insights into the properties of hot and dense matter, see also, e.g., Refs. [146, 147]. An example for this is shown in Fig. 4.5, which illustrates the combination of information from the observation of a single NS merger with the MR relation (see, e.g., Refs. [146–148]). More detections of such events will further contribute to the development of new limits.

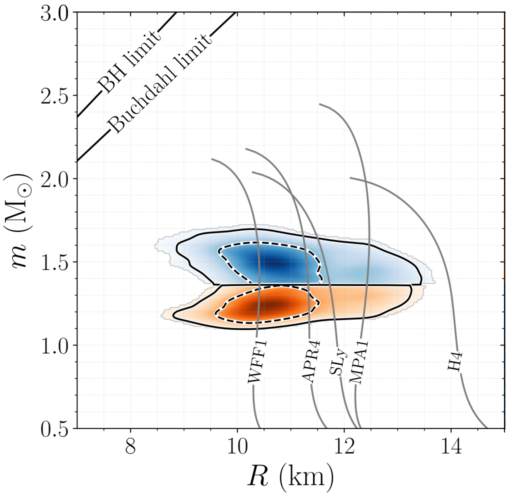

Figure 4.5.: Constraints for the MR relation from the NS merger detection by the LIGO-VIRGO collaboration, for more information see Ref. [30].

4.3.1 Lattimer & Swesty equation of state

The Lattimer & Swesty equation of state [120], further denoted as LS EOS, is one of the most commonly used EOS in CCSN simulations. It is based on a phenomenological, non-relativistic momentum-independent Skyrme interaction [149–151] in a self-consistent mean-field approximation, see also Ref. [152].

In the LS EOS, matter is assumed to consist of electrons, positrons, photons, unbound neutrons, unbound protons, alpha particles, and one single heavy nucleus that is representative for all heavy nuclei, a so-called single nucleus approximation (SNA). Alpha particles are representative for all light nuclei ($A \leq 4$) in the system. The free energy is written as [120]:

$$F = F_o + F_\alpha + F_N + F_{e^+} + F_{e^-} + F_\gamma\,, \tag{4.10}$$

where F_o denotes the free energy of unbound nucleons outside nuclei. Further, F_α and F_N represent light and heavy nuclei, respectively. Electrons F_{e^-} and positrons F_{e^+} are treated as ideal, non-interacting Fermi gas, and photons F_γ as ideal Bose gas. In the following, we focus on the nucleonic contribution, as leptons and photons can be considered separately, see Sec. 4.4.

Nuclei are described within the liquid-drop model. The free energy of heavy nuclei F_N is expressed in terms of nucleons F_{bulk} that are bound in nuclei, a surface energy F_s, and a Coulomb contribution F_C [120]:

$$F_N = F_{\mathrm{bulk}} + F_s + F_C \,. \tag{4.11}$$

Details of the surface and Coulomb contributions can be found in Ref. [120]. One main aspect in the LS EOS is that nucleons bound inside nuclei and nucleons outside nuclei are treated with the same expression for their free energy F_{bulk}. The phase transition from uniform to non-uniform matter is obtained using a Maxwell construction, for details see Ref. [120].

The internal energy density is obtained from Skyrme energy density functional theory [120, 151, 153]:

$$E_{\mathrm{bulk}}(n,x,T) = \sum_t \frac{\hbar\tau_t}{2m_t^*} + (a + 4bx(1-x))\,n^2 + cn^{1+\delta} - xn\Delta \,, \tag{4.12}$$

where $t = n, p$ denotes the isospin, x represents the proton fraction, and $a, b, c,$ and δ are the so-called simplified Skyrme parameters [120], which include nuclear matter properties, i.e., saturation density n_s, incompressibility K, binding energy B, and symmetry energy E_{sym}. A detailed derivation of these parameters including the effective mass can be found in Refs. [154, 155]. The first term in Eq. (4.12) corresponds to the nucleon kinetic energies, the second term ($\sim n^2$) represents the Skyrme two-body interaction, and the third term denotes the Skyrme many-body interaction. The last term accounts for the neutron-proton mass difference Δ, which appears as all energies in the LS EOS are written relative to the neutron rest mass. In the kinetic energy term, the density-dependent effective mass m^* is given by [120]:

$$\frac{\hbar^2}{2m_t^*} = \frac{\hbar^2}{2m} + \alpha_1 n_t + \alpha_2 n_{-t} \,, \tag{4.13}$$

where n_t is the number density of the corresponding nucleon and $-t$ denotes the opposite isospin. Note that the LS EOS does not include an effective mass, meaning $\alpha_1 = \alpha_2 = 0$. We discuss the impact of this in Chapter 5. In Eq. (4.12), no explicit dependence on the temperature is visible, however, it is included in the kinetic energy density τ_t terms and the nucleon number densities. The LS EOS provides a set of parameters with three different incompressibilities, $K = 180$, 220, and 375 MeV, where the ones with an incompressibility of $K = 180$ and 220 MeV have been widely used in CCSN simulations. We further consider the model with $K = 220$ MeV, denoted as LS220.

4.3.2 Shen equation of state

The Shen *et al.* equation of state [136, 156, 157], further denoted as Shen EOS, is based on a relativistic mean-field (RMF) model. Meson-exchange forces are used to calculate the nucleon interaction, following the idea by Yukawa [158] that massive particles mediate the nuclear force. It is a phenomenological model that has been used quite frequently in CCSN simulations.

The Shen EOS assumes the same constituents of matter as the LS EOS, meaning electrons, positrons, photons, unbound neutrons, unbound protons, alpha particles, and a single heavy nucleus, representing all heavy nuclei. Leptons and photons are considered separately. Heavy nuclei are treated within a Thomas-Fermi approximation, which is a parametrization of the density distribution of particles, for more details see Ref. [156]. The phase transition is obtained by calculating and comparing the free energy of uniform matter and non-uniform matter, assuming the lower free energy to be the present state.

The field equations of the interacting particles are derived from the Lagrangian density in the RMF theory. Nucleons are represented by Dirac spinors, which yield a set of coupled equations that are solved self-consistently in the

RMF approximation. The coupling to scalar mesons modifies the effective mass of nucleons, leading to different effective masses for the Shen and LS EOS, see Tab. 4.1. The meson masses and related coupling constants in the Lagrangian density are taken from experimental parameter sets, which in case of the Shen EOS is the TM1 RMF parametrization [159]. These parametrizations also determine the values for the nuclear matter properties.

Considering EOS models in CCSN simulations, the Shen EOS is less favorable for successful explosions compared to the LS220 EOS (see, e.g., Refs. [160, 161]). This can be related to the contraction behavior of the proto-neutron star, which highly depends on the EOS. However, it is not clear which component of the EOS is responsible for this behavior. We discuss this in Chapter 5.

4.3.3 Further developments

There have been recent efforts to improve EOS models for CCSN simulations (see, e.g., Refs. [121, 162–165]), either based on RMF theory or Skyrme-type interactions. For RMF models, different parametrizations within the same theoretical framework have been investigated, for example TMA [166] or FSUgold [167]. The SFHo parametrization [163, 168] is even constructed such that it is consistent with constraints from NS observations. Further, new Skyrme parameter sets have been developed, e.g., SLy4 [165], an overview can be found, e.g., in Refs. [122, 169]. Additionally, nuclei below the phase transition are described differently. While the LS EOS and Shen EOS treat nuclei within a single nucleus approximation, more recent models employ a chemical composition, assuming a statistical ensemble of different species and nucleons in thermal equilibrium. This captures shell effects of nuclei and also modifies neutrino opacities, see, e.g., Ref. [162].

4.4 Electrons, positrons, and photons

The free energy of the EOS is composed of the individual constituents of stellar matter. This includes leptons and photons in addition to nucleons. In this section, we present the contributions of electrons, positrons, and photons, investigate the conditions where these constituents become important, and also discuss the order of magnitude in which they occur.

Electrons and positrons are present in uniform as well as non-uniform matter. For the conditions encountered in CCSN, they can be treated as an ideal Fermi gas (see, e.g., Refs. [77, 120]), described by a Fermi-Dirac distribution:

$$f_{\mathrm{FD}} = \frac{1}{1+\exp((\epsilon-\mu)/k_{\mathrm{B}}T)}\,, \tag{4.14}$$

with energy ϵ and matter temperature T. Note that an additional term due to the rest mass energy may arise, depending on the definition. Electrons are degenerate for densities $\rho \gtrsim 10^5\,\mathrm{g\,cm^{-3}}$, and also relativistic, depending on the temperature, see Fig. 4.6. Charge neutrality requires:

$$n_p = n_{e^-} - n_{e^+}\,, \tag{4.15}$$

where n_p, n_{e^-}, and n_{e^+} are the number densities for protons, electrons, and positrons, respectively.

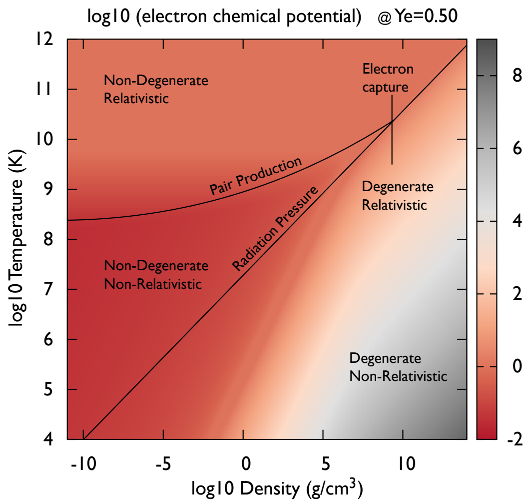

Figure 4.6.: Electron chemical potential, from Ref. [170], calculated with Ref. [171].

The number densities of electrons and positrons are obtained from the integral over the Fermi-Dirac distribution, i.e., $n = 2/(2\pi)^3 \int \mathrm{d}^3\mathrm{k}\, f_{\mathrm{FD}}$. In the ultra-relativistic case, the integration is evaluated with the following Fermi-Dirac integral:

$$F_k(\eta,\beta) = \int_0^\infty \frac{x^k(1+\frac{1}{2}\beta x)^{1/2}}{1+\exp(x-\eta)}dx\,, \qquad \text{with} \qquad \beta = \frac{k_{\mathrm{B}}T}{m_e c^2}\,, \qquad \text{and} \qquad \eta = \frac{\mu}{k_{\mathrm{B}}T}\,. \tag{4.16}$$

The electron number density and positron number density then follow as, e.g., Refs. [77, 122, 171]:

$$n_{e^-} = K\beta^{3/2}\left[F_{1/2}(\eta,\beta) + F_{3/2}(\eta,\beta)\right], \qquad \text{and} \qquad n_{e^+} = K\beta^{3/2}\left[F_{1/2}(-\eta-\frac{2}{\beta},\beta) + F_{3/2}(-\eta-\frac{2}{\beta},\beta)\right], \tag{4.17}$$

with $K = 8\pi\sqrt{2}m_e^3c^3/h^3$ and the electron mass m_e. The degeneracy parameter η and number densities are determined by charge neutrality. Therefore Eq. (4.15) and Eq. (4.17) are solved iteratively. Note that the number densities are defined such that the chemical potential of electrons does not include the rest mass energy. Consequently, it has to be added to the chemical potential of positrons with $\eta_{e^+} = -\eta - 2/\beta$, and thus the number density of positrons in Eq. (4.17) has a different form.

The Fermi-Dirac integrals that appear in the number densities cannot be solved analytically. In CCSN simulations, it is therefore common to use a tabulated free energy for electrons and positrons, and compute internal energy, pressure and entropy from Eq. (4.6). This electron-positron table is sometimes referred to as "Timmes EOS". Details for the implementation and its accuracy can be found in Refs. [171, 172].

For electrons, pressure, internal energy, and entropy read, e.g., Ref. [122]:

$$P_{e^-} = \frac{2}{3}Km_ec^2\beta^{5/2}\left[F_{3/2}(\eta,\beta) + \frac{\beta}{2}F_{5/2}(\eta,\beta)\right], \tag{4.18}$$

$$E_{e^-} = Km_ec^2\beta^{5/2}\left[F_{3/2}(\eta,\beta) + \beta F_{5/2}(\eta,\beta)\right], \tag{4.19}$$

$$S_{e^-} = \frac{P_{e^-} + E_{e^-}}{T} - n_{e^-}\eta, \tag{4.20}$$

and analogously for positrons, including the rest mass energy difference.

In the following, we compare the order of magnitude of the contributions from the different constituents, starting with pressure as a function of density and temperature. Internal energy and entropy are presented in Sec. 4.5. The electron pressure in Eq. (4.18) follows $\beta^{5/2} \sim T^{5/2}$. There is no explicit density dependence, however, the chemical potential, and thus Fermi-Dirac integrals and number densities, depends on the matter density, see Fig. 4.6. A visual representation of Fermi-Dirac integrals as a function of η and β is illustrated in Ref. [173].

A typical profile of the temperature as a function of density in a CCSN simulation is shown in Fig. 4.7. The shock position is visible at around $\rho \sim 10^9\,\mathrm{g\,cm^{-3}}$. The temperature is maximal inside the PNS ($\rho \sim 10^{11}\,\mathrm{g\,cm^{-3}}$), and decreases following $\rho^3 \sim r^{-1}$. The pressure of electrons ("e^-") rises with increasing density and temperature. Positrons ("e^+") follow a similar trend, although Pauli-blocking reduces the amount of positrons in the PNS. The nucleonic pressure ("*nuc*", unbound and bound, here for the LS220 EOS) yields the main contribution for densities above $10^{10}\,\mathrm{g\,cm^{-3}}$, see the previous sections. However, electrons substantially support the total pressure, and are the major contribution for $\rho < 10^9\,\mathrm{g\,cm^{-3}}$. The plot additionally shows the radiation pressure from photons ("γ").

Photons are included assuming a simple blackbody emission in thermodynamic equilibrium. Pressure, internal energy, and entropy read:

$$P_\gamma = \frac{4\sigma_\mathrm{B}}{3c}\cdot T^4, \qquad E_\gamma = 3\cdot P_\gamma/\rho, \qquad \text{and} \qquad S_\gamma = \frac{P_\gamma/\rho + E_\gamma}{T}, \tag{4.21}$$

where σ_B denotes the Stefan-Boltzmann constant with $\sigma_\mathrm{B} = 2\pi^5k_\mathrm{B}^4/(15h^3c^2)$.

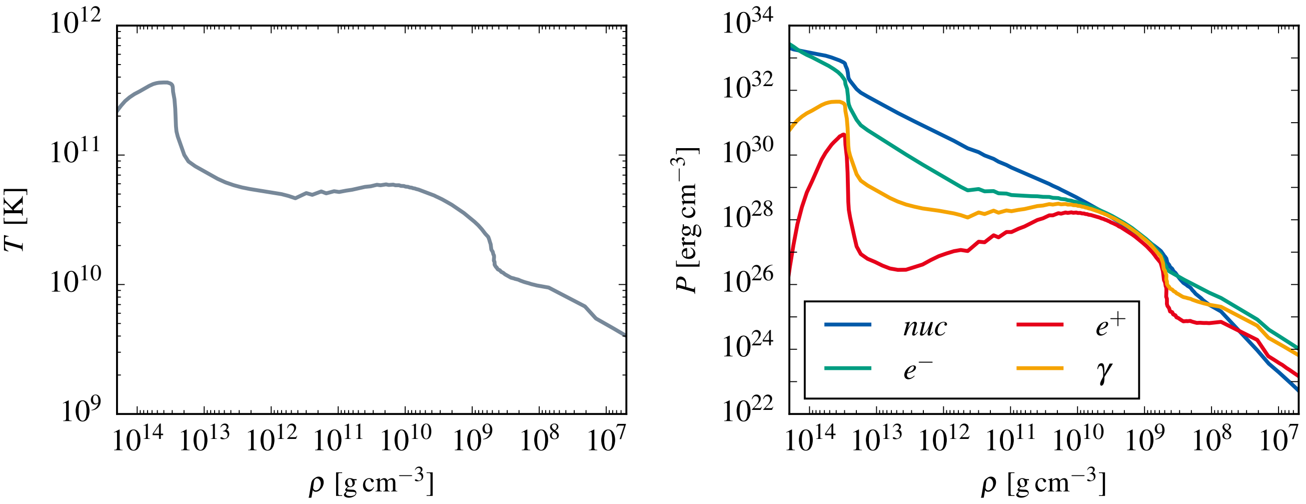

Figure 4.7.: Temperature and individual pressure contributions as a function of density for representative conditions in a CCSN simulation (with the LS220 EOS). Simulation details can be found in Appendix A.

The pressure solely depends on temperature ($\sim T^4$), which is reflected in the contribution shown in Fig. 4.7. For nuclear densities, the radiation pressure is minor compared to nucleons and electrons, which are highly dependent on density. However, below $\rho \sim 10^{10}\,\mathrm{g\,cm^{-3}}$, photons substantially support the pressure and yield, together with electrons, the main contribution at moderate densities.

Note that we do not include light particles and Coulomb corrections in our discussion. Their contribution is relatively small compared to the main components. However, light particles are relevant for the determination of the chemical equilibrium and affect the identification of the minimum of the free energy (see, e.g., Ref. [120]). A discussion of the Coulomb corrections can be found in Refs. [77, 174, 175].

4.5 Helmholtz equation of state

Outside the PNS, densities and temperatures decrease with increasing radius. For these moderate conditions, the average distance between the constituents is large enough such that the strong interaction can be neglected. Further, nucleons are bound in ions. Matter can thus be described as a plasma of ions, electrons, positrons, and photons. The free energy of the system is written as [77]:

$$F = F_{\mathrm{ion}} + F_{e^-} + F_{e^+} + F_\gamma \,. \tag{4.22}$$

An EOS that includes these constituents is also referred to as "Helmholtz" EOS. The terminology Helmholtz EOS refers to the Timmes EOS where photons and ions are added to electrons and positrons. It provides a reasonable description as long as the strong interaction can be neglected, thus for $\rho \lesssim 10^{10}\,\mathrm{g\,cm^{-3}}$ [171]. The term for nucleons outside nuclei in Eq. (4.10) vanishes, and the contribution from nuclei is reduced to the ion component. The correction terms that arise for Coulomb interactions of the ionized nuclei is discussed in Ref. [77].

The ion contribution is approximated from an ideal gas equation with an adiabatic index of 5/3 [77]. Pressure and internal energy read [77]:

$$P_{\mathrm{ion}} = \frac{N_{\mathrm{A}}}{\bar{A}}\,\rho\, k_{\mathrm{B}} T\,, \qquad \text{and} \qquad E_{\mathrm{ion}} = \frac{3}{2}\cdot\frac{N_{\mathrm{A}}}{\bar{A}}\, k_{\mathrm{B}} T\,, \tag{4.23}$$

with the Avogadro constant N_{A}. The entropy is calculated via:

$$S_{\mathrm{ion}} = \frac{N_{\mathrm{A}}\, k_{\mathrm{B}}}{\bar{A}} \left(\frac{5}{2} + \log\left[\frac{\bar{A}^{5/2}}{N_{\mathrm{A}}\,\rho} \left(\frac{2\pi k_{\mathrm{B}} T}{m_p h^2} \right)^{3/2} \right] \right), \tag{4.24}$$

the so-called "Sackur-Tetrode" equation. We further introduce the average mass number $\bar{A}$ and average proton number $\bar{Z}$:

$$\bar{A} = \left(\sum_i X_i / A_i \right)^{-1} , \qquad \text{and} \qquad \bar{Z} = \bar{A} \sum_i \frac{Z_i \, X_i}{A_i} = \bar{A} \sum_i Z_i Y_i \, , \tag{4.25}$$

with the mass fraction X_i of an isotope i and the abundance Y_i:

$$X_i = \frac{\rho_i}{\rho} = \frac{n_i \, A_i}{\rho \, N_\mathrm{A}} , \qquad \text{and} \qquad Y_i = \frac{X_i}{A_i} = \frac{n_i}{\rho \, N_\mathrm{A}} . \tag{4.26}$$

The pressure contribution from ions is proportional to the product of density and temperature, which implies an increase of pressure towards the center of the star. The internal energy follows the temperature. Note that the binding energy of nuclei is not considered in Eq. (4.23), the internal energy is therefore likely overestimated. The entropy depends on the logarithm of the ratio of temperature and density. Additionally, pressure, energy, and entropy are proportional to the inverse of the average mass number, which is determined by the composition. In CCSN, the average mass number is mainly determined by the shock position, as the shock wave dissociates nuclei into protons, neutrons, and alpha particles, resulting in a small average mass number, see Chapter 2. In front of the shock wave, nuclei are present. The contributions to pressure, internal energy, and entropy for all discussed constituents are depicted in Fig. 4.8, for the same profile as in Fig. 4.7. The shock position is visible at around $\rho \sim 10^9\,\mathrm{g\,cm^{-3}}$.

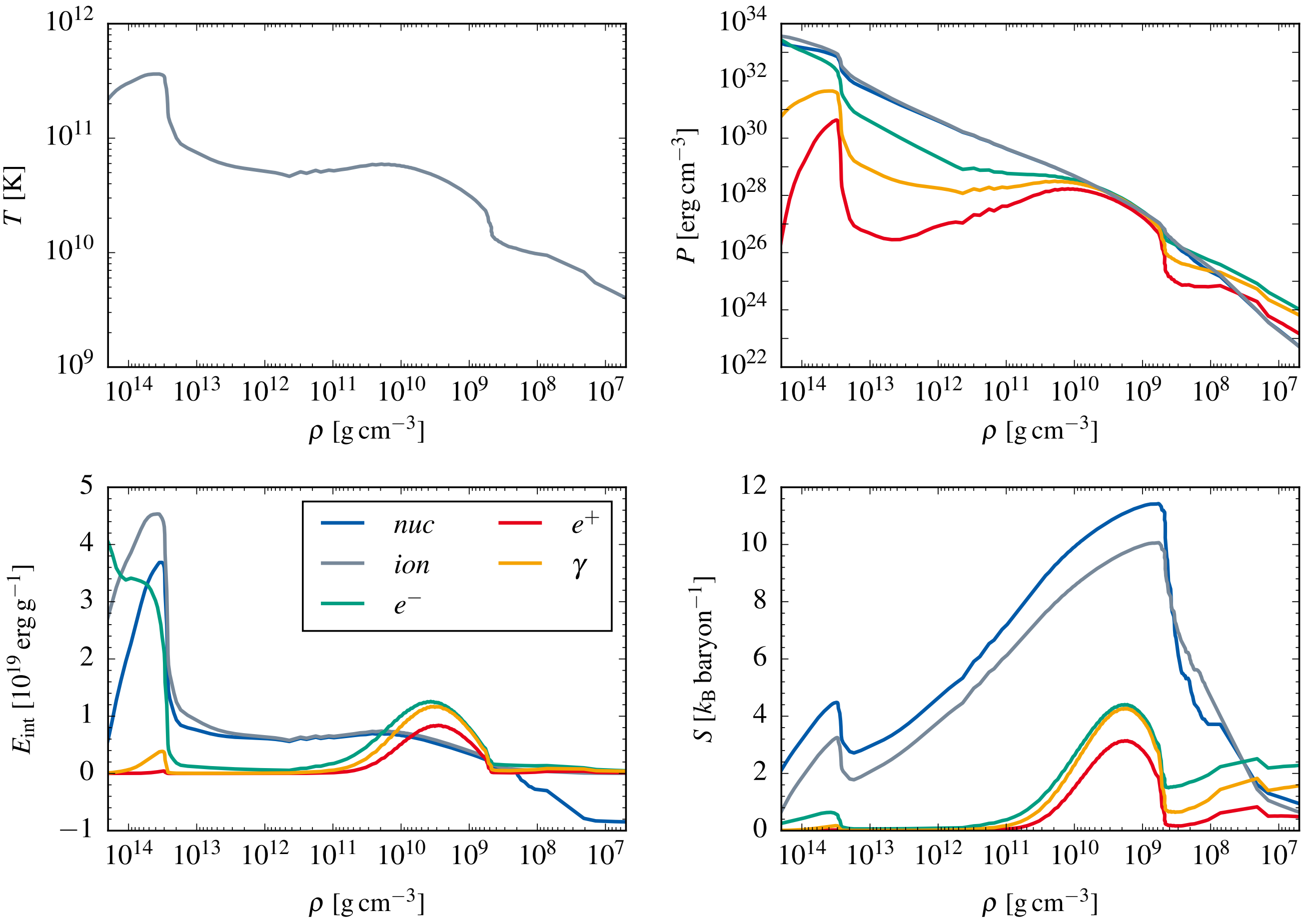

Figure 4.8.: Temperature and individual contributions to pressure, internal energy, and entropy as a function of density for representative conditions in a CCSN simulation (with the LS220 EOS). Simulation details can be found in Appendix A.

The ion contribution approximately agrees with nuclear matter calculations from the high-density EOS, except for densities where the strong interaction becomes highly relevant. Internal energy and entropy follow a similar pattern as previously discussed for the pressure. Inside the PNS, pressure, energy, and entropy are dominated by the nucleonic contribution, followed by electrons and photons. Note that we do not show contributions from light nuclei and Coulomb corrections here, since they are relatively small.

However, there is an additional difference in the internal energy. The nucleonic contribution is negative for densities below $\rho \lesssim 10^9\,\mathrm{g\,cm^{-3}}$, in contrast to the ion contribution. This is a result of the missing binding energy that is not included in the Helmholtz EOS, which has to be considered when transitioning from one EOS to another. A possible method how to combine a high-density EOS and the Helmholtz EOS is investigated in Chapter 6.

5 Equation of State Effects in Core-Collapse Supernovae

The equation of state (EOS) is a key ingredient in core-collapse supernova (CCSN) simulations. It determines the contraction behavior of the proto-neutron star (PNS), and thus impacts neutrino energies, deciding the outcome of the simulation. The center of the PNS exhibits nuclear densities, where the strong interaction governs the behavior of uniform matter. However, the description of nuclear matter under these conditions is still topic of intense research and ab initio EOS calculations for the wide ranges of densities and temperatures in CCSN are not feasible yet. Therefore, CCSN simulations rely on phenomenological EOS models that differ in their nuclear physics input as well as underlying theory.

The differences in the nuclear physics input make it difficult to trace the impact of individual variables in the EOS. In this chapter, we present the first systematic study of varying different nuclear matter properties separately. We investigate the impact of the nucleon effective mass, incompressibility, symmetry energy, and nuclear saturation point in the framework of Skyrme density functional theory, using the Lattimer & Swesty EOS. We trace the contraction behavior of the PNS to the effective mass, which determines the thermal contributions to the EOS at nuclear densities.

The results in this chapter have been obtained in collaboration with Sabrina Schäfer, Almudena Arcones and Achim Schwenk. A manuscript is submitted [176]. We perform spherically symmetric simulations with the FLASH code [77, 161], a $15\,M_\odot$ progenitor [36], and the M1 neutrino transport scheme from Refs. [74, 82]. We enhance the energy deposition by neutrinos in the gain layer by a factor of 2.85 to trigger artificial explosions, see also Sec. 3.4.1. Further simulation details can be found in Appendix A.

5.1 Role of the equation of state in core-collapse supernova simulations

The uncertainties in the high-density equation of state (EOS) have significant impact in core-collapse supernovae (CCSN) simulations. Phenomenological EOS that are available differ in their underlying theory as well as their nuclear physics input. There are two EOS that have been used frequently in CCSN simulations. The Lattimer & Swesty or LS EOS [120] and the Shen *et al.* EOS [156]. While the LS EOS is based on a non-relativistic Skyrme density functional approach, the Shen EOS applies a relativistic mean-field theory (RMF) framework. They employ different values for the nucleon effective mass m^*, incompressibility K, symmetry energy E_{sym}, and nuclear saturation density n_0, as well as binding energy B. An overview of the parameters, as well as theoretical estimates from chiral effective field theory, can be found in Tab. 5.1. Note that these nuclear matter properties are defined at saturation density for cold matter ($T = 0$). In the following, we consider the LS EOS with an incompressibility of 220 MeV, further denoted as LS220.

	m^*/m	K [MeV]	${E_{\mathrm{sym}}}^1$ [MeV]	L [MeV]	n_0 [fm^{-3}]	B [MeV]
LS220	1.0	220	29.3	73.7	0.155	16.0
Shen	0.634	281	36.9	110.8	0.145	16.3
χEFT	$\sim 0.8-1.0$	$175-254$	$28.4-35.7$	$32.4-69.8$	$0.157-0.171$	$15.29-16.43$

Table 5.1.: Theoretical estimates from chiral effective field theory (χEFT) calculations for the effective mass m^* [137, 139, 140], incompressibility K [129, 138], symmetry energy E_{sym} [129], slope parameter L [127, 141], saturation density n_0 [141], and binding energy B [141], compared to values used in the LS220 and Shen EOS.

---

[1] Note that the symmetry energy in the Shen EOS is obtained via the second derivative of the energy per particle and not from the difference of neutron and symmetric matter as in the LS EOS.

The implications of these differences in the EOS are illustrated in Fig. 5.1. We present the evolution of the proto-neutron star (PNS) contraction and shock radius for simulations performed with the LS220 and Shen EOS. The PNS radius is defined as the radius where the density is equal to $10^{11}\,\mathrm{g\,cm^{-3}}$. The time $t = 0\,\mathrm{s}$ refers to the time of bounce. While the simulation performed with the LS220 EOS results in a successful explosion, the one with the Shen EOS does not explode. This can be traced to the different contraction behavior of the PNS. The success of the shock revival via the neutrino mechanism depends on the energy deposition by neutrinos, see also Chapter 2. The neutrino energies approximately scale with the temperature on the surface of the PNS. When the PNS contracts, its temperature increases and neutrino spectra harden. A faster contraction commonly results in higher neutrino energies, which supports a successful explosion.

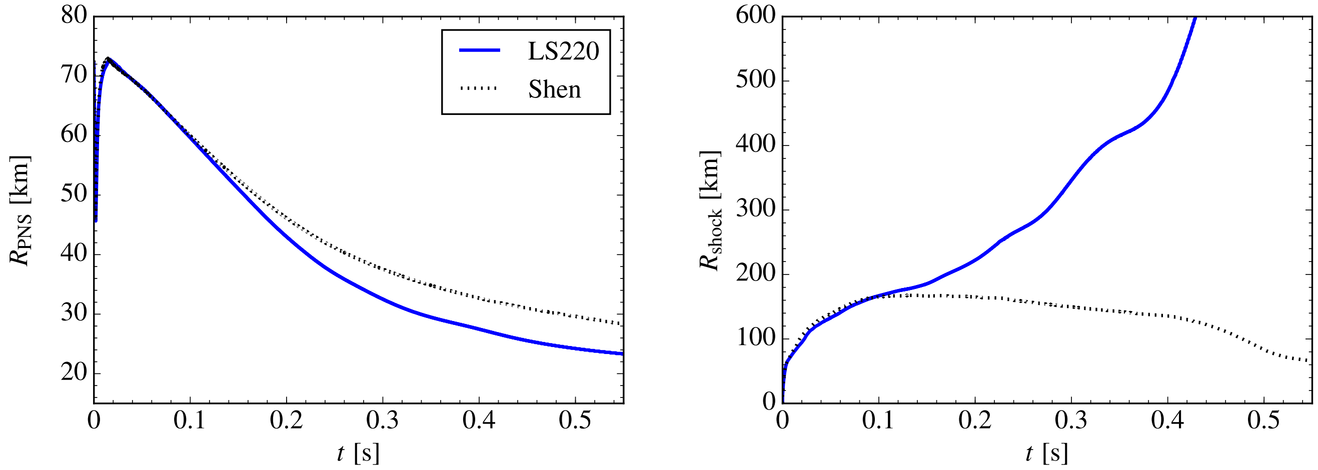

Figure 5.1.: Evolution of the PNS radius (left) and shock radius (right) for CCSN simulations performed with the LS220 EOS and Shen EOS.

The impact of the EOS in CCSN simulations has been discussed in various simulation setups by different groups (see, e.g., Refs. [31, 160, 161, 177]). Further, there has been recent effort to improve phenomenological EOS (see, e.g., Refs. [121, 162–165]). However, all available EOS studies always vary the complete set of the underlying nuclear physics input, e.g., Refs. [122, 163, 165–169], which makes it difficult to trace the individual impact of nuclear matter properties in the EOS. The only systematic study that has been performed so far is within the LS EOS, where three different values for the incompressibility ($K = 180, 200, 375\,\mathrm{MeV}$) are investigated [120], but it is not clear which component of the EOS determines the contraction behavior of the PNS.

5.2 Effective mass and Skyrme parameters

We modify nuclear matter properties within the framework of the Lattimer & Swesty EOS, which is based on a Skyrme energy density functional. The internal energy of bulk nuclear matter as a function of number density $n = n_n + n_p$, proton fraction $x = n_p/n$, and temperature reads [120]:

$$E_{\mathrm{bulk}}(n,x,T) = \sum_t \frac{\hbar^2 \tau_t}{2m_t^*} + (a + 4bx(1-x))\,n^2 + cn^{1+\delta} - xn\Delta\,. \tag{5.1}$$

The first term corresponds to the nucleon kinetic energy with isospin t and the nucleon energy density τ_t. The second and third term represent the two-body and many-body interaction, with the so-called simplified Skyrme parameters a, b, c, and δ. The neutron-proton mass difference Δ appears, since all energies in the LS EOS are written with respect to the neutron mass. Note that the temperature dependence is included in the nucleon energy density and nucleon density n_t.

The density-dependent effective mass for a nucleon with isospin t is calculated as [120]:

$$\frac{\hbar^2}{2m_t^*} = \frac{\hbar^2}{2m} + \alpha_1 n_t + \alpha_2 n_{-t}\,, \tag{5.2}$$

where $-t$ denotes the opposite isospin. The parameters α_1 and α_2 are used to fit the effective mass to the desired value for pure neutron matter (PNM) and symmetric matter (SM) at saturation density, respectively. In the following, we use $\alpha_1 = \alpha_2$, which results in [154, 155]:

$$\left.\frac{m^*}{m}\right|_{\mathrm{PNM,n_0}} = \left.\frac{m^*}{m}\right|_{\mathrm{SM,n_0}} = \frac{\hbar^2}{1+(\alpha_1+\alpha_2)mn_0/\hbar^2}\,. \tag{5.3}$$

The original work by Lattimer & Swesty does not include an effective mass, i.e., $\alpha_1 = \alpha_2 = 0$. As a result, the set of simplified Skyrme parameters that is provided in their work does not include an effective mass dependence. Together with Sabrina Schäfer, we derive these effective mass dependent parameters, see Refs. [154, 155] for more detail:

$$a = \frac{\alpha\left(\frac{5}{3}-\frac{m^*}{m}-\delta\right)-B\delta}{n_0(\delta-1)} - b\,, \tag{5.4}$$

$$b = \frac{1}{n_0}\left[(2^{2/3}-1)\,\alpha - E_{\mathrm{sym}}\right], \tag{5.5}$$

$$c = \frac{K-10\alpha\beta+18\alpha\left(\frac{5}{3}-\frac{m^*}{m}\right)}{9\delta(\delta-1)n_0^{\delta}}\,, \tag{5.6}$$

$$\delta = \frac{K-10\alpha\beta+18\alpha\left(\frac{5}{3}-\frac{m^*}{m}\right)}{9B+\alpha\left(9\,\frac{m^*}{m}-6\right)}\,, \tag{5.7}$$

where the nuclear matter properties incompressibility K, symmetry energy E_{sym}, binding energy B, and saturation density n_0 are included in the set of Skyrme parameters. Further, in our case $\alpha = \alpha_{\mathrm{SM}} = \alpha_{\mathrm{PNM}} = 3\hbar^2(3/2\pi^2 n_0)^{2/3}/(10m^*)$. Note that these are the parameters for the case $\alpha_1 = \alpha_2$, which agree with the Skyrme parameter set provided in the LS EOS when $m^*/m = 1$ and $\beta = 1$. The Skyrme parameters for $\alpha_1 \neq \alpha_2$ and $\alpha_{\mathrm{SM}} \neq \alpha_{\mathrm{PNM}}$ can be found in Refs. [154, 155].

An illustration how variations of the nuclear matter properties modify the internal energy, Eq. (5.1), is shown in Fig. 5.2 for cold nuclear matter, i.e., $T = 0$. The energy per particle of symmetric matter ($n_p = n_n$) is minimal at saturation density n_0, which also defines the binding energy B. The incompressibility K determines the curvature of symmetric matter and impacts the curvature of pure neutron matter ($n_p = 0$, $n_n = n$). For pure neutron matter, the energy per particle is positive as the system is unbound. The energy difference of neutron matter to symmetric matter at saturation density is determined by the symmetry energy E_{sym}.

In the following, we vary each of the nuclear matter properties individually from values of the LS220 EOS to values of the Shen EOS. With this, we are able to investigate which of the parameters, effective mass m^*, incompressibility K, symmetry energy E_{sym}, or saturation density n_0 together with the binding energy B, determines the contraction behavior of the PNS. We create seven different EOS tables, where we calculate a new set of Skyrme parameters for every individual variation. An overview of the parameters can be found in Tab. 5.2.

We investigate three different values for the effective mass. The first one corresponds to the original LS220 EOS, where no effective mass is included, thus $m^*/m = 1$. For the second variation, we chose a value of $m^*/m = 0.8$, which is an estimate from chiral effective field theory calculations [137, 139, 140], and label it as $m^*_{0.8}$. For the third scenario, we employ the effective mass value from the Shen EOS and label it accordingly, m^*_{S}.

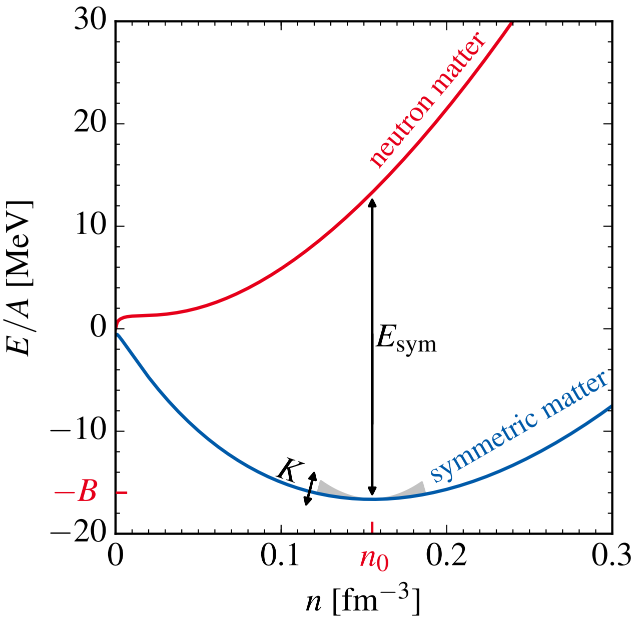

Figure 5.2.: Energy per particle as a function of number density with variations of nuclear matter properties for cold nuclear matter, i.e., $T = 0$. Thanks to Sabrina Schäfer for providing the plotting routine.

On top of the effective mass variations, we change the incompressibility from the value of the LS EOS to the value of the Shen EOS, denoted as $(m^*, K)_\mathrm{S}$. Further, we vary the symmetry energy in combination with the effective mass, $(m^*, E_\mathrm{sym})_\mathrm{S}$, and investigate the case where K and E_sym are modified simultaneously, $(m^*, K, E_\mathrm{sym})_\mathrm{S}$. Finally, we change the saturation point together with the previous variations, and also re-fit the effective mass value to the saturation density of the Shen EOS, see Eq. (5.3), labeled as "SkShen".

The EOS tables are created using the open-source code from Ref. [122, 125]. We also implement an effective mass in the original code from LS [120, 178], and compare our results, see Ref. [154]. We find precise agreement among the two codes. The Shen EOS is taken from Ref. [89, 124]. For every EOS table, we create neutrino opacity tables for the M1 neutrino transport scheme, using the routines from Ref. [74, 114], see also Sec. 3.4.1.

	m^*/m	K [MeV]	E_sym [MeV]	L [MeV]	n_0 [fm^{-3}]	B [MeV]
LS220	1.0	220	29.3	73.7	0.155	16.0
$m^*_{0.8}$	0.8	220	29.3	79.3	0.155	16.0
m^*_S	0.634	220	29.3	86.5	0.155	16.0
$(m^*, K)_\mathrm{S}$	0.634	281	29.3	86.5	0.155	16.0
$(m^*, E_\mathrm{sym})_\mathrm{S}$	0.634	220	36.9	109.3	0.155	16.0
$(m^*, K, E_\mathrm{sym})_\mathrm{S}$	0.634	281	36.9	109.3	0.155	16.0
SkShen	0.634	281	36.9	109.4	0.145	16.3
Shen	0.634	281	36.9	110.8	0.145	16.3

Table 5.2.: Summary of EOS parametrizations investigated in this work. Note that the effective mass of the SkShen EOS is re-fitted to the different value of the saturation density. The slope parameter L is not an input in the Skyrme parameters, but emerges from the other nuclear matter properties. We add it for completeness.

The impact of variations in the effective mass and nuclear matter properties is shown in Fig. 5.3. We present the energy per particle and pressure as a function of density for cold nuclear matter, i.e., $T = 0$. For vanishing temperature, the free energy is equal to the internal energy, and the pressure is given by the derivative of the energy with respect to density, see also Eq. (4.6).

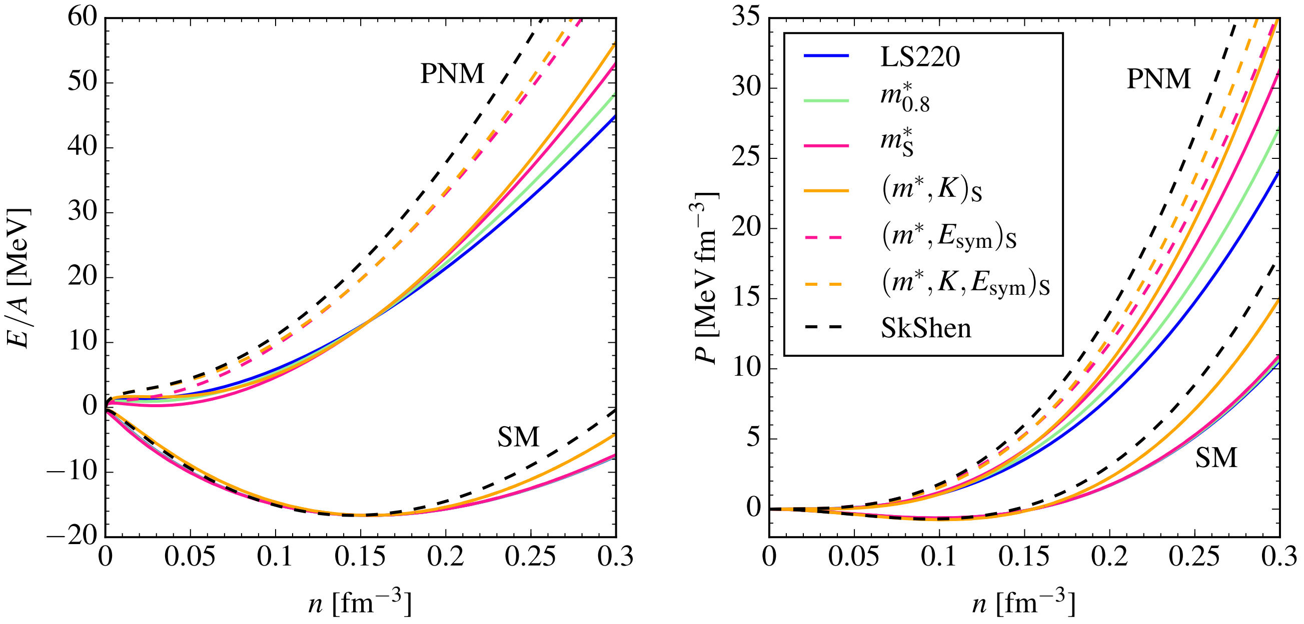

Figure 5.3.: Energy per particle and pressure as a function of number density for cold nuclear matter with the variations of nuclear matter properties considered in this work. Thanks to Sabrina Schäfer for providing the plotting routine.

The effective mass has minor impact on the energy per particle of symmetric matter and thus the corresponding pressure. For pure neutron matter, energy and pressure increase with $m^*/m < 1$ above saturation density. A larger value for the incompressibility, model $(m^*, K)_{\mathrm{S}}$, impacts the curvature of symmetric matter, as indicated in Fig. 5.2, thus resulting in a higher pressure for symmetric matter as well as pure neutron matter. Variations in the symmetry energy, model $(m^*, E_{\mathrm{sym}})_{\mathrm{S}}$, affect the energy difference of pure neutron matter to symmetric matter at saturation density, resulting in the same modification in pressure, see also Fig. 5.2. Changing the incompressibility and symmetry energy simultaneously, model $(m^*, K, E_{\mathrm{sym}})_{\mathrm{S}}$, simply combines the effects discussed above. In the SkShen model, the saturation density and corresponding binding energy are modified on top of the previous changes. This shifts the energy per particle curve for symmetric matter and pure neutron matter to smaller densities. As a result, the pressure at given density is larger compared to all the other models.

5.3 Impact of the effective mass

As a first step, we perform CCSN simulations with the EOS tables that have different effective masses. Pressure roughly follows the relation $P \sim 1/m^*$, therefore we expect a smaller effective mass, i.e., $m^*/m < 1$, to increase the pressure, as seen in Fig. 5.3, which results in a smaller density. This presumably changes the radius of the PNS.

The evolution of the PNS and shock radius for the three different effective mass scenarios together with the Shen EOS is presented in Fig. 5.4. We find that decreasing the effective mass impacts the PNS evolution significantly. Smaller effective masses result in a slower contraction of the PNS, which affects the shock propagation.

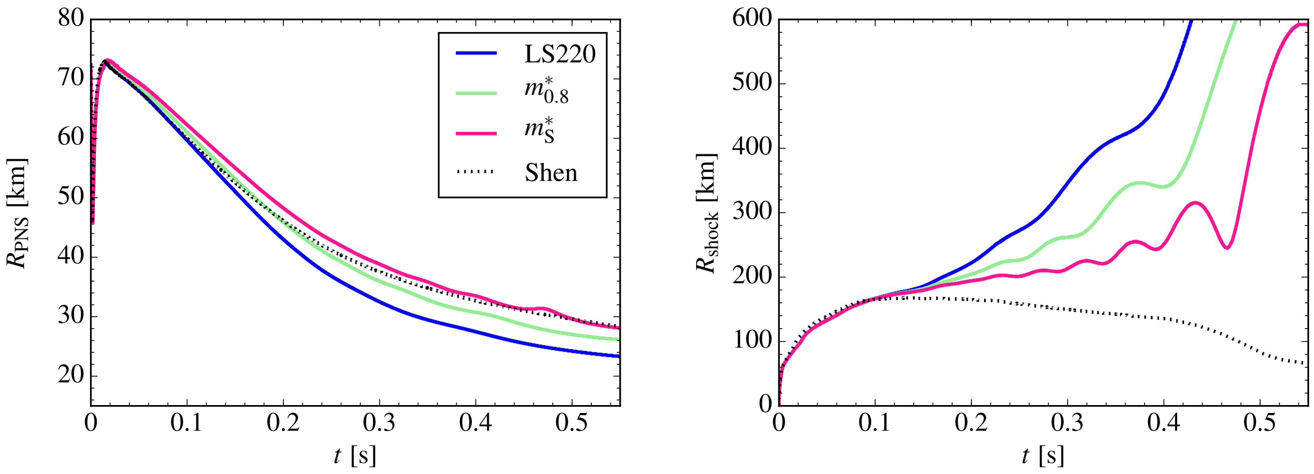

Figure 5.4.: Evolution of the PNS radius (left) and shock radius (right) for three EOS with different effective masses, and the Shen EOS.

The contraction behavior can be linked to pressure and density in the interior of the PNS. In Fig. 5.5, we depict the central pressure as a function of density, and the evolution of the central density. Decreasing the effective mass increases the pressure above saturation density, as already observed in Fig. 5.3. The pressure directly impacts the density, where smaller pressures allow higher central densities. As the PNS contracts, the central density increases with time.

Note that the central pressure within the simulation does not exactly agree with Fig. 5.3, as matter in CCSN simulations cannot be considered to be cold, i.e., $T \neq 0$. Additionally, supernova matter also includes electrons, positrons, and photons. However, the pressure for cold matter already provides insights into the properties within the PNS.

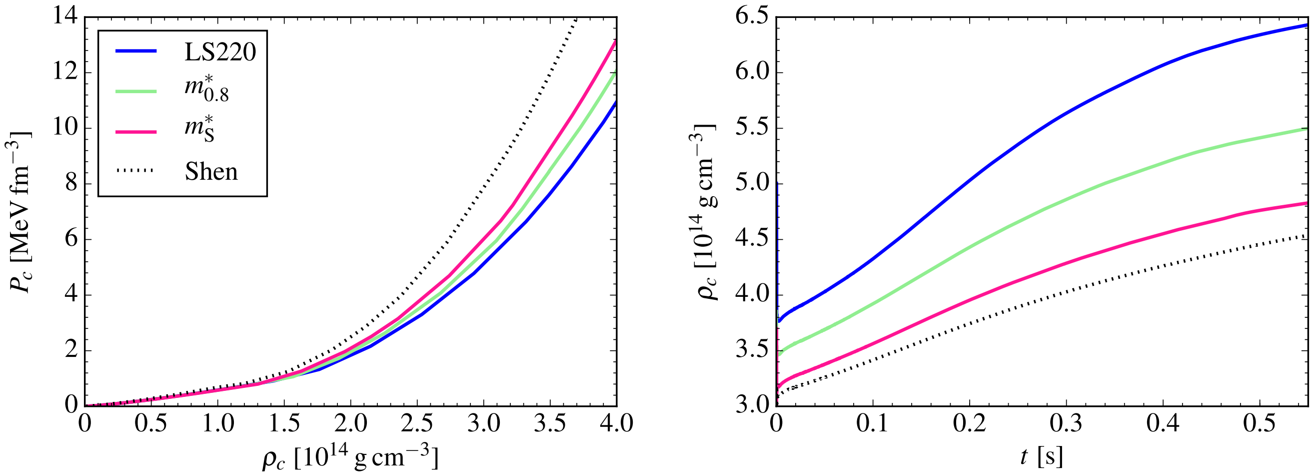

Figure 5.5.: Central pressure as a function of density (left) and evolution of the central density (right).

Further, we find that towards the end of the simulation ($t \sim 0.5$ s), the PNS radius of the simulation performed with the effective mass value that is equivalent to the value used in the Shen EOS, model m^*_{S}, approaches the radius of the original Shen EOS. This does not hold for earlier times ($t \sim 0.2$ s), where the PNS radius of the Shen EOS rather matches the effective mass scenario $m^*_{0.8}$. Note that this may be influenced by a different mass accretion, we address this in Sec. 5.7.1. Even though the effective mass scenario with m^*_{S} approximately reproduces the PNS radius of the original Shen EOS, the simulation still results in a successful explosion in contrast to the Shen EOS. In the following, we vary other EOS parameters to investigate possible reasons for the differences in the shock behavior as well as PNS interior.

5.4 Variation of nuclear matter properties

We present our results for variations of the incompressibility K, symmetry energy E_{sym}, and nuclear saturation point together with the previously discussed effective mass scenarios and the Shen EOS in Fig. 5.6.

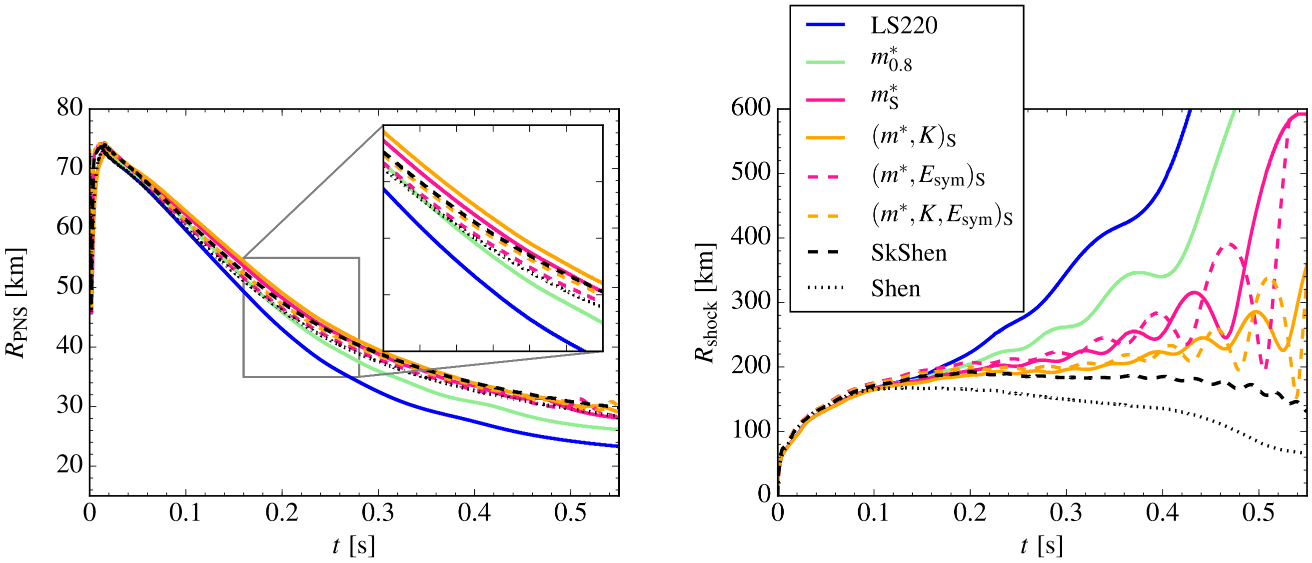

Figure 5.6.: Evolution of PNS (left) and shock radius (right) for variations of all nuclear matter properties.

We first focus on the impact of changing the incompressibility K on top of the effective mass. A larger value for the incompressibility increases the PNS radius slightly, which can be seen in the inset in Fig. 5.6, model $(m^*,K)_{\mathrm{S}}$. Variations in K modify the curvature of the energy per particle, discussed in Fig. 5.2. When the incompressibility increases, the curvature becomes more pronounced, resulting in an increase in pressure. This holds for pure neutron matter as well as symmetric matter, see also Fig. 5.3. Thus, increasing the incompressibility results in a stiffer EOS and hence smaller central density. The effect of changing the incompressibility has been discussed in the framework of the LS EOS, see also Refs. [120, 161, 177]. However, the impact on the PNS radius is smaller compared to the impact of the effective mass. As a result, the shock evolution is less energetic than for the m^*_{S} model, which can be attributed to slightly smaller neutrino energies.

Increasing the symmetry energy, model $(m^*,E_{\mathrm{sym}})_{\mathrm{S}}$, slightly decreases the PNS radius within the first 350 ms. The impact is relatively small and has minor effect on the shock evolution. The symmetry energy defines the energy difference between pure neutron matter and symmetric matter at saturation density. Thus, increasing the symmetry energy also results in a larger energy per particle for neutron matter. As a consequence, the pressure of pure neutron matter for EOS with a larger symmetry energy increases. However, changes in the symmetry energy affect the electron fraction, which we discuss in Fig. 5.7.

Varying symmetry energy and incompressibility simultaneously, model $(m^*,K,E_{\mathrm{sym}})_{\mathrm{S}}$, combines the effects discussed above. We observe that the shock evolution can be summarized into four different groups. One group for each effective mass scenario, where the effective mass scenario m^*_{S} forms one subgroup together with changes in the symmetry energy $(m^*,E_{\mathrm{sym}})_{\mathrm{S}}$, and another subgroup for changes in the incompressibility and symmetry energy on top of that, as indicated by the colors. However, all of these models still result in a successful explosion.

Finally, the SkShen model changes all parameters to the corresponding Shen EOS values. This model is as similar as possible to the Shen EOS in terms of the nuclear physics input. We notice that the radius of the PNS is larger compared to the radius obtained with the original Shen EOS. This model does not result in a successful explosion within the first 500 ms. The shock radii of the SkShen and Shen EOS still differ, suggesting additional differences among the two EOS.

To gain further insights into the differences observed in Fig. 5.6, we investigate density, temperature, entropy, and electron fraction in the center of the PNS in Fig. 5.7. The central density is governed by the central pressure, see also Fig. 5.8. Decreasing the effective mass results in larger pressures. Changing the incompressibility to the higher value of the Shen EOS increases the pressure further, thus resulting in a smaller central density. The symmetry energy has moderate impact. Finally, modifying the saturation point decreases the density, due to larger pressures, see also Fig. 5.3.

The entropy of the core before, during, and after collapse is slightly impacted by the effective mass. As neutrinos in the center are trapped, entropy is conserved with values around unity [179]. The entropy obtained with the Shen EOS is noticeably smaller, as it does not include the kinetic entropy contribution from heavy nuclei [121]. The incompressibility has minor impact. We observe that a larger value for the symmetry energy increases the central entropy. The entropy depends on changes in the electron fraction [179, 180]:

$$T\,\mathrm{d}S = -\mathrm{d}Y_e\left[\mu_e - (\mu_n - \mu_p) - \frac{3}{5}\Delta\right], \tag{5.8}$$

where Δ denotes the maximum energy available for electron capture. Neutron and proton chemical potentials are determined by the symmetry energy [181]:

$$E_{\mathrm{sym}} \sim \frac{1}{4\beta}(\mu_n - \mu_p), \tag{5.9}$$

with the asymmetry parameter $\beta = (N-Z)/A = x_n - x_p$.

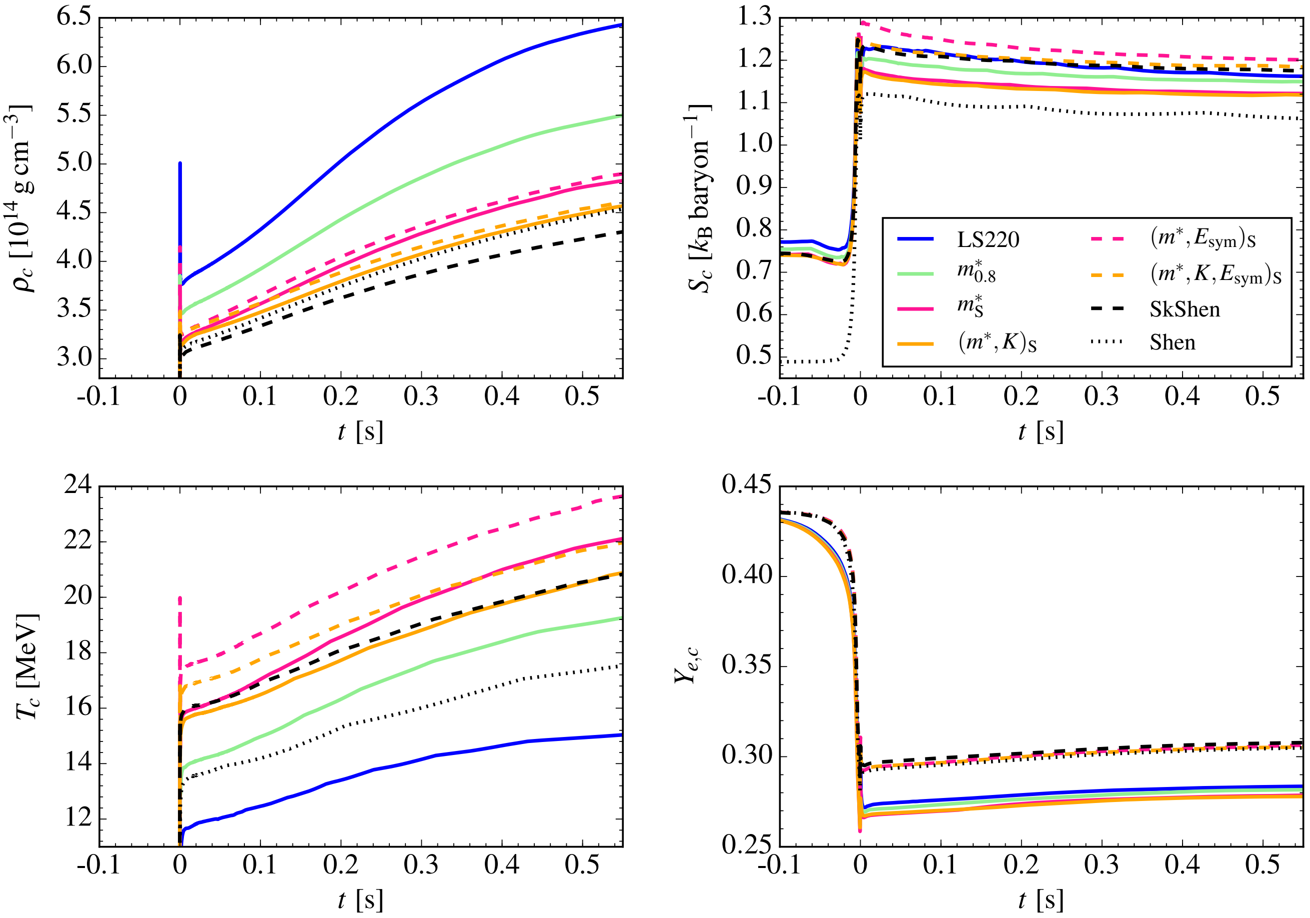

Figure 5.7.: Evolution of density (upper left), entropy (upper right), temperature (bottom left), and electron fraction (bottom right) in the PNS interior.

A higher symmetry energy favors a conversion from neutrons to protons. This agrees with our findings that modifying the symmetry energy increases the electron fraction, thus resulting in a larger central entropy. The models with a larger value for the symmetry energy obtain the same electron fraction as with the original Shen EOS.

The behavior of the central temperature follows Fermi-liquid theory [182]:

$$S \sim m^* \, T \, \rho^{-2/3} \,. \tag{5.10}$$

Note that the central entropy is approximately equal for all performed simulations, with the exception of the Shen EOS. Thus, the EOS with the largest effective mass (LS220) exhibits the lowest central temperature. Decreasing m^*/m raises the temperature. The modified incompressibility results in slightly smaller temperatures. Additionally, we find that the enlarged symmetry energy increases the central temperature, which can be attributed to changes in the central entropy. The temperature obtained with the Shen EOS is relatively small, due to the absence of the kinetic entropy contribution from nuclei. This has consequences for the PNS evolution and neutrino emission.

5.5 Thermal effects and cold neutron stars

The simulations performed with modified nuclear matter properties show that the PNS contraction is mainly governed by the effective mass. However, the impact of the effective mass in cold matter is not as pronounced as the PNS radii suggest. In this section, we investigate the thermal contributions to the EOS.

Pressure and energy density $\varepsilon = \rho(1 + \epsilon/m)$, with internal energy ϵ, can be divided into a cold and a thermal contribution [183]:

$$P = P_{\text{cold}} + P_{\text{th}} \,, \tag{5.11}$$

$$\varepsilon = \varepsilon_{\text{cold}} + \varepsilon_{\text{th}} \,. \tag{5.12}$$

The thermal component of the pressure is related to the thermal index and the energy density via:

$$P_{\text{th}} = (\Gamma_{\text{th}} - 1)\varepsilon_{\text{th}} \,. \tag{5.13}$$

Solving for the thermal index and inserting Eqs. (5.11) – (5.12) yields:

$$\Gamma_{\text{th}} = 1 + \frac{P_{\text{th}}}{\varepsilon_{\text{th}}} = 1 + \frac{P - P_{\text{cold}}}{\varepsilon - \varepsilon_{\text{cold}}} \,. \tag{5.14}$$

The properties of cold matter can be obtained post-processing simulation data. To calculate P_{cold} and $\varepsilon_{\text{cold}}$, we interpolate pressure and internal energy from the EOS table for the corresponding density and electron fraction, taking the lowest value for the temperature available in the table, i.e., $T \sim 0.01\,\text{MeV}$. We use the baryonic part of the EOS table, meaning electrons, positrons, and photons are not included in this calculation.

We present the central pressure and the thermal index as a function of density in Fig. 5.8. The central pressure also includes contributions from leptons and photons. However, it approximately follows the hierarchy already discussed for pure neutron matter in Fig. 5.3. Smaller effective masses increase the pressure. A larger value for the incompressibility, on top of the effective mass changes, enhances the pressure above saturation density further. The same holds for modifications in the symmetry energy. The pressure obtained with SkShen model approximately agrees with the Shen EOS.

The thermal index for densities above of the phase transition, $\rho \gtrsim 0.5\, n_0$, only depends on the effective mass. Below saturation density, matter is non-uniform and nuclei are present, which changes Γ_{th}. Larger effective masses yield a smaller thermal index, as indicated in Fig. 5.8. Note that the thermal index for the SkShen models looks slightly different, since the effective mass is fitted to a smaller value of the saturation density.

For an ideal gas of non-relativistic particles, the thermal index solely depends on the density-dependent effective mass (see, e.g., Ref. [184]):

$$\Gamma_{\mathrm{th}}^{\text{n-rel}} = \frac{5}{3} - \frac{n}{m^*}\frac{\partial m^*}{\partial n}\,, \tag{5.15}$$

implying that the thermal index increases for smaller effective masses. Equation (5.15) is indicated as the gray bands in Fig. 5.8, and our models entirely agree. This links the contraction behavior of the PNS to the thermal contribution at nuclear densities, which is determined by the effective mass. The Shen EOS, which is based on a relativistic theory, is not in accordance with this model.

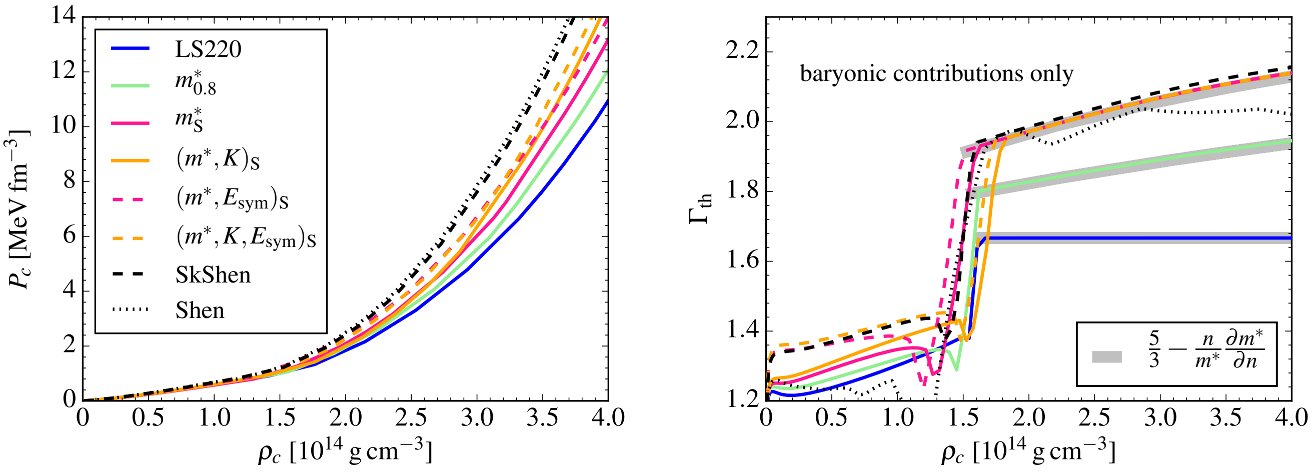

Figure 5.8.: Central pressure (left) and thermal index (right) for the performed simulations. Note that we do not include leptons and photons in the calculation of the thermal index.

We additionally verify that the constructed EOS give reasonable modifications to the mass-radius (MR) relation. To this end, we compute the Tolman-Oppenheimer-Volkoff (TOV) equations [63] at $T = 0.1$ MeV and vanishing neutrino chemical potential, see also Refs. [122, 154]. The MR curves for our EOS models and the Shen EOS are presented in Fig. 5.9.

Modifications in the effective mass show minor impact in the MR curve. We find a small increase of the maximum mass as well as the radius. Since the curve is calculated at $T = 0.1$ MeV, the characteristics agree with the previously discussed properties of pressure for cold matter in Fig. 5.3. The same holds for the incompressibility, model $(m^*, K)_{\mathrm{S}}$, where a larger value for K results in a larger pressure, thus supporting a higher maximum mass. Variations in the symmetry energy have a noticeable effect on the radius in the MR curve, see model $(m^*, E_{\mathrm{sym}})_{\mathrm{S}}$ and $(m^*, K, E_{\mathrm{sym}})_{\mathrm{S}}$. Increasing the symmetry energy results in a larger radius. The SkShen model shows an even higher maximum mass and radius. The radius approximately agrees with the Shen EOS, whereas the mass obtained with the SkShen model is relatively large. Within our modifications the results are consistent with the findings in pure neutron matter, where the SkShen model shows the largest pressure due to the modified saturation point.

We conclude that the maximum mass is slightly impacted by the effective mass, and rather determined by the incompressibility. Variations in the symmetry energy change the radius in the MR curve. Modifying the saturation point further increases the corresponding radius. We additionally plot an uncertainty band from chiral effective field theory calculations with a polytropic expansion [127], shown in gray. As the symmetry energy in the Shen EOS is relatively high and not in agreement with recent constrains, also the radii obtained with that value for the symmetry energy are relatively large. The $2\,M_{\odot}$ constraint from Refs. [28, 29, 135] is fulfilled by all models, as pressures increase for varying nuclear matter properties from LS220 to Shen.

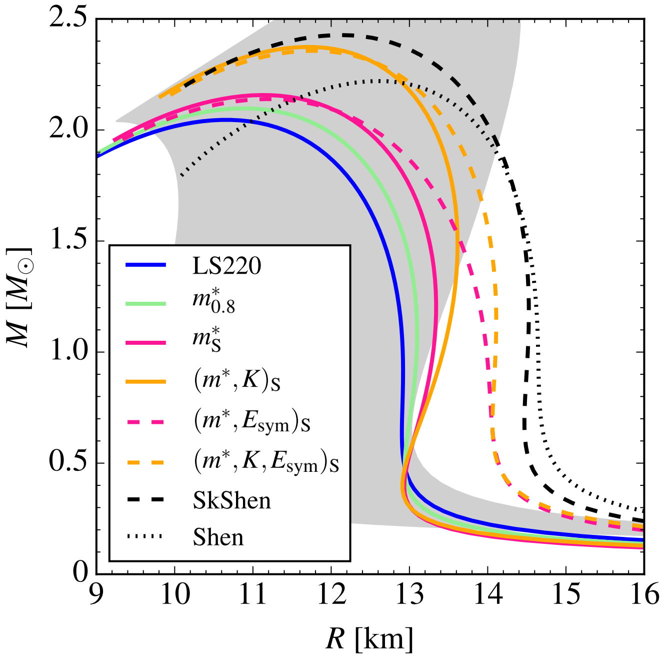

Figure 5.9.: Mass-radius relation for cold ($T = 0.1$ MeV) neutron stars in beta equilibrium for the various EOS models. The gray band depicts an uncertainty band from Ref. [127].

5.6 Explosion properties

We investigate the explosion properties in the simulations performed with our various EOS models. The previous discussion attributed the different shock behavior to the neutrino energies. Neutrinos decouple thermally approximately at the surface of the PNS, implying that the neutrino energy hierarchy roughly follows the PNS radii. However, the PNS contraction behavior with the Shen EOS approximately agrees with our model that employs the Shen effective mass value, still the Shen EOS does not result in a successful explosion. In the following, we investigate possible reasons for this.

The net neutrino heating rate Q_gain in the gain region is presented in the left panel of Fig. 5.10. Note that we focus on the first 300 ms, as this is the interval where the shock propagation starts to differ. At $t \sim 0.15$ s, the energy deposition is highest for the LS220 model with the largest effective mass. This is followed by the two other effective mass models. The modified incompressibility, model $(m^*, K)_\mathrm{S}$, shows a smaller energy deposition, together with the varied symmetry energy. The SkShen and Shen EOS exhibit the lowest Q_gain.

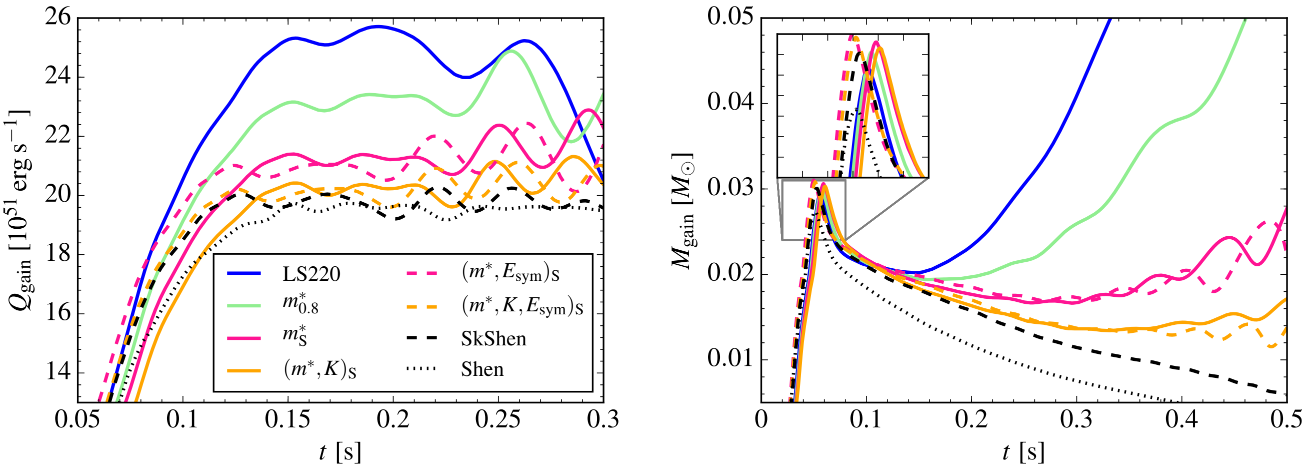

Figure 5.10.: Energy deposition by neutrinos in the gain layer (left) and mass in the gain layer (right).

This agrees with the fact that the simulations performed with the SkShen and Shen EOS do not result in a successful explosion. The hierarchy of energy deposition is similar to the shock behavior shown in Fig. 5.6 but does not correlate with the PNS radii. Note that the heating rate is relatively high, as we artificially enhance the energy deposition by neutrinos.

We additionally show the mass in the gain region M_{gain} in Fig. 5.10. For the Shen EOS and the SkShen model, the mass in the gain layer is smaller compared to the other models, see the inset in Fig. 5.10. This might be one of the possible reasons for the lower energy deposition. For the exploding models, the masses grow as soon as the shock expands. Since the gain region is defined up to the shock position, the layer grows with increasing shock radii, thus including more mass.

The energy deposition gives insight into the explosion behavior. However, the hierarchy does not agree with the obtained PNS radii. We further investigate the average electron neutrino energy E_{ν_e} in Fig. 5.11. At approximately $t \sim 0.15$ s, the LS220 EOS exhibits the largest average energy, which presumably is a result of the smallest PNS radius. It is followed by the Shen EOS, which agrees with the contraction behavior within the first 150 ms. The average energies obtained with our other models follow the hierarchy of the PNS radii at the corresponding time, as also indicated in Fig. 5.6. Decreasing the effective mass, as well as enlarging the incompressibility, pushes the PNS radius farther out, resulting in smaller neutrino energies. Changing the symmetry energy yields smaller PNS radii, due to the modified electron fraction, which is also correlated with the corresponding average neutrino energies. As the PNS contracts, the average electron neutrino energies rise. We conclude that although the average electron neutrino energies follow the PNS radii, the mass in the gain region differs and thus the neutrino energy deposition, which depends on both quantities combined, results in a different shock behavior.

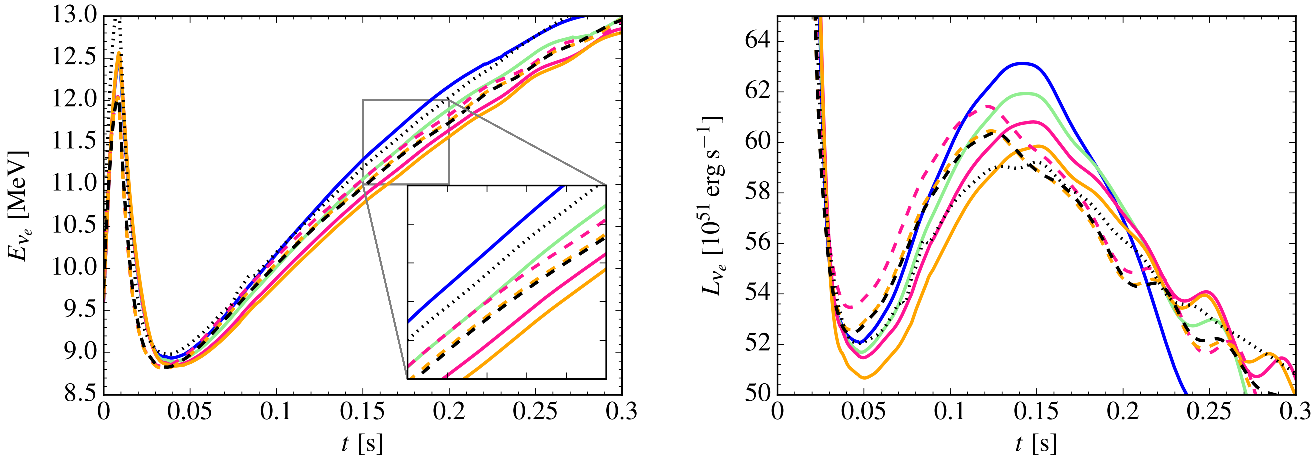

Figure 5.11.: Average electron neutrino energy (left) and electron neutrino energy luminosity (right). For a legend please refer to the other plots.

The average electron neutrino energy luminosities L_{ν_e} in Fig. 5.11 show a slightly different behavior compared to the electron neutrino energies. We observe two different maxima, which can be divided into two groups depending on the symmetry energy. Within the corresponding peak, the luminosities again agree with the PNS radii. Further, the luminosity obtained with the Shen EOS is relatively small compared to the other models. This may be an additional factor why the Shen EOS does not result in a successful explosion. The neutrino burst is visible within the approximately first 50 ms, see Chapter 2. Neutrino energies as well as luminosities look similar for the electron antineutrinos.

We conclude this section by comparing the mass accretion rate $\dot{M}_{\text{acc}}$ at 500 km and PNS mass in Fig. 5.12. Note that we start the plot of the mass accretion rate pre-bounce. The simulation performed with the Shen EOS shows a larger accretion rate for $t < 0$ s compared to all the other EOS models. This can possibly be attributed to a different deleptonization of the collapsing material, as the entropy differs, see also Fig. 5.7 and Tab. 5.3. We observe two peaks for the different symmetry energy groups, as already discussed for the electron neutrino energy luminosity in Fig. 5.11. After collapse, models with a higher symmetry energy exhibit slightly smaller mass accretion rates.

The different mass accretion rates also impact the mass of the PNS in Fig. 5.12. We can again identify two different groups related to the symmetry energy. After the onset of the explosion, the PNS masses start to saturate, i.e., at around $t \sim 0.3\,\mathrm{s}$ for the LS220 EOS.

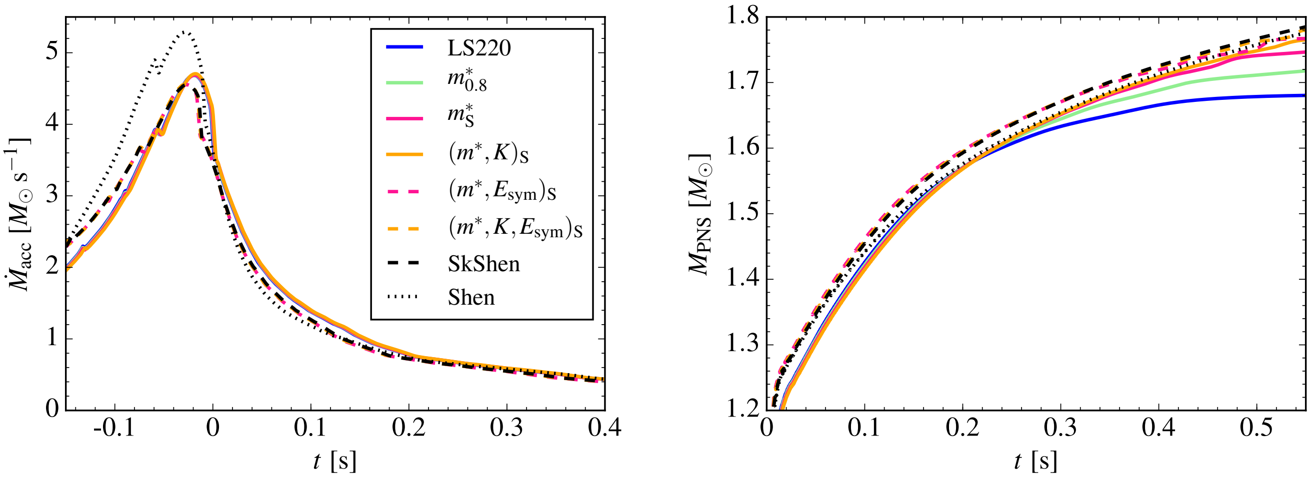

Figure 5.12.: Mass accretion rate at 500 km (left) and PNS mass evolution (right).

The deleptonization impacts the collapse phase and the mass accretion rate. The time of bounce t_{bounce} for our various EOS models is given in Tab. 5.3. The three effective mass scenarios, LS220, $m^*_{0.8}$, and m^*_{S}, together with a modified incompressibility, model $(m^*, K)_{\mathrm{S}}$, have a similar bounce time, which also agrees with the electron fraction in Fig. 5.7. The electron fraction in combination with the entropy determines the deleptonization of the collapsing star, affecting the collapse, see also Sec. 3.4.2. A larger value for the symmetry energy, models $(m^*, E_{\mathrm{sym}})_{\mathrm{S}}$ and $(m^*, K, E_{\mathrm{sym}})_{\mathrm{S}}$, delays the time of bounce, which can be attributed to the higher electron fraction. The simulation performed with Shen EOS has the earliest bounce time, presumably due to the small entropy.

	LS220	$m^*_{0.8}$	m^*_{S}	$(m^*, K)_{\mathrm{S}}$	$(m^*, E_{\mathrm{sym}})_{\mathrm{S}}$	$(m^*, K, E_{\mathrm{sym}})_{\mathrm{S}}$	SkShen	Shen
t_{bounce} [ms]	273.6	273.7	273.4	271.5	291.6	288.9	283.4	219.2

Table 5.3.: Time of bounce for the different EOS models.

5.7 Investigation in GR1D

The previously discussed simulations were performed with the FLASH code and an M1 neutrino transport scheme. The FLASH code is a Newtonian code, see also Sec. 3.2. It utilizes a gravitational potential that includes modifications from general relativity. In this section, we verify our results with GR1D, a different CCSN simulation code that formulates the Eulerian equations of hydrodynamic in a framework based on general relativity, see Sec. 3.3. As the PNS is a highly compact object, relativistic corrections are relevant. With results from the two different codes, we are also able to check the gravitational potential that is implemented in FLASH, see also Ref. [82].

We perform spherically symmetric simulations with the GR1D code [74, 89], and the same 15 $M_\odot$ progenitor [36]. Moreover, we employ the M1 neutrino transport scheme from Refs. [74, 105] with the same neutrino opacity tables used previously [74, 114]. We also perform simulations with a neutrino leakage scheme from Refs. [42, 89, 102], with an artificial heating factor of 1.24, and use the deleptonization from Ref. [92]. This allows us to compare the two different neutrino treatments. We use the same seven EOS models except for SkShen. The EOS tables are created using the open-source code from Ref. [122, 125]. All technical simulation details can be found in Appendix A.

5.7.1 M1

We present our results for the PNS radius and shock evolution in Fig. 5.13. As we did not enhance the energy deposition by neutrinos for this simulation performed with the M1 transport scheme, no successful explosion for any of the models are obtained. Note that the resolution that has been applied in these simulations is lower compared to the previous results.

The evolution of the PNS radii agrees with the results obtained with the FLASH code and an artificial explosion. This confirms our conclusion that the PNS contraction behavior is mainly determined by the effective mass. Note that towards the end of the simulation ($t \sim 0.4$ s), the PNS radius of the simulation performed with the effective mass value that is equivalent to the value used in the Shen EOS again approaches the radius from the original Shen EOS, model m^*_S. We observe that shock radii within the first 100 ms are slightly larger for the EOS with the varied symmetry energy, models $(m^*, E_\mathrm{sym})_\mathrm{S}$ and $(m^*, K, E_\mathrm{sym})_\mathrm{S}$.

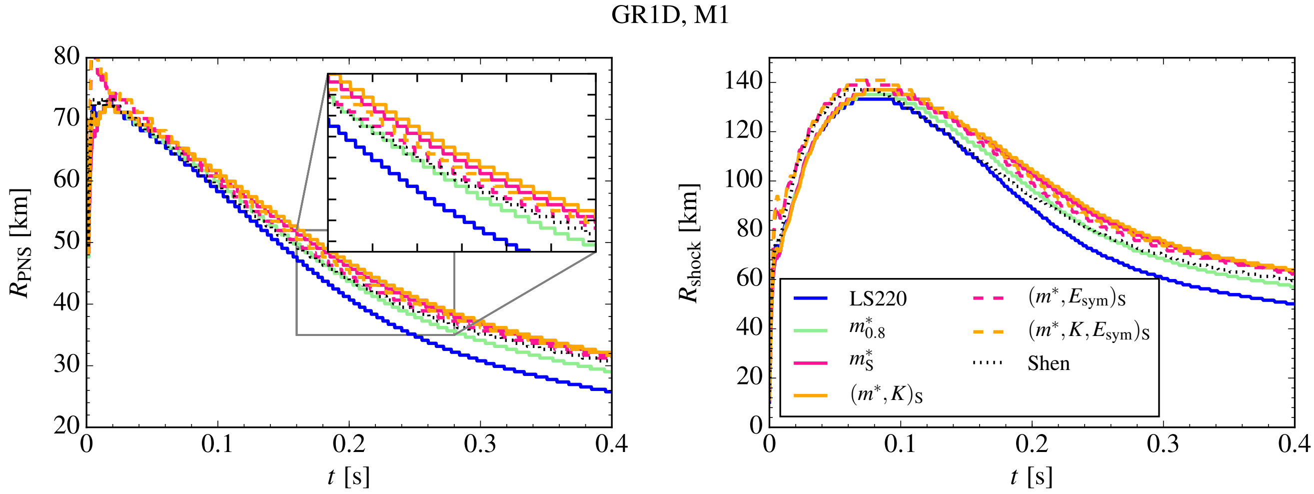

Figure 5.13.: Evolution of the PNS (left) and shock radius (right) in simulations performed with GR1D.

We further investigate the PNS interior in Fig. 5.14. The behaviour of all central quantities is the same as already observed in the simulations performed with FLASH. Additionally, even absolute numbers in the center of the PNS agree for density, entropy, temperature, and electron fraction.

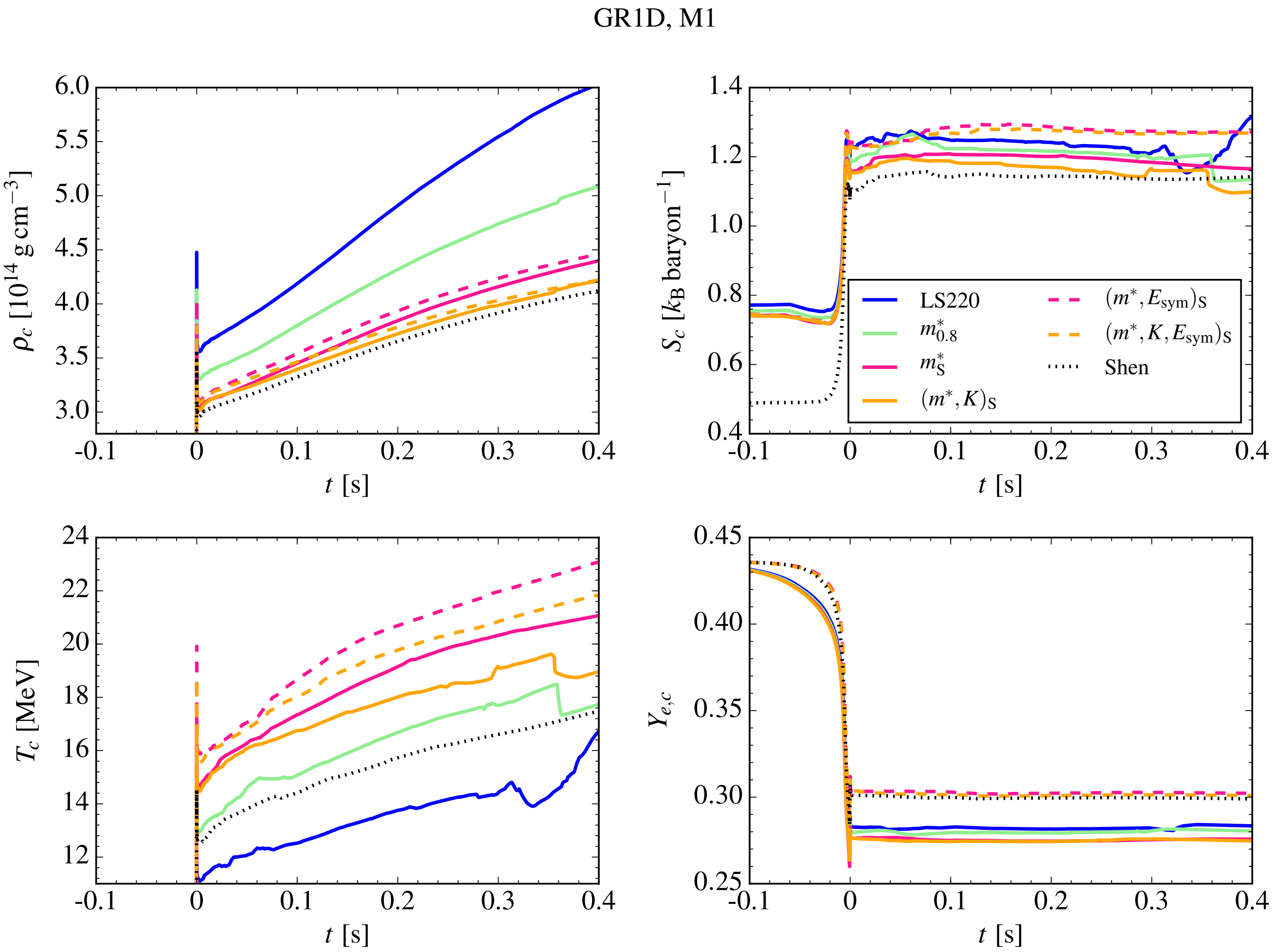

Figure 5.14.: Central density (upper left), entropy (upper right), temperature (bottom left), and electron fraction (bottom right) in simulations performed with GR1D and M1.

5.7.2 Leakage

We further investigate our EOS models in the same simulation environment, GR1D, with a simplified neutrino transport scheme. Using the neutrino leakage from Refs. [42, 89, 102], and the deleptonization treatment from Ref. [92], simulations are performed with a heating factor of 1.24, see also Sec. 3.4.2.

The evolution of PNS and shock radii is presented in Fig. 5.15. We find that simulations performed with the neutrino leakage show a slightly different contraction behavior compared to results obtained with a full neutrino transport. While the PNS radius evolution still follows the same behavior among the effective mass models, as well as the one with the modified incompressibility, radii obtained for EOS with a varied symmetry energy are larger compared to results with M1. Also, the PNS contraction obtained with the Shen EOS is slower. The PNS radius agrees with the effective mass model m^*_S that is equivalent to the Shen EOS. For all EOS models, the overall contraction is faster than in the previous cases.

The shock evolution also varies compared to the results obtained with M1. All shock radii agree within the first 100 ms and no differences, e.g., for the varied symmetry energy, are visible. Additionally, the shock propagation groups differently compared to our findings with M1 in FLASH. Here, the hierarchy of the shock energetics follows the contraction behavior of the PNS, except for the Shen EOS. Further, the model with a larger value for the incompressibility and symmetry energy, model $(m^*, K, E_{sym})_S$, does not result in a successful explosion.

Our results with the neutrino leakage scheme suggest that the PNS interior looks different compared to simulations performed with M1. The cooling of the PNS via neutrinos highly depends on the neutrino treatment. We investigate central density, entropy, temperature, and electron fraction in Fig. 5.16.

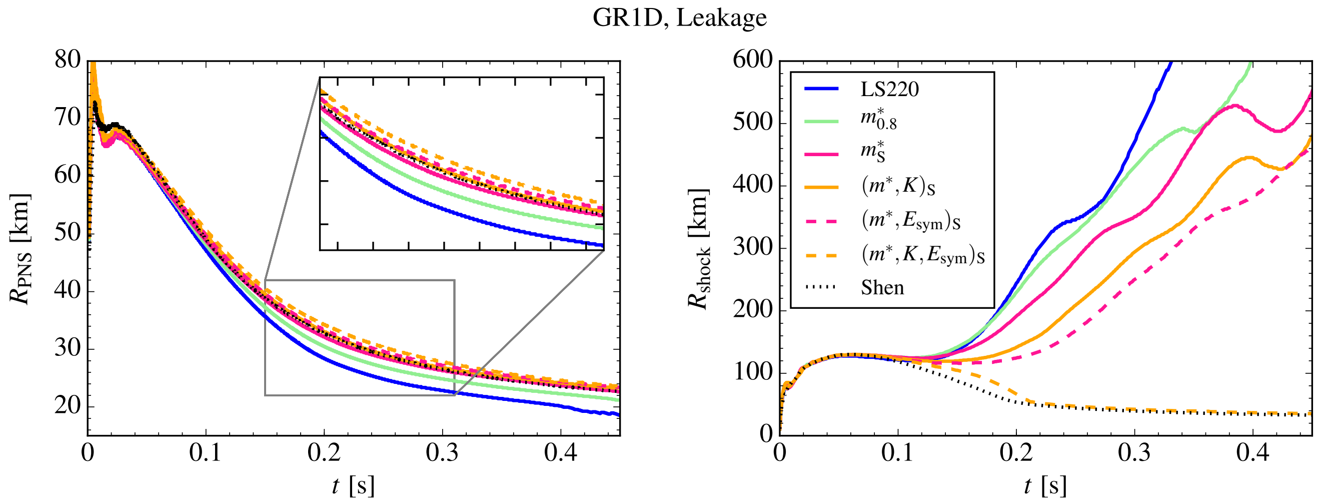

Figure 5.15.: Evolution of the PNS (left) and shock radius (right) for simulations performed with a neutrino leakage scheme in GR1D. The results do not agree with the previous findings.

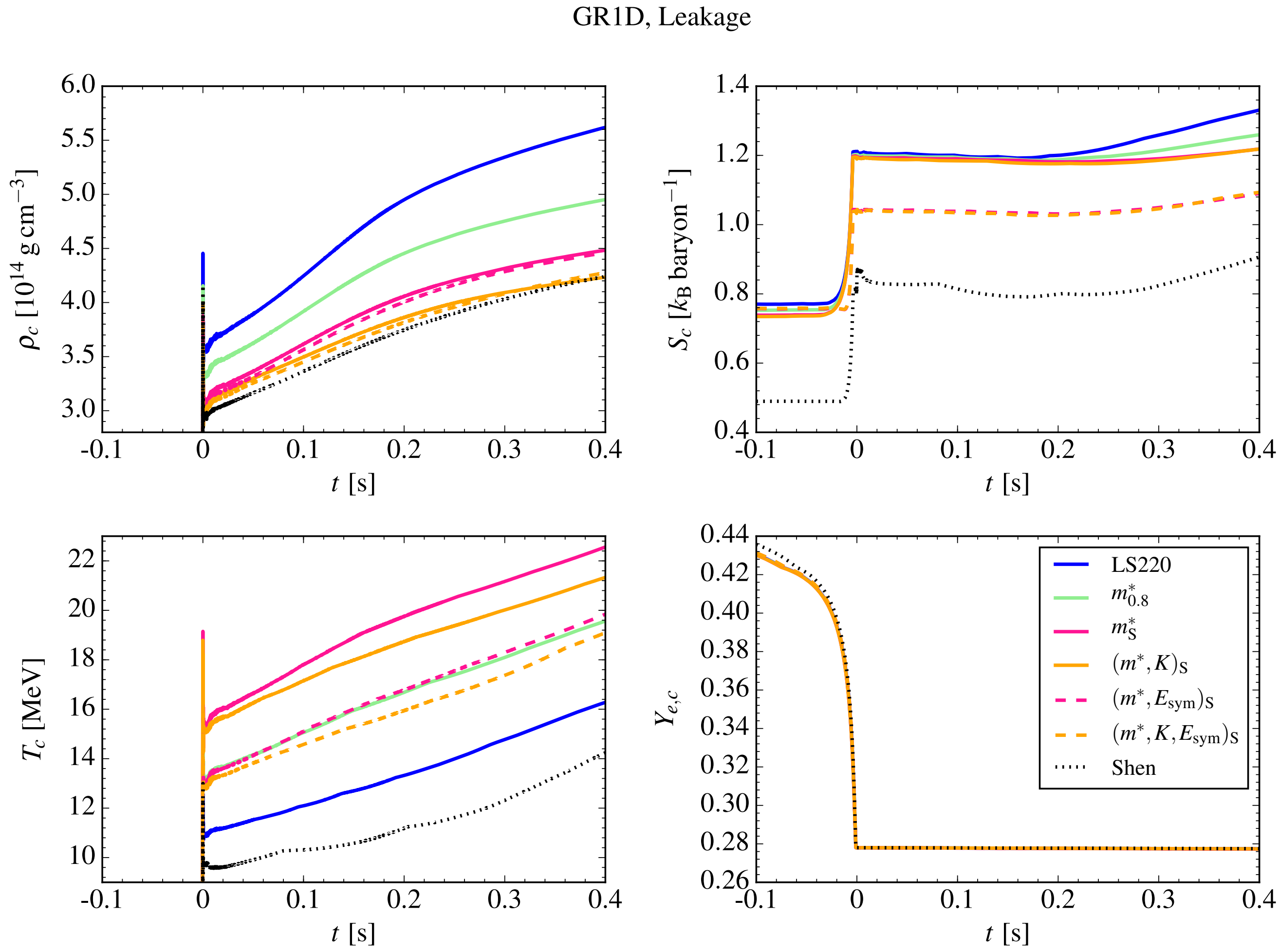

Figure 5.16.: Central density (upper left), entropy (upper right), temperature (bottom left), and electron fraction (bottom right) for simulations performed with a neutrino leakage scheme in GR1D. The electron fraction is smaller for models with a varied symmetry energy compared to results with M1, as a consequence of the employed deleptonization scheme. As a result, also entropy and temperature vary.

The central density approximately agrees with the previous results, however, the absolute numbers are smaller compared to the cases with M1. This can be attributed to the different cooling behavior of the PNS with the neutrino leakage.

Further, we observe that the central entropy is different compared to our results with M1. Especially the entropy obtained with the Shen EOS is smaller than in Fig. 5.14. This is a result of the different electron fraction, also depicted in Fig. 5.16. For all models, the value of the electron fraction is the same, independent of the symmetry energy. This is a consequence of the deleptonization scheme that is employed in combination with the neutrino leakage. To compute the electron fraction, the deleptonization scheme from Ref. [92] constructs an electron fraction profile as a function of density, see also Sec. 3.4.2. This sets a minimum value for the electron fraction at densities above $\rho \sim 10^{13}\,\mathrm{g\,cm^{-3}}$, when neutrino trapping during collapse occurs. As a result, the electron fraction has the same minimum value for all EOS models.

This results in the differences we find in the central entropy. The presumably too low values of the electron fraction for cases with enlarged symmetry energy also leads to a smaller central entropy compared to results obtained with a full neutrino transport. Especially the Shen EOS, which does not include the kinetic entropy of heavy nuclei [121], shows significantly smaller entropies, which also results in smaller temperatures, as presented in Fig. 5.16. While the models without modified symmetry energy approximately agree with the previous results, the central temperatures are nonetheless overestimated. This suggests that the cooling behavior of the PNS cannot be reproduced accurately with the neutrino leakage.

We conclude that simulations performed with a neutrino leakage cannot reproduce accurate electron fractions and are thus not able to capture important effects regarding modifications in the symmetry energy. Additionally, entropy and temperature change as a result of the deleptonization scheme, implying that predictions regarding the PNS interior require an accurate neutrino transport.

5.7.3 Leakage with modified electron fraction

The investigation of EOS effects using a neutrino leakage scheme suggests that accurate predictions regarding the PNS interior are not possible. However, the deleptonization scheme allows that the minimum value for the electron fraction for densities above $\rho \sim 10^{13}\,\mathrm{g\,cm^{-3}}$ can be modified. In the following, we adapt the electron fraction that is obtained with the corresponding M1 transport scheme and change it individually for every EOS model. This reproduces the particular electron fraction obtained with M1 and consequently affects the central entropy and temperature. We present the simulation results with the modified electron fraction for the PNS and shock evolution in Fig. 5.17. The changes in the electron fraction impact the contraction behavior of the PNS. The radii are more consistent with the simulations performed with M1, although the overall contraction of the PNS is again faster. This suggests that small modifications in the electron fraction modify the interior of the PNS.

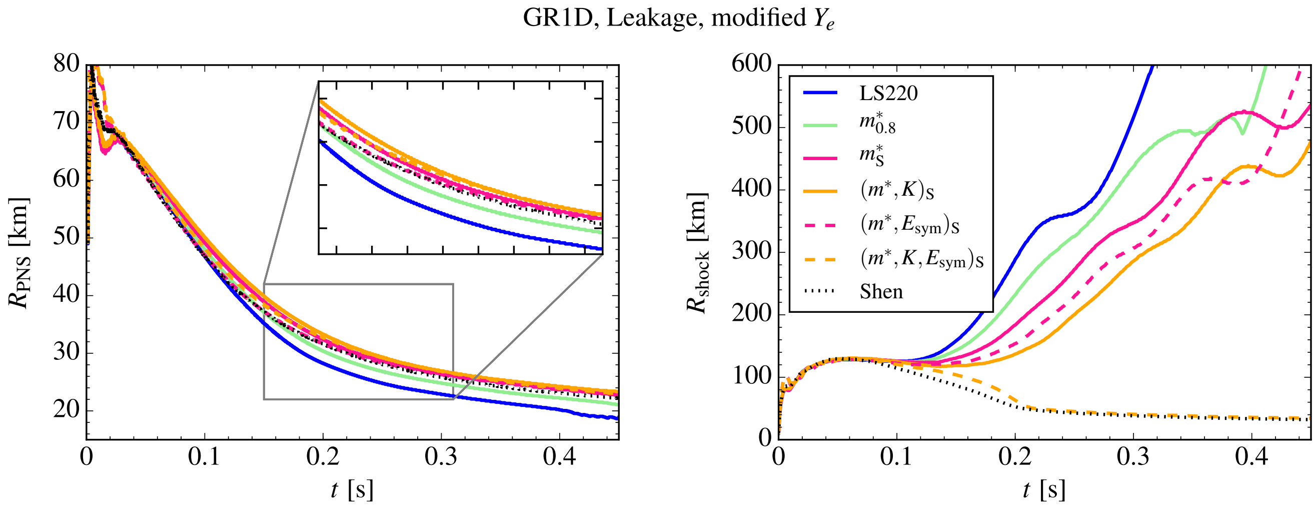

Figure 5.17.: PNS (left) and shock radius evolution (right) for simulations performed with a modified electron fraction for the neutrino leakage scheme in GR1D.

However, the evolution of the shock radii still looks similar to the cases obtained with the "unmodified" neutrino leakage. The shock evolution is not correlated with the PNS contraction as it is for the leakage results, and the model with modified incompressibility and symmetry energy, model $(m^*, K, E_{\mathrm{sym}})_{\mathrm{S}}$, still does not result in a successful explosion. Overall, the shock evolution does not seem to be affected by changes of the central electron fraction.

We further investigate changes in the PNS interior with the modified electron fraction in Fig. 5.18. Variations in the electron fraction affect the central density, temperature, and entropy. The models with enlarged symmetry energy, model $(m^*, E_{\mathrm{sym}})_{\mathrm{S}}$ and $(m^*, K, E_{\mathrm{sym}})_{\mathrm{S}}$ exhibit slightly larger densities compared to the previous results. Still, absolute values of the central density are smaller compared to results obtained with M1.

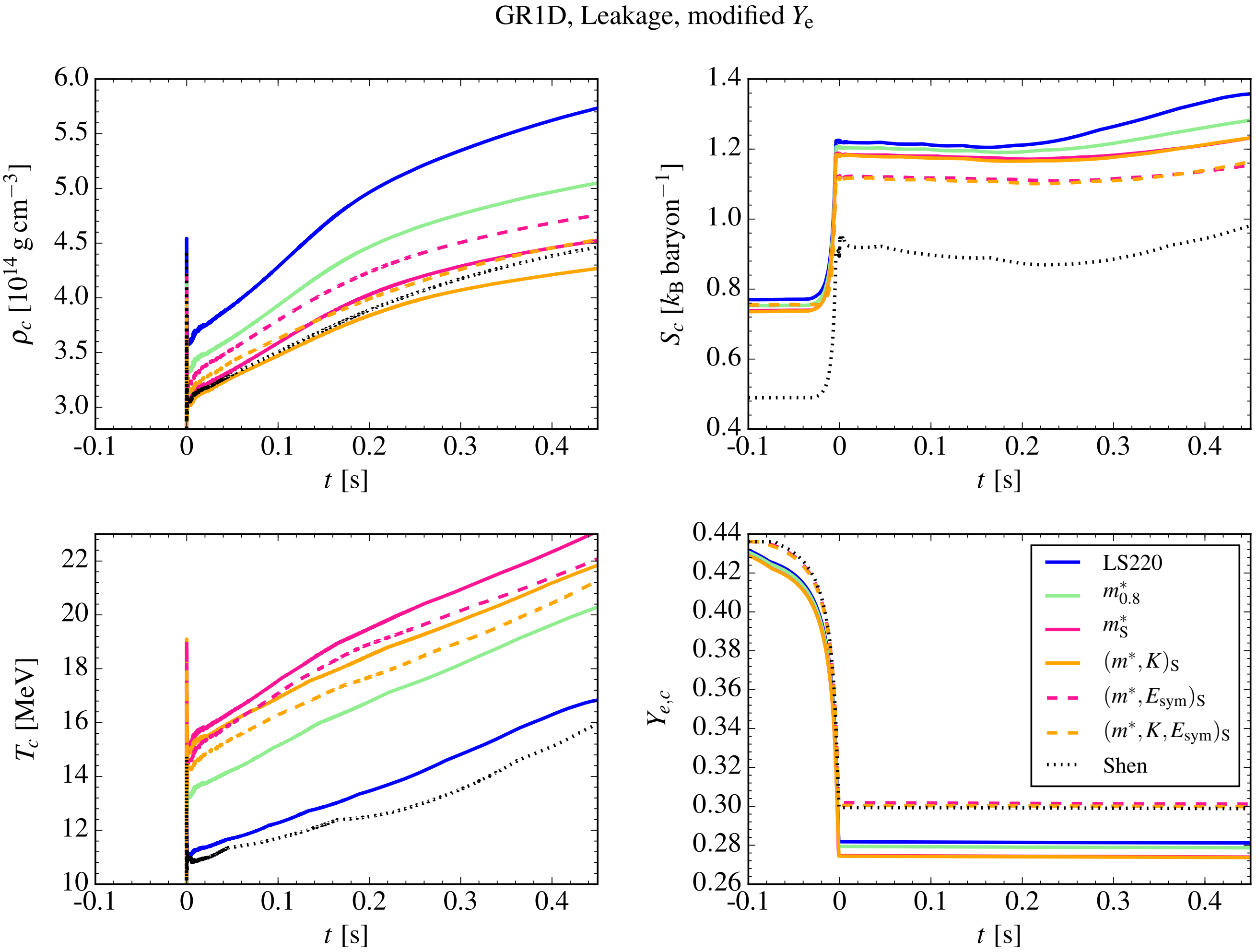

Figure 5.18.: Central density (upper left), entropy (upper right), temperature (bottom left), and electron fraction (bottom right) for simulations performed with a modified electron fraction in GR1D.

The central entropy is yet not in agreement. Although the entropy is larger for models $(m^*, E_{\mathrm{sym}})_{\mathrm{S}}$ and $(m^*, K, E_{\mathrm{sym}})_{\mathrm{S}}$, there is still no agreement with the hierarchy obtained with M1. The same holds for the central entropy obtained with the Shen EOS, which is smaller compared to M1 results. The changes in entropy also affect the temperature. As the entropy for the models with the enlarged symmetry energy is smaller compared to the entropy obtained with M1, also the central temperatures are underestimated. This is presumably one of the reasons why the model $(m^*, K, E_{\mathrm{sym}})_{\mathrm{S}}$ does not result in a successful explosion, in contrast to our findings with M1. It appears that adapting the minimum electron fraction to values obtained with a full neutrino transport is not sufficient to reproduce characteristic features in the PNS interior. We conclude that investigations of EOS effects, especially cases that modify the symmetry energy, rely on a full neutrino transport in order to be able to capture the relevant changes in the underlying physical properties. Finally, the gravitational potential in FLASH captures relativistic effects, as already discussed in Ref. [82].

6 Equation of State Transition

In this chapter, we discuss a transition from a high-density equation of state to one that is applicable at low densities. Such a transition is necessary for long-time simulations of core-collapse supernovae. The conditions that are encountered when the shock propagates from the center to the outer layers of the star span a wide range in density and temperature. Therefore, a description of matter in all of these different configurations is necessary. In the following, we discuss the challenges that occur for such a transition, introduce our formalism, and present results.

6.1 Introduction

In core-collapse supernova (CCSN) simulations, densities span ranges from $10^{-2}\,\mathrm{g\,cm^{-3}}$ up to $10^{15}\,\mathrm{g\,cm^{-3}}$, temperatures reach from $10^{6}\,\mathrm{K}$, and less, to $10^{12}\,\mathrm{K}$, and the electron fraction can take values between $0.05-0.7$. One of the main challenges for simulations is to have the equation of state (EOS) available for all these conditions, see also Chapter 4. For nuclear densities, EOS models are applied, which require numerically expensive calculations. It is therefore quite common to use pre-calculated EOS tables, and interpolate the required values, as this is computationally favorable. However, these tables have a lower boundary, which limits the simulation domain.

Simultaneously, for the outer layers of the star, with comparably small densities, $\rho < 10^{6}\,\mathrm{g\,cm^{-3}}$, and temperatures, the EOS is understood and can easily be calculated analytically. Further, these analytical calculations have no lower limit, as is the case for tables. Ideally, one would use EOS tables for high densities and transition to analytical calculations once specific contributions from the nuclear EOS are negligible. In the following, we present our approach for implementing such a transition.

The EOS is usually derived from the Helmholtz free energy F, which can be written as the sum of the contributions from different particles in the system, see also Chapter 4:

$$F = F_{\mathrm{nucleons}} + F_{\mathrm{nuclei}} + F_{e^-} + F_{e^+} + F_{\gamma}\,, \tag{6.1}$$

where F_{nucleons}, F_{nuclei}, F_{e^-}, F_{e^+}, and F_{γ} denote the free energy of unbound nucleons, nuclei, electrons, positrons, and photons, respectively. Depending on the conditions, different constituents become important or may vanish, e.g., F_{nucleons} is relevant at nuclear densities, but vanishes for small densities, as nucleons are bound in nuclei. An overview for the individual contributions can be found in Chapter 4. For densities below nuclear density, physical properties are well described within theories and investigated in experiments. Most of the contributions can be calculated analytically, and are commonly summarized in the Helmholtz EOS [171]:

$$F_{\mathrm{Helmholtz}} = F_{\mathrm{ion}} + F_{e^-} + F_{e^+} + F_{\gamma}\,, \tag{6.2}$$

where the F_{nuclei} part in Eq. (6.1) reduces to the contribution from ions F_{ion}, see also Sec. 4.5 for more details. Nuclear EOS tables are usually constructed such that they transition into the Helmholtz EOS. This crossing is seamless for pressure and entropy. However, calculating the internal energy poses a challenge for the transition. In the nuclear EOS, the contribution from nuclei in the internal energy E_{nuclei} includes a term for the binding energy. This is not the case for the Helmholtz EOS, where the nuclei component simply contains the ion contribution. The calculation of the binding energy depends on the composition, where the details of the treatment vary with every EOS model. To illustrate the differences, we show pressure, internal energy (including a FLASH-specific energy shift, discussed below), and entropy as a function of density for a nuclear EOS (Lattimer & Swesty EOS with an incompressibility of 220 MeV, further denoted as LS220) and the Helmholtz EOS in Fig. 6.1. The profiles are calculated for representative conditions in a CCSN simulation, 300 ms after bounce.

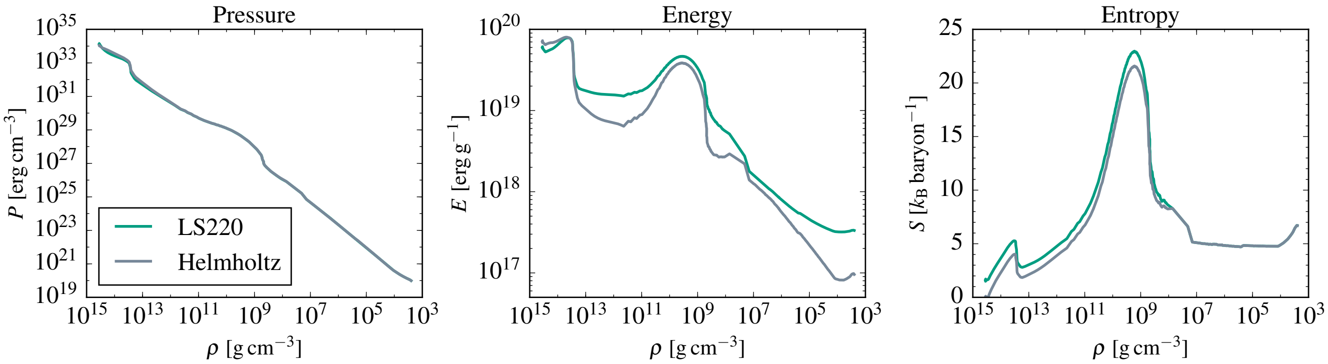

Figure 6.1.: Pressure, internal energy, and entropy as a function of density for representative conditions in a CCSN simulation for a nuclear EOS (LS220) and the Helmholtz EOS.

While pressure and entropy mostly agree within the valid region for the Helmholtz EOS, approximately up to $\rho \sim 10^{11}\,\mathrm{g\,cm^{-3}}$ [171], the internal energy shows large differences between the two EOS, due to the missing binding energy. A simple switch between the EOS, neglecting the binding energy contribution, is not possible. When solving the Eulerian equations of hydrodynamics, see Sec. 3.1, large differences in a quantity can lead to unphysical oscillations and cause numerical problems [77]. Therefore, a smooth transition is necessary, which we discuss in the following.

6.2 Transition

Ideally, one would calculate the binding energy within the simulation and add it to the Helmholtz internal energy. This requires a nuclear reaction network that provides the composition of the star. But even if such a reaction network is used, the binding energy would most likely not agree with the binding energy that is computed in the nuclear EOS. Most reaction networks in supernovae simulations are reduced networks, meaning they consider a small amount of isotopes (around 20 in FLASH [77]). However, the majority of the recent nuclear EOS evaluate the binding energy using nuclear statistical equilibrium (NSE) calculations with more than 5000 nuclei (see, e.g., Ref. [162]). In addition, nuclear EOS define their internal energies with respect to different rest masses, e.g., the LS220 uses the neutron mass m_n [120], while others use the atomic mass m_u [136, 156, 162], resulting in noticeably different values. This makes it difficult to generalize such a computation.

6.2.1 Requirements

For our transition between the two EOS regimes, we skip the calculation of the binding energy and chose a purely numerical approach. This is not the "physically correct" way, since the binding energy is not taken into account, but the difference is estimated so that the transition works numerically in the simulation. Further, there arises a problem that is simulation-dependent: The hydrodynamics solver in the FLASH code requires positive values for the internal energy. However, the internal energy can become negative when the binding energy is the dominant contribution, see Sec. 4.5. To handle this, EOS tables for FLASH shift all internal energies upwards by a constant *energy shift*, such that all entries are values above zero [89]. This has to be included in the treatment of the transition.

We impose the following requirements for the numerical transition. The transition has to work for all available high-density EOS tables. It should be functional for different neutrino schemes, for example an approximation like a neutrino leakage or a full neutrino transport, see Sec. 3.4. As we will use information from the progenitor star for the calculation of the transition, it has to be independent of the chosen progenitor. The transition onset is determined by a density criterion. The density, where the transition starts is arbitrary, as well as where the transition stops. Additionally, we introduce parameters that allow for a fine-tuning, if desired, which we discuss in the following section. All of these quantities can be changed, but we also provide default values that have been tested extensively.

6.2.2 Formalism

This formalism is specifically developed for the FLASH code. It utilizes the fact that values of the internal energy in the nuclear EOS are always greater than the internal energy from the Helmholtz EOS, as a result of the energy shift. The idea is to calculate the difference between the nuclear EOS and the Helmholtz at the transition density, further denoted as *offset*, and then slowly decrease this offset such that it vanishes once the lower end of the transition region is reached. The formalism is designed as follows:

1. Chose a density, where the transition starts $\rho_{\text{transition}}$ and a lower density, where the transition stops ρ_{stop}. We recommend to select this transition region within one order of magnitude, at least half a magnitude - default values are provided ($\rho_{\text{transition}} = 5 \cdot 10^5\,\text{g}\,\text{cm}^{-3}$, $\rho_{\text{stop}} = 1 \cdot 10^5\,\text{g}\,\text{cm}^{-3}$).
2. Decide how quickly the additional offset should exponentially decrease, within the transition region. We recommend around two orders of magnitude (default value is $\textit{decrease} = 1 \cdot 10^{-2}$) such that the offset contribution is negligible compared to the internal energy of the Helmholtz EOS.
3. Compute the exponential decline parameter α so that it corresponds to the decrease that has been chosen:

$$\exp\left(-\frac{\log_{10}\left(\rho_{\text{transition}}\right) - \log_{10}\left(\rho_{\text{stop}}\right)}{\alpha}\right) \approx \textit{decrease}\,, \tag{6.3}$$

$$\Rightarrow \alpha = \left(\frac{\log_{10}\left(\rho_{\text{stop}}\right) - \log_{10}\left(\rho_{\text{transition}}\right)}{\ln\left(\textit{decrease}\right)}\right). \tag{6.4}$$

The difference in the internal energy between the nuclear EOS and the Helmholtz EOS can be quite large, see Fig. 6.1. In order to reduce this difference, and make the transition less susceptible to possible oscillations, we shift the internal energy from the Helmholtz EOS by a constant energy shift c_{shift}, analogous to the energy shift introduced in the nuclear EOS tables. It is not trivial how to determine a shift that is functional for all available EOS tables, since it is crucial that it is not overestimated. If overestimated, the resulting Helmholtz internal energy including the shift might be larger than the one from the nuclear EOS. We present one possible way to estimate such a shift in the following.

The EOS can be written as a function of three parameters, which in our case will be density, temperature, and the electron fraction, see also Chapter 4. Their profiles are initially given by the conditions of the spherically symmetric progenitor star and then evolved within the simulation. When the star collapses, density and temperature increase significantly, also increasing pressure and internal energy, compared to the initial progenitor profiles. We can therefore use these progenitor conditions $(\rho, T, Y_e)_{\text{progenitor}}$ as a lower limit to approximate c_{shift}.

4. Determine the temperature and electron fraction of the progenitor at the transition density. Then, obtain the constant energy shift c_{shift} for the Helmholtz EOS from the progenitor input:

$$c_{\text{shift}} = E_{\text{int}}^{\text{nuclear}}(\rho, T, Y_e)_{\text{transition, progenitor}} - E_{\text{int}}^{\text{Helmholtz}}(\rho, T, Y_e)_{\text{transition, progenitor}}\,, \tag{6.5}$$

   ensuring that the internal energy from the Helmholtz EOS does not exceed the nuclear EOS. This step can be skipped, although we highly recommend it.

5. Calculate the difference *diff*(T, Y_e) between the internal energy of the high-density EOS and the Helmholtz EOS at the transition density and store the values in a table:

$$\textit{diff}(T, Y_e)\Big|_{\rho_{\text{transition}}} = E_{\text{int}}^{\text{nuclear}}(T, Y_e) - E_{\text{int}}^{\text{Helmholtz}}(T, Y_e) - c_{\text{shift}}\,. \tag{6.6}$$

   This is computed for all temperatures and all electron fractions available in the nuclear EOS table. It is later used as a look-up table for the individual conditions when the EOS is called in the simulation.

Note that the transition density has to be available in the high-density EOS table. All of the above steps are pre-requisites that are computed before the actual start of the simulation.

In the simulation, the EOS domain is divided into three parts. Densities above the transition density, where the nuclear EOS is called, densities within the transition region, and densities below the transition region $\rho < \rho_{\text{stop}}$.

In the transition region, the internal energy is calculated via:

$$E_{\text{int, transition}}(\rho, T, Y_e) = E_{\text{int}}^{\text{Helmholtz}}(\rho, T, Y_e) + \mathit{diff}(T, Y_e) \cdot \exp\left[\left(\log_{10}(\rho) - \log_{10}(\rho_{\text{transition}})\right)/\alpha\right] + c_{\text{shift}}\,, \tag{6.7}$$

combining all the parameters that are mentioned above. At the transition density, the resulting calculated internal energy is, per construction, equal to the internal energy from the nuclear EOS. The term that includes the difference and the exponential decline vanishes with smaller densities. In the following, we refer to that term as "offset function". Below the transition region ρ_{stop}, the internal energy reduces to:

$$E_{\text{int, below transition}}(\rho, T, Y_e) = E_{\text{int}}^{\text{Helmholtz}}(\rho, T, Y_e) + c_{\text{shift}}\,. \tag{6.8}$$

This approach allows that all of the computed terms can always be re-evaluated, also post-processing, if necessary. The constant offset shift is written to the output files of the simulation and all other parameters can be calculated if the two EOS are available. We present our results for this formalism in the following section.

Additional remark

The entropy in Fig. 6.1 shows differences among the two EOS at densities above $\rho \gtrsim 10^9\,\text{g}\,\text{cm}^{-3}$. For values below $\rho \sim 10^8\,\text{g}\,\text{cm}^{-3}$, both EOS agree. This is due to the construction of the applied EOS table, where the entropy is shifted such that the Helmholtz EOS agrees with the LS220 EOS at $\rho \sim 10^8\,\text{g}\,\text{cm}^{-3}$ [89]. However, the entropy is not used to evolve the hydrodynamics in the simulation, see Sec. 3.1, and thus small differences are not critical.

Nevertheless, the entropy is an input for the calculation of the deleptonization pre-bounce, when using the neutrino leakage, see Sec. 3.4.2. The deleptonization is computed down to density values of $\rho \sim 10^6\,\text{g}\,\text{cm}^{-3}$. Therefore, we advise to chose the transition density below that value, at least for simulations with a neutrino leakage.

6.3 Results

We discuss our findings for a simulation using the LS220 EOS [120] with a $20\,M_\odot$ progenitor from Ref. [185] in detail, and further investigate possible parameter sets, as well as different progenitors and various EOS models. All simulations are performed with the FLASH code [77, 161], using a neutrino gray leakage [102, 117, 118] with the deleptonization from Ref. [92], applying a heating factor (hf) to obtain artificial explosions, see Sec. 3.4.2. We refer to simulations that use the transition formalism as "Hybrid".

The transition for this first case is done from $\rho_{\text{transition}} = 5 \cdot 10^5\,\text{g}\,\text{cm}^{-3}$ to $\rho_{\text{stop}} = 1 \cdot 10^5\,\text{g}\,\text{cm}^{-3}$, using a decrease of 10^{-3}. In principle, the transition is possible everywhere. However, one should be certain that effects from the nuclear EOS are negligible. Further, we recommend considering the progenitor structure to ensure that the transition is not done between shell interfaces, so that the internal energy in the transition region is monotonic.

We present our results for the hybrid EOS in Fig. 6.2. Additionally, we perform the same simulation without transition, i.e., solely with the EOS table from Ref. [89], in order to be able to compare the results. The radial profiles of density, temperature, electron fraction (upper panel), and pressure, internal energy, and entropy (lower panel) are shown 100 ms after bounce[1].

---

[1] Note that the radius denotes the distance from the center of the star.

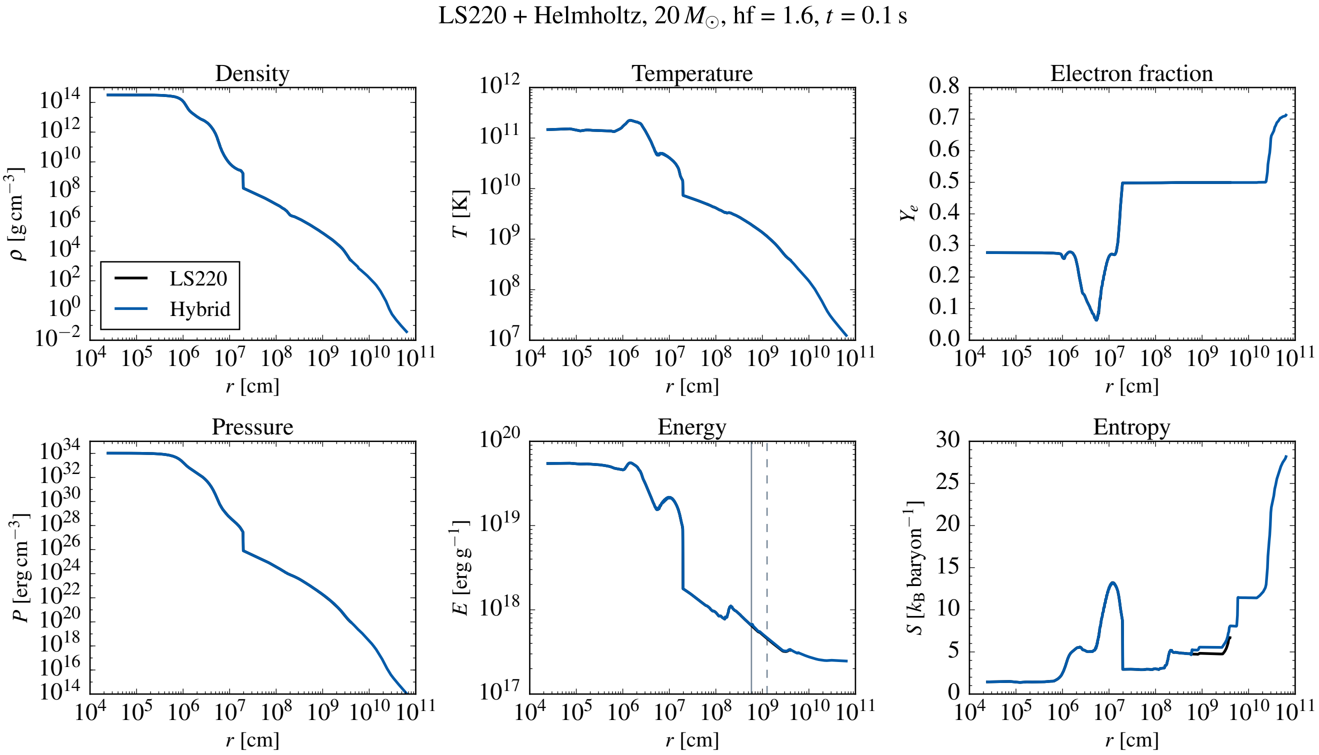

Figure 6.2.: Results for the hybrid EOS, together with simulation results from the original LS220. The gray vertical lines mark the start (solid) and end (dashed) of the transition region.

The results obtained with the nuclear EOS table and the hybrid EOS agree reasonably well. The transition region is marked in the panel of the internal energy. The vertical solid gray line indicates the radius where the transition density is located, and the vertical dashed gray line depicts the lower end of the transition region. In the entropy, minor variations are visible for radii outside the transition region. This is a result of the different average mass number $\bar{A}$ and average proton number $\bar{Z}$ that are used to describe nuclei in the ion contribution, see Sec. 4.5. As long as it is available, we let the nuclear EOS determine the composition. Below the transition region, the information is taken from the progenitor, yielding a slightly different composition. This allows us to exceed the limits of the nuclear EOS table, where the electron fraction in the available tables usually has an upper limit of $Y_{e,\mathrm{max}} \sim 0.55$. Ideally, a nuclear reaction network would determine the actual composition.

Density, temperature, pressure, and internal energy reach their maximum in the interior of the newly-formed, hot and dense proto-neutron star (PNS). The PNS radius is commonly defined as the radius where the density is equal to $10^{11}\,\mathrm{g\,cm^{-3}}$, around 70 km in Fig. 6.2. Density and temperature decrease with increasing radius, as the star becomes less compact. The shock is visible as the discontinuity at around 200 km. In front of the shock, the star still resembles the progenitor. Note that the profiles can be followed up to radii of roughly 600 000 km with densities down to $10^{-2}\,\mathrm{g\,cm^{-3}}$. The nuclear EOS table is limited to $\rho_\mathrm{low} \sim 10^3\,\mathrm{g\,cm^{-3}}$, which corresponds to a maximum simulation domain of about 40 000 km. This also confines the possible simulation time, since the simulation stops as soon as the shock leaves the domain.

We present our results for the same simulation, 5 s after bounce in Fig. 6.3. The heating factor was chosen to be relatively small, such that the shock is less energetic and still located in the smaller domain. A smaller value results in a failed explosion. With this, we are able to compare our results to the original EOS table when the shock has passed the transition region.

Again, both EOS agree and only minor differences are visible. There are some small variations, especially around the shock region, however, all relevant characteristics are reproduced. We notice that the electron fraction obtained with the hybrid EOS is slightly smaller than the one from the nuclear EOS once the shock has passed the transition region. This might again be related to the fact that the hybrid EOS assumes the composition of the progenitor below the transition region.

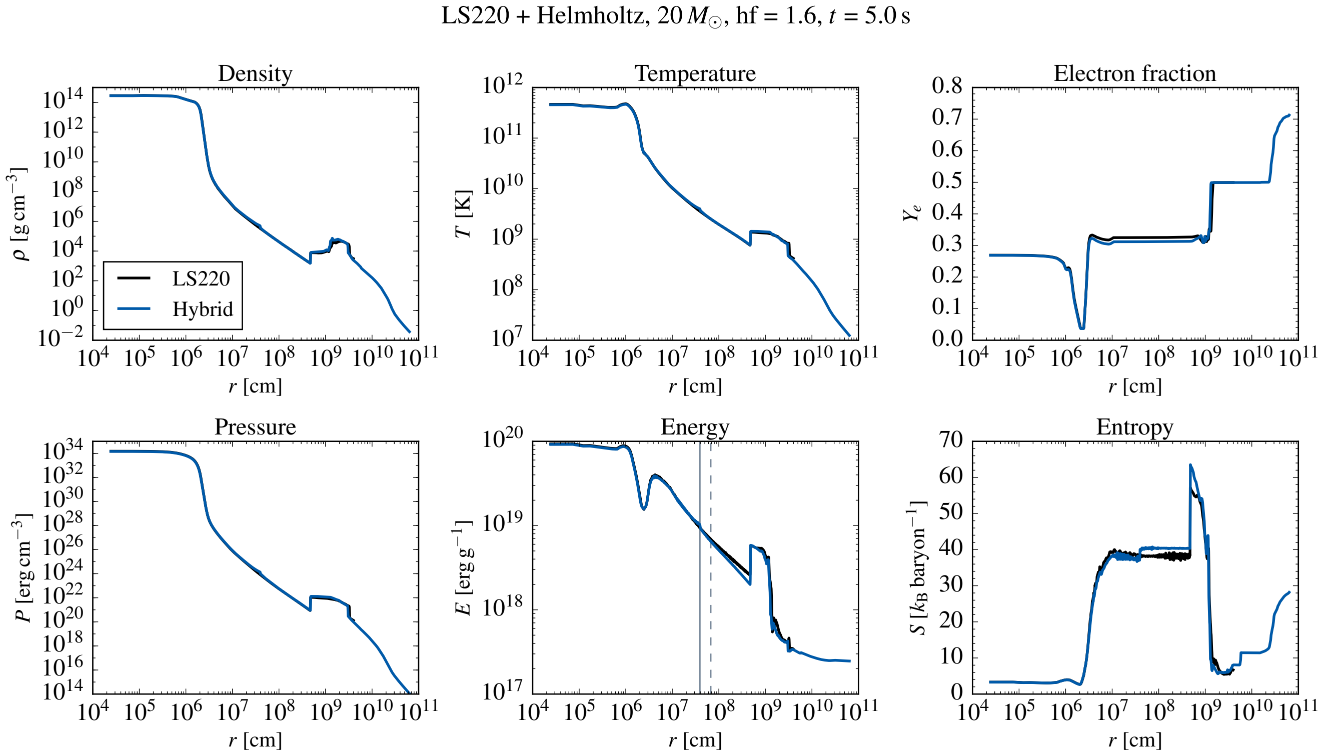

Figure 6.3.: Same as Fig. 6.2, but compared 5 s after bounce. Note that the transition region (gray vertical lines) moves to smaller radii as the PNS contracts.

There are additional differences in the internal energy. When the shock passes the lower end of the transition region, the internal energy is only calculated from the Helmholtz EOS, including the constant offset shift from the progenitor. It does not contain the contribution from the offset function with the exponential decrease, which roughly corresponds to the binding energy, which is used to match the transition. As a result, the internal energy is smaller compared to the nuclear EOS. Other than that, and the entropy differences already described above, the hybrid EOS reproduces all important features from the nuclear EOS, and transitions to the Helmholtz EOS, with no boundaries for the simulation domain.

6.3.1 Varying parameters

The results presented in the previous section are obtained with a transition region from $\rho_\mathrm{transition} = 5 \cdot 10^5\,\mathrm{g\,cm^{-3}}$ to $\rho_\mathrm{stop} = 1 \cdot 10^5\,\mathrm{g\,cm^{-3}}$, with a decrease of 10^{-3}. This parameter set, among others, reproduces the nuclear EOS results most accurately. The transition formalism allows a variation of both densities as well as the decrease. In the following, we discuss variations of these parameters.

As mentioned previously, we recommend considering the progenitor structure to make sure the transition is done in a relatively monotonic region, and not between shell interfaces. Further, we advise to chose the transition region large enough, such that the decrease is possible as a smooth transition and not a steep drop. This requires approximately half an order of magnitude for densities below $\rho = 1 \cdot 10^6\,\mathrm{g\,cm^{-3}}$, see Sec. 6.2.2. Additionally, the transition region should not be more than an order of magnitude, which we motivate in this section. Finally, the decrease should be small enough, such that the offset contribution vanishes, although too small values do not make a transition but rather a steep drop. It should also fit to the size of the transition region, e.g., larger transition regions can have a larger decrease.

We present our results for variations of the parameter sets, using the same simulation conditions as mentioned above, in Fig. 6.4. The radial profiles of the internal energy are shown 100 ms and 5 s after bounce.

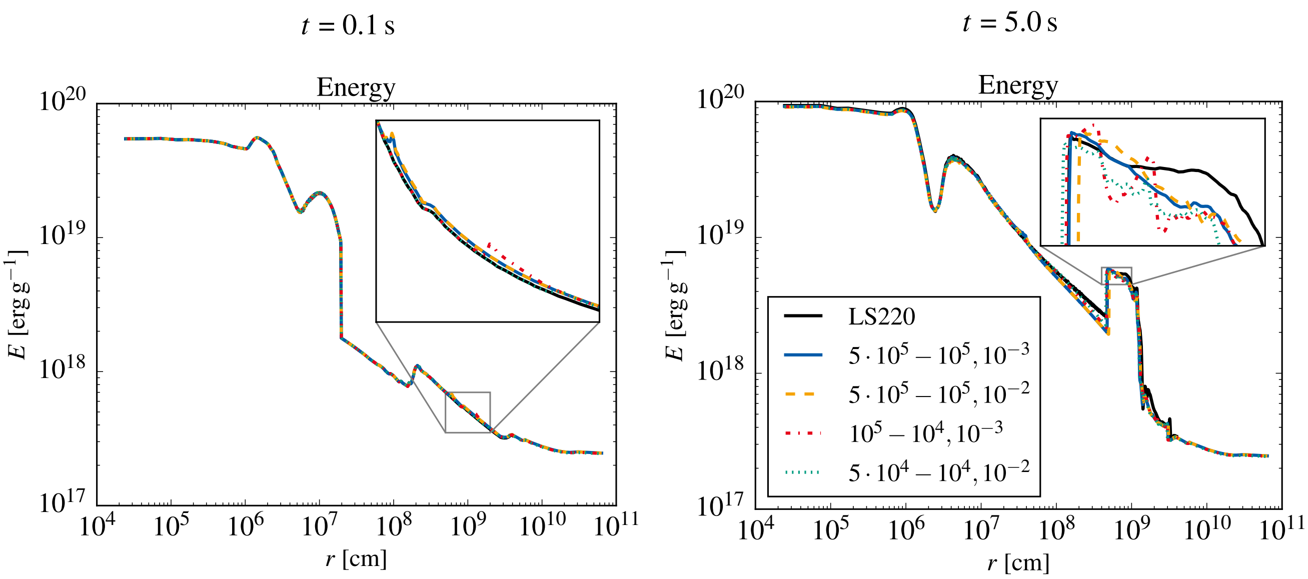

Figure 6.4.: Comparison of various parameter sets at 0.1 s and 5 s after bounce from the simulation setup investigated previously. The parameters can be chosen arbitrarily. Numbers in front of the comma denote the transition densities in g cm^{-3}, the value after the comma indicates the decrease.

Overall, the different parameter sets yield similar results, especially at earlier times. A close look at the internal energy reveals the onset of the transition and how it blends in with the nuclear EOS. For the lowest transition density, $\rho_{\text{transition}} = 5 \cdot 10^4\,\text{g}\,\text{cm}^{-3}$, the starting point is almost not visible. More differences occur for the radial profiles 5 s after bounce. Firstly, all of our parameter sets yield lower internal energies, as a result of the missing offset contribution after the shock passes the transition region. Also, the shock position is not reproduced accurately by all parameter sets, shown in the inset. Additionally, we observe that small oscillations arise in the largest transition region, $10^5\,\text{g}\,\text{cm}^{-3} - 10^4\,\text{g}\,\text{cm}^{-3}$, and also in the lowest transition region. For the same densities, $5 \cdot 10^5\,\text{g}\,\text{cm}^{-3} - 10^5\,\text{g}\,\text{cm}^{-3}$, with varying decrease, 10^{-2} and 10^{-3}, it seems that the smaller decline yields more robust results and further reproduces the shock position more accurately.

Based on this, we recommend a transition region of the order of half a magnitude, with a decrease of around 10^{-3}. However, all of the presented parameter sets yield reasonable results compared to the simulations performed with the nuclear EOS. Altogether, the transition formalism seems robust enough regarding the choice of parameters.

6.3.2 Different progenitors

The constant offset shift is determined using initial conditions from the progenitor. Here, we want to test the transition formalism for a different progenitor, and also point out the importance of the progenitor structure when choosing the transition region. We investigate a $15\,M_\odot$ progenitor [36], choosing the transition region from $5 \cdot 10^5\,\text{g}\,\text{cm}^{-3}$ to $10^5\,\text{g}\,\text{cm}^{-3}$, with a decrease of 10^{-2}. The radial profiles for pressure, internal energy, and entropy are shown in Fig. 6.5, 100 ms after bounce. The transition region is marked by gray vertical lines.

The result are quite similar to the $20\,M_\odot$ progenitor in Fig. 6.2. Pressure and internal energy reach their maximum values in the interior of the hot and dense PNS and further decrease in the outer layers of the star. The shock is visible at around 200 km. Additionally, we observe that the choice of $\rho_{\text{transition}} = 5 \cdot 10^5\,\text{g}\,\text{cm}^{-3}$ as starting point for the transition appears to be an upper limit that is reasonable. A local maximum in the internal energy, from the progenitor structure, at around 4 000 km, corresponding to a density of $5 \cdot 10^5\,\text{g}\,\text{cm}^{-3}$, could yield numerical problems as the decrease function would not be monotonic.

Further, the same differences in entropy as observed in the $20\,M_\odot$ star, linked to the way the average mass number and average proton number are obtained, are visible. Apart from that, the two EOS agree, implying the transition formalism is functional for various progenitors.

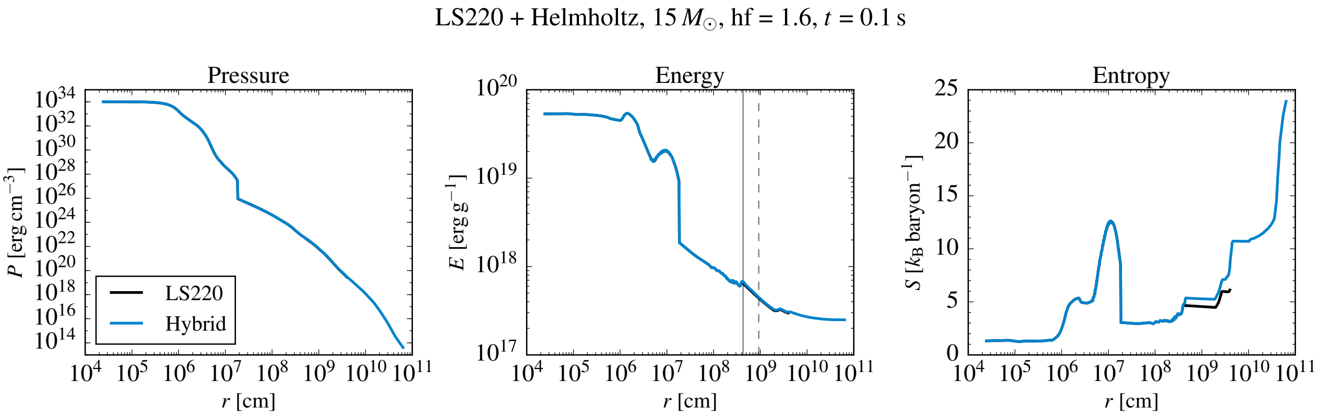

Figure 6.5.: Investigation of the hybrid EOS for a different progenitor.

We analyze our results when the shock has left the transition region in Fig. 6.6. Here, we have to chose 3 s after bounce for comparing the two EOS, since the shock has left the simulation domain for the nuclear EOS table at a later time. The results are similar to the 20 $M_\odot$ progenitor, although for this progenitor, the electron fraction shows no difference at a later time (also when compared to the 20 $M_\odot$ progenitor 3 s after bounce). We find that the internal energy is smaller compared to the nuclear EOS, due to the missing offset contribution that is not added anymore after the shock has left the transition region. Other than that, both EOS agree and yield the same shock position. We note again that the hybrid EOS extends the domain to arbitrary radii, removing the previous limit for the maximum simulation time.

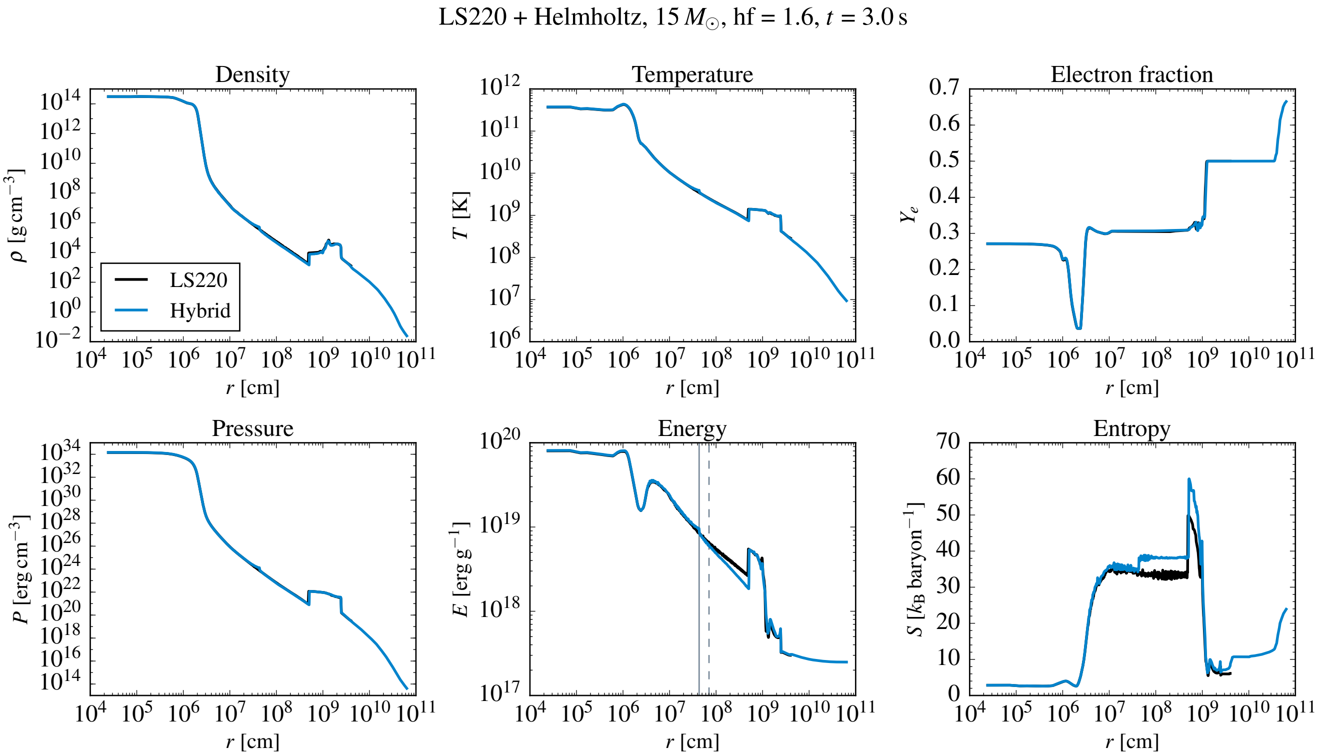

Figure 6.6.: Same as Fig. 6.5, shown 3 s after bounce.

Since the transition formalism allows us to investigate later times, we also present results for the 15 $M_\odot$ progenitor, 5 s after bounce, in Fig. 6.7. The shock has left the smaller simulation domain ($r \sim 40\,000$ km) and further propagates outwards. We note again that the entropy is relatively high, as a consequence of using the progenitor composition. As a next step, one should consider using a network with the transition formalism to have a better estimate of the composition. However, this is a first step towards the goal of making long-time simulations available.

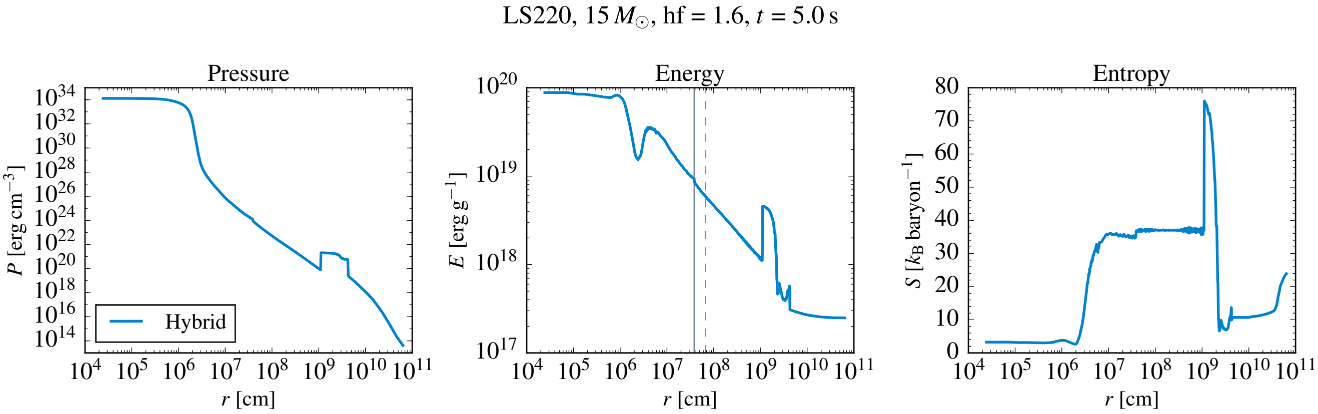

Figure 6.7.: The same simulation as Fig. 6.5 and Fig. 6.6, 5 s after bounce. Note that we do not show the nuclear LS220 EOS table results here, since the shock has left the simulation domain that is available with the table. Therefore the simulation stopped.

6.3.3 Different equations of state

Our next objective is to test different available equation of state. The LS EOS is based on a Skyrme energy density functional and nuclei are described within the compressible liquid-drop model, see Sec. 4.3.1. It assumes matter consisting of electrons, positrons, photons, neutrons, protons, alpha particles, and heavy nuclei [120]. The latter are treated within a single nucleus approximation (SNA), meaning the distribution of nuclei is described by one representative nucleus. However, other EOS models are based on different theories and also may treat nuclei differently. Another commonly used nuclear EOS is the Shen *et al.* EOS (Shen EOS) [136, 156], see also Sec. 4.3.2, which is based on a meson-exchange interaction in a relativistic mean-field approximation. It also uses a SNA and assumes the same particles as in the LS EOS. There are more recently developed EOS models, based on the same formalism as the Shen EOS, which do not use the SNA but employ a chemical composition for the distribution of nuclei (see, e.g., Refs. [121, 162] and Sec. 4.3.3). Note that the LS EOS defines the internal energy relative to the rest masses of the neutron, while others use the atomic mass m_u.

The above mentioned EOS are widely used in CCSN simulations, which means that the transition formalism should work for all these EOS. Since all of the parameters (constant offset shift and the offset function) are tuned to the EOS within the initialization of the simulation, this requires no further modifications.

We present our results using the Shen EOS for the 15 $M_\odot$ progenitor in Fig. 6.8. The transition is done from $5 \cdot 10^5$ g cm^{-3} to 10^5 g cm^{-3}, with a decrease of 10^{-2}. Note that the heating factor is larger compared to the previous ones. The Shen EOS is a "stiffer" EOS, which makes the PNS less compact, and thus results in less energetic shocks. The radial profiles are shown 5 s after bounce, as differences in the two EOS are most pronounced at later times.

The two EOS are in agreement, and the hybrid EOS manages to reproduce all of the relevant characteristics of the nuclear EOS. For the Shen EOS, the electron fraction 5 s after bounce is matched by the hybrid EOS. We see a decrease in the internal energy after the shock has passed the transition region, resulting from the missing offset contribution. Regarding the entropy, the hybrid EOS yields again higher values, although not as distinct as for the LS220 EOS. Apart from the points discussed above, all of the relevant quantities are matched. We conclude that the transition formalism is applicable for the Shen EOS, and no additional modifications need to be considered.

To conclude this chapter, we present simulation results obtained with the SFHo EOS [163] and the 20 $M_\odot$ progenitor in Fig. 6.9. This is one of the EOS that includes a statistical ensemble of nuclei in contrast to the LS and Shen EOS. The transition is done from $5 \cdot 10^5$ g cm^{-3} to 10^5 g cm^{-3}, with a decrease of 10^{-2}. Note again the higher heating factor.

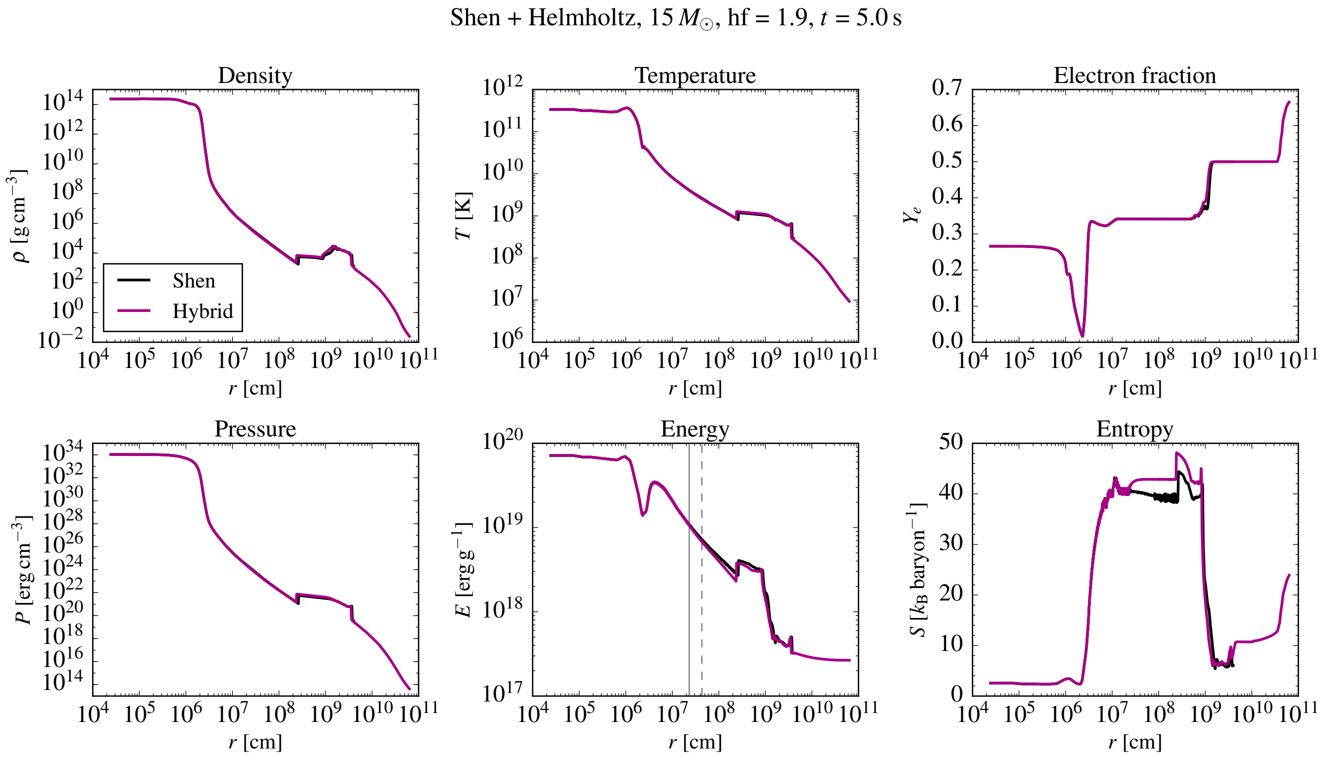

Figure 6.8.: Results for the transition formalism tested with the Shen EOS.

The radial profiles are shown 5 s after bounce. All quantities agree among the two EOS, apart from the differences already discussed for the other cases. In the SFHo EOS, a chemical composition is used instead of a SNA (like in the Shen or LS EOS). However, these differences do not affect the EOS transition.

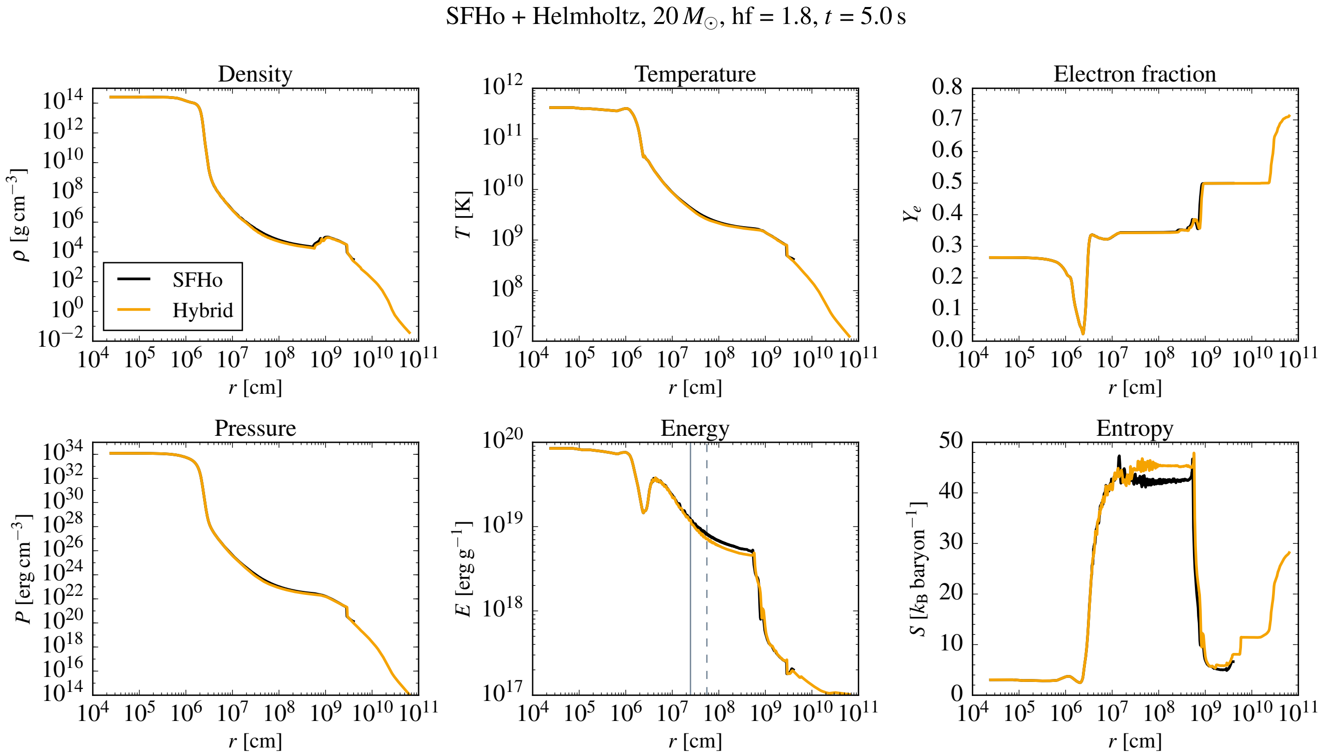

Figure 6.9.: Radial profiles for the SFHo EOS, which uses a different description of nuclei.

The investigated cases show that the implemented transition formalism works well for different EOS, different progenitors, and various parameter sets. We have also tested the hybrid EOS with an M1 transport scheme from Ref. [82], as well as an advanced spectral leakage from Ref. [79]. All of the important characteristics are reproduced when compared to simulations without the transition. With the hybrid EOS, the domain can be extended arbitrarily. As a next step, one should consider including a nuclear reaction network, such that the composition is not taken from the progenitor but estimated more accurately. Computationally speaking, this is more expensive, however, it would be useful for nucleosynthesis calculations. The decrease in the internal energy comes from the fact that the binding energy is not taken into account. If a network is used, the binding energy could be calculated and added. Then, a transition would still be necessary, since the binding energy will not precisely agree with the one from the nuclear EOS, but the margin between the two EOS would be much smaller. This could replace the constant offset shift from the progenitor that was used to minimize the difference. Nonetheless, the presented approach already makes long-time simulations available and is modular, so that further improvements can be easily included.

6.3.4 Two-dimensional simulations

We further investigate the functionality of the hybrid EOS in two-dimensional (2D) simulations with FLASH in cylindrical symmetry. Since 2D simulations are computationally more expensive, we focus on the LS220 EOS with the $15\,M_\odot$ progenitor, using the gray neutrino leakage scheme. The transition is done from $5 \cdot 10^5\,\mathrm{g\,cm^{-3}}$ to $10^5\,\mathrm{g\,cm^{-3}}$, with a decrease of 10^{-2}. Note that we will not be able to compare these results to a simulation obtained with the previously used nuclear EOS table, due to the stochastical nature of multidimensional simulations, even if all initial conditions are identical. This section should therefore be viewed as a proof of concept.

The first snapshot in Fig. 6.10 shows the internal energy 700 ms after bounce, for a heating factor of hf = 1.1. The z-axis is the symmetry axis and the value of the internal energy is color coded. The PNS in the center is visible, where the internal energy reaches its maximum (red), comparable to the 1D results. The cyan-greenish outer layer visualizes the position of the shock, where the internal energy is higher compared to the outer layers (dark blue), which the shock has not reached yet. Within the shock, the turbulent nature of multidimensional effects in CCSN simulations is visible.

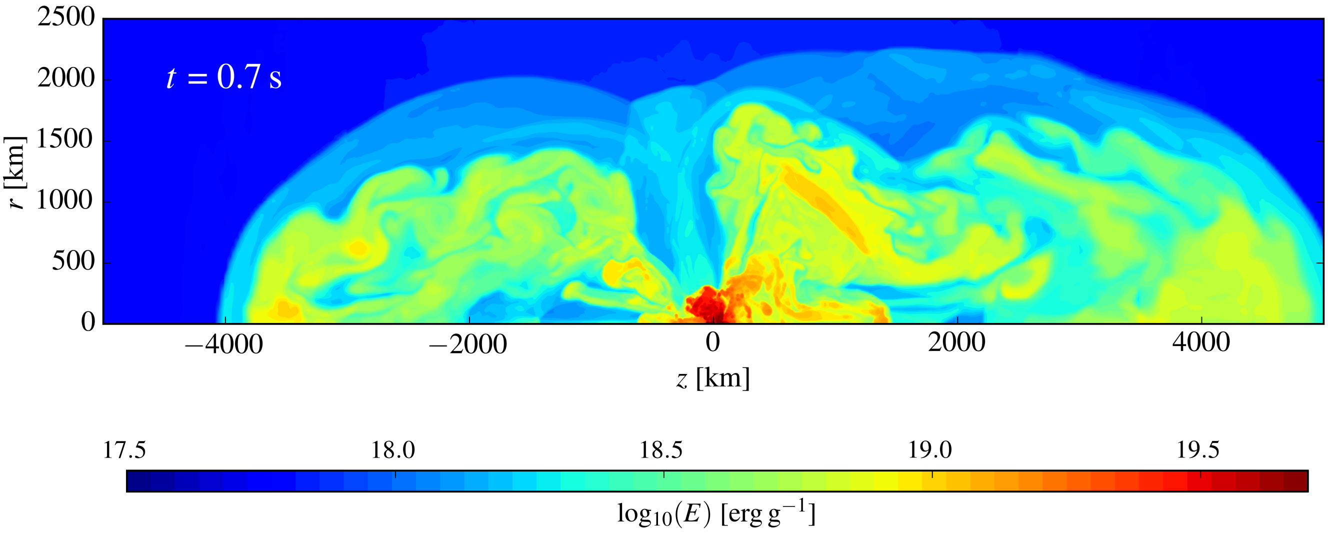

Figure 6.10.: Snapshot of the internal energy from a 2D simulation. The transition formalism is tested with the LS220 EOS, $15\,M_\odot$, and a heating factor of hf = 1.1.

We choose this time as the shock is already passing the transition region. In Fig. 6.11, we plot the same snapshot, but with contours where the density is equal to $5 \cdot 10^5\,\mathrm{g\,cm^{-3}}$. When comparing these two figures, the transition region is not identifiable in Fig. 6.10, implying that the transition between the two EOS is relatively smooth. This agrees with our previous findings. Note that we do not have to make any additions to the transition formalism in order to use it in 2D, as it has no restriction to any dimension in the way that it is implemented.

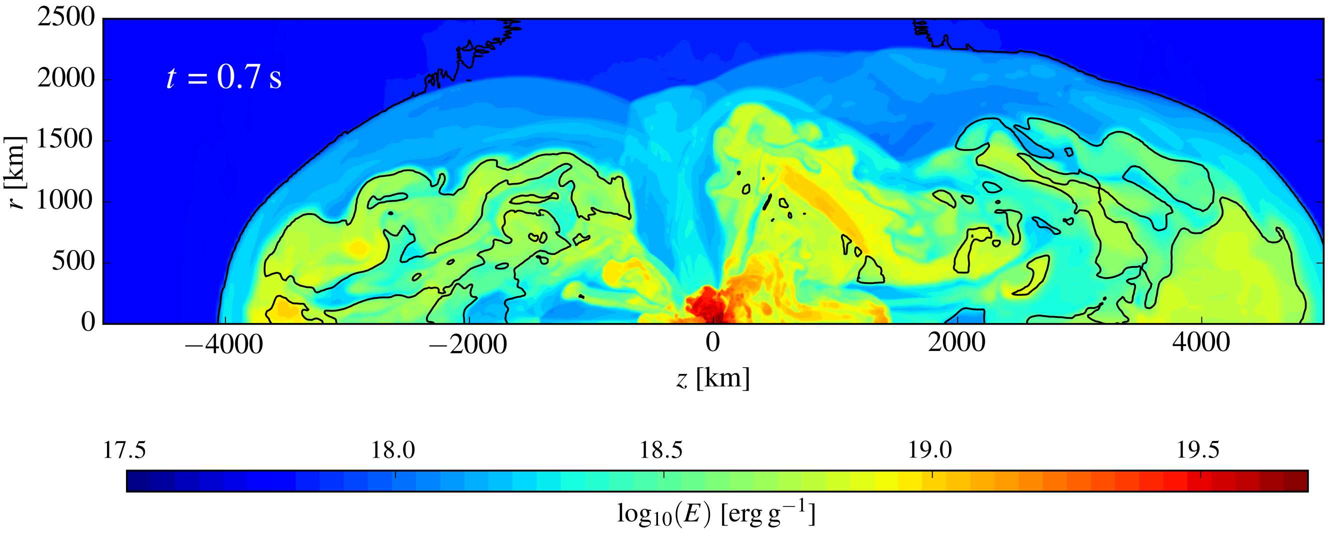

Figure 6.11.: Same as Fig. 6.10, but the density where the transition region starts ($\rho_{\text{transition}} = 5 \cdot 10^5\,\mathrm{g\,cm^{-3}}$) is marked as black contours.

An intermediate time, 2.5 s after bounce, for the same simulation is shown in Fig. 6.12. Note that the plotted domain is larger compared to the figures above. Again, the shock surface is visible as cyan-greenish region and the outer layers, where the shock has not passed yet, are indicated as dark blue. One can see how the shock expansion is not symmetrical but rather favors one direction as discussed, e.g., in Ref. [186]. We additionally plot a contour, where the density is equal to $1 \cdot 10^3\,\mathrm{g\,cm^{-3}}$. This corresponds to the minimum density value in the nuclear EOS table. Once the shock reaches this radius, a simulation with only the nuclear EOS table stops, in this case around 2.5 s after bounce. Further, one can observe that there are additional low density, $\rho < 10^3\,\mathrm{g\,cm^{-3}}$, regions within the shock expansion. With the nuclear EOS, these are set to the lowest available density in the EOS table.

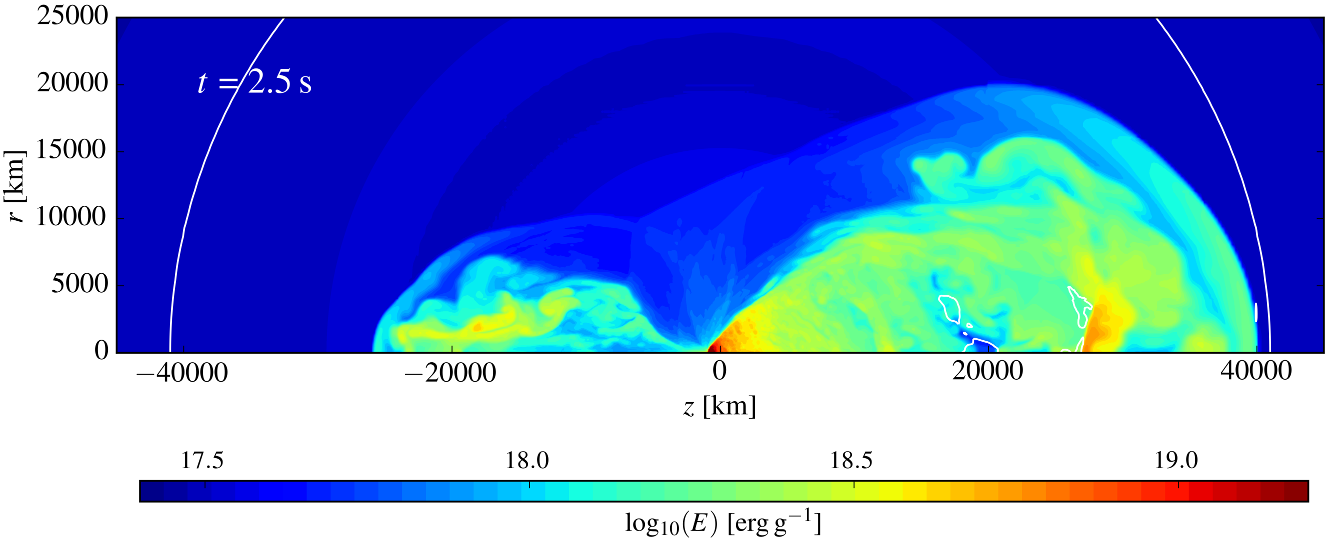

Figure 6.12.: Same simulation, 2.5 s after bounce. The white contour indicates where the density is equal to $10^3\,\mathrm{g\,cm^{-3}}$. This corresponds to the minimum of the nuclear EOS table. As soon as the shock reaches this density, simulations with only the nuclear EOS table stop.

With the hybrid EOS, however, we are able to extend the domain and follow the shock as long as desired. We present the internal energy 5 s after bounce in Fig. 6.13.

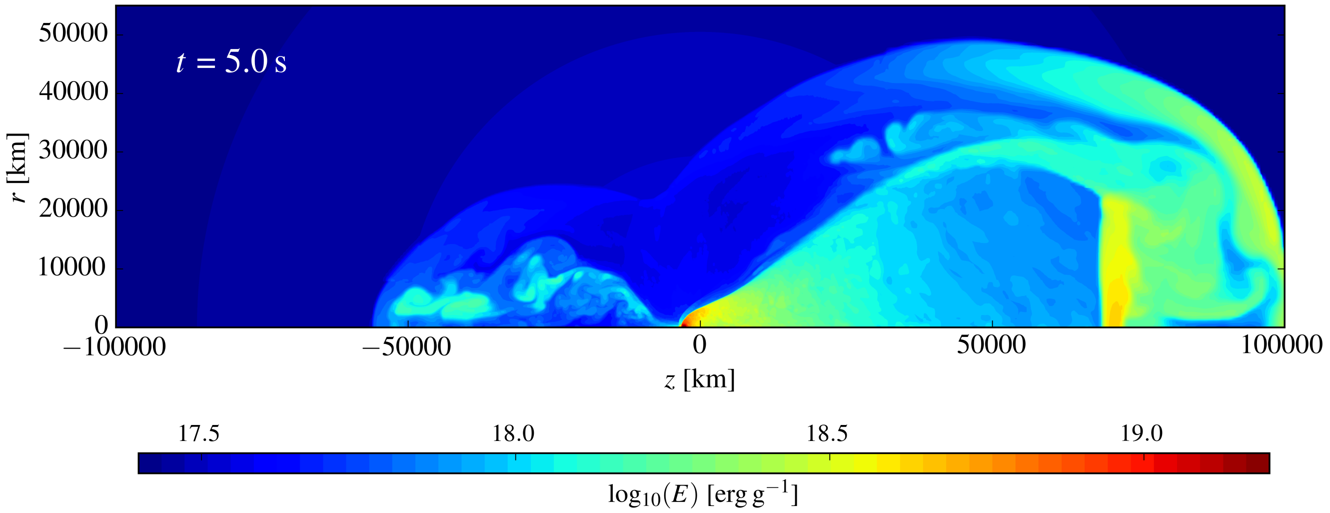

Figure 6.13.: Final snapshot of the simulation, 5 s after bounce.

Note that the domain is larger than in Fig. 6.12. The asymmetrical expansion of the shock is again visible. The region where the transition is applied is not recognizable. One might speculate that the mixing with more neighboring cells in 2D, compared to 1D, makes the transition less susceptible to possible oscillations that can develop [77].

A detailed discussion of long-time CCSN simulations with various heating factors and additional rotational profiles can be found in the next chapter. Here, we solely focus on the validity of the transition formalism. We have also tested the hybrid EOS in a setup with additional rotation. First tests in 3D have yet to be performed. Overall, the transition formalism works for different EOS and progenitors, various heating factors and neutrinos schemes, and spherical as well as 2D simulations. All technical simulation details can be found in Appendix A.

7 Long-time Simulation of Core-Collapse Supernovae

Long-time simulations of core-collapse supernovae (CCSN) are essential to understanding the conditions that are relevant for nucleosynthesis. We investigate different CCSN scenarios varying the rotational profile and the explosion energetics by enhancing the neutrino energy deposition. The simulations are performed in cylindrical symmetry and we follow the shock evolution up to five seconds after bounce. This requires a large simulation domain and allows us to verify the validity of our implemented hybrid equation of state, see Chapter 6. Our intent is to perform a systematic parameter study, we therefore chose to explore two-dimensional simulations with a simplified neutrino leakage scheme. Future work includes nucleosynthesis calculations using tracer particles.

Calculations for this research were conducted on the Lichtenberg high performance computer of the TU Darmstadt. The results presented here are preliminary, we solely aim to provide a first summary. A detailed analysis is still ongoing.

7.1 Simulation setup

The simulations are performed in cylindrical symmetry with the FLASH code [77, 161], a $15\,M_\odot$ progenitor from Ref. [36] without initial rotation, and a gray neutrino leakage [117] with a deleptonization scheme pre-collapse [92]. We employ the Lattimer & Swesty equation of state [120, 124] with an incompressibility of $K = 220$ MeV. The domain is extended using the hybrid extension, see Chapter 6, with a transition from $5 \cdot 10^5$ g cm^{-3} to $1 \cdot 10^5$ g cm^{-3}, and a decrease of $1 \cdot 10^{-2}$. The simulations are evolved up to 5 s after bounce. Further technical simulation details can be found in Appendix A.

We run a total of 24 simulations. The energy deposition by neutrinos in the gain layer is enhanced by means of a heating factor (hf), see Sec. 3.4.2, which we vary from 1.0 to 1.5. On top, we investigate 7 different rotational profiles, including non-rotating cases. An overview of the models that are investigated is shown in Tab. 7.1. Out of the 24 simulations, 13 do not result in a successful explosion after a simulation time of 1 s, and are not continued longer. They are marked as (x).

An artificial heating factor of at least hf = 1.05 is necessary to obtain a successful explosion. The additional rotational profile for the case with a heating factor of hf = 1.1 seems to be less favorable for an explosion. Neutrino-driven winds form in 5 of our models and appear to be supported by additional rotation, see hf = 1.3. In the following, we investigate 9 different cases in detail, including 5 different heating factors and 5 different rotational profiles. They are marked in blue in Tab. 7.1.

Ω_0 [2π rad s^{-1}]	0.00	0.01	0.03	0.06	0.10	0.20	0.30
hf							
1.00	(x)	(x)	(x)	(x)	(x)	(x)	(x)
1.05	✓						
1.10	✓	(x)	(x)	(x)	(x)	(x)	(x)
1.20	✓						
1.30	✓	**W**	✓	✓	**W**	**W**	W
1.50	**W**						

Table 7.1.: Overview of our simulation configurations. Cases marked with (x) do not explode after 1 s and are not continued. Simulations marked with a checkmark explode. Further, "W" denotes the presence of a neutrino-driven wind in the simulation. We investigate the cases that are colored in blue.

In view of these findings, it is necessary to perform additional simulations with a heating factor of hf = 1.2 and rotation to find clear correlations regarding the impact of rotation.

We impose an additional rotational profile via:

$$\Omega(r) = \Omega_0 \cdot \frac{1}{1+(r/r_A)^2}, \tag{7.1}$$

where Ω_0 represents the rotational velocity in the origin of the star, r denotes the distance from the center of the rotational axis, and r_A is a free parameter. We investigate different values for Ω_0, see Tab. 7.1, and chose $r_A = 3 \cdot 10^8$ cm, which is approximately the size of the iron core in the progenitor. A value of $\Omega_0 = 0.03 \cdot 2\pi\,\mathrm{rad\,s^{-1}}$ in a $15\,M_\odot$ progenitor corresponds to a rotational velocity that emerges from stellar evolution calculations including magnetic fields [187], which we refer to as "moderate" rotation in the following. Rotational velocities with $\Omega_0 \sim 0.1 \cdot 2\pi\,\mathrm{rad\,s^{-1}}$ and higher can be seen as a rapid rotation (see, e.g., Refs. [188, 189]), although not commonly found in stellar evolution [187].

The impact of rotation has been investigated in 2D simulations (see, e.g., Refs. [189–198]), and 3D simulations (see, e.g., Refs. [188, 189, 199]), with various neutrino treatments. Recent 2D simulations suggest that the effect of rotation on the explosion mechanism depends on magnetic fields (see, e.g., Ref. [198]), but also on the strength of the standing accretion shock instability, and convection (see, e.g., Ref. [197]), which is also related to the mass of the progenitor star. We employ a $15\,M_\odot$ progenitor without magnetic fields similar to Ref. [189], which investigates the impact of rotation in 2D and 3D. In their 2D simulations, Summa *et al.* [189] find that moderate rotation supports the shock revival by neutrinos, however, the rapidly rotating model fails to explode. They note that the centrifugal forces in the rapidly rotating model stabilize the accretion shock and increase the advection time scale, but simultaneously the neutrino luminosity is reduced due to the rapid rotation that prevents accretion, resulting in a failed explosion.

All of the above mentioned simulations that have been performed in recent years are evolved up to approximately 600 ms after bounce and the impact of rotation on the long-time behavior of CCSN has not been studied thoroughly yet. We follow the simulations up to 5 s after bounce, and additionally explore different artificial heating factors in combination with rotation. Further, we plan to use tracer particles to perform nucleosynthesis calculations for our long-time simulations. An example for such an approach can be found in, e.g., Refs. [200–202].

7.2 Explosion properties

We present the average (av) and maximum (max) shock radius as a function of time, 1 s and 5 s after bounce, for our 9 different cases in Fig. 7.1. The time $t = 0$ s refers to the time of bounce.

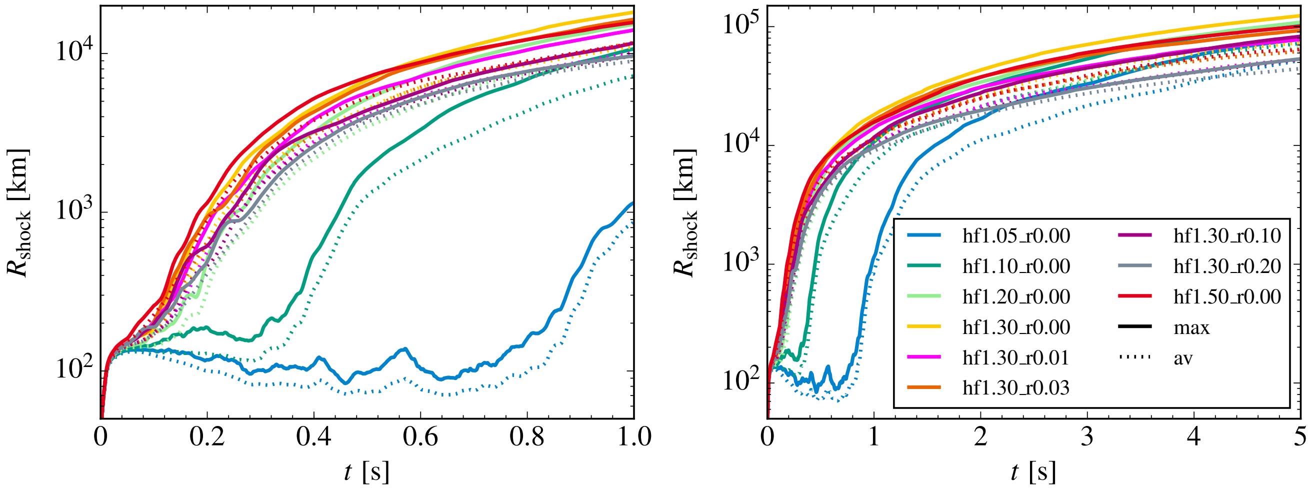

Figure 7.1.: Average (av) and maximum (max) shock radius as a function of time for the 9 different simulation cases.

The simulation with the highest heating factor, hf = 1.5, explodes earliest ($t_{\mathrm{expl}} \sim 120$ ms), where we define the explosion time as the time where the shock reaches 500 km. This is followed by the hierarchy of heating factors, and the model with the lowest heating, hf = 1.05, explodes comparably late ($t_{\mathrm{expl}} \sim 900\,\mathrm{ms}$). For heating factors hf $\geq$ 1.2, we obtain early explosions in the first 200 ms after bounce. Within the same heating factor, hf = 1.3, but exploring different rotational profiles, the shock evolution is hardly affected by moderate rotation, i.e., $\Omega_0 = 0.01, 0.03$, and $0.1 \cdot 2\pi\,\mathrm{rad\,s^{-1}}$. The rapidly rotating case, $\Omega_0 = 0.2 \cdot 2\pi\,\mathrm{rad\,s^{-1}}$, exhibits a slightly later explosion time compared to the non-rotating model ($t_{\mathrm{expl}} \sim 40\,\mathrm{ms}$ later).

We calculate the diagnostic energy via:

$$E_{\mathrm{diag}} = \sum_{E_{\mathrm{tot}}>0} E_{\mathrm{tot}}\,, \qquad \text{where} \qquad E_{\mathrm{tot}} = E_{\mathrm{int}} + E_{\mathrm{kin}} + E_{\mathrm{grav}}\,, \tag{7.2}$$

where E_{int} denotes the internal energy that we compute from the Helmholtz EOS, see Sec. 4.5, and E_{kin} and E_{grav} represent the kinetic and gravitational binding energy, respectively. Positive values for E_{tot} correspond to matter expanding away from the proto-neutron star (PNS). Note that the internal energy from the Helmholtz EOS does not include a binding energy of nuclei.

The diagnostic energy for the 9 different cases is shown in Fig. 7.2. We find that the larger the heating factor, the higher the diagnostic energy. Additional rotation reduces the diagnostic energy, where the simulation with the strongest rotation, $\Omega_0 = 0.2 \cdot 2\pi\,\mathrm{rad\,s^{-1}}$, results in the smallest value after 5 s. This strong rotation case also develops a neutrino-driven wind with a duration of $t_{\mathrm{wind}} \sim 3.6\,\mathrm{s}$. We present the cases where a neutrino-driven wind develops in Tab. 7.2. The wind duration t_{wind} is defined as the time where the total mass accretion rate at $r = 500\,\mathrm{km}$ is equal to zero, i.e., $\dot{M}_{\mathrm{acc}} = 0$. Models with a neutrino-driven wind that is longer than $t \sim 1\,\mathrm{s}$ exhibit a smaller diagnostic energy, cases hf1.30_r0.01, hf1.30_r0.20, and hf1.50_r0.00, as these models have a smaller mass accretion rate. However, none of our models show a complete saturation of the diagnostic energy within the first 5 s.

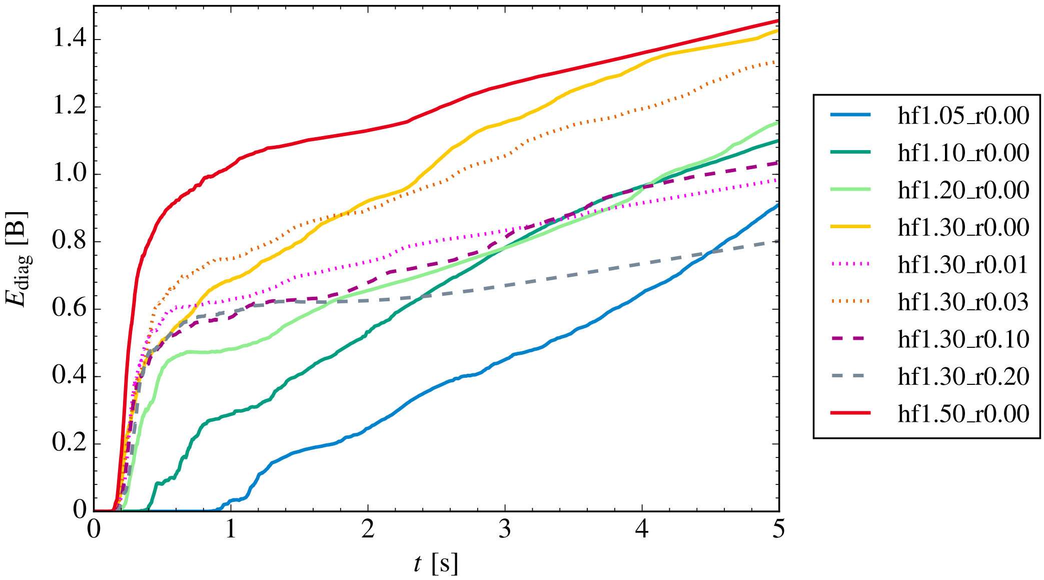

Figure 7.2.: Diagnostic energy for our various models, where $1\ \mathrm{B} = 1 \cdot 10^{51}$ erg.

	hf1.30_r0.01	hf1.30_r0.10	hf1.30_r0.20	hf1.50_r0.00
t_{wind} [s]	0.820	0.668	3.601	1.829
t_{start} [s]	4.185	4.435	1.481	3.278

Table 7.2.: Neutrino-driven wind starting time t_{start} and duration t_{wind} until the end of the simulation.

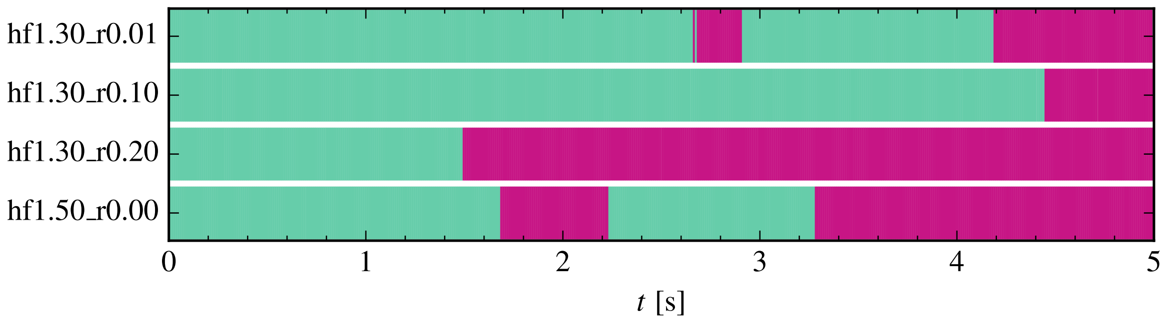

Figure 7.3.: Visualization of neutrino-driven wind appearances (red) in our simulations. For two models, hf1.30_r0.01 and hf1.50_r0.00, additional neutrino-driven winds occur that are not stable.

To determine why the diagnostic energy does not saturate, we investigate the mass accretion in the left panel of Fig. 7.4. The three simulations with the lowest heating factors, hf = 1.05, 1.1, and 1.2, exhibit the largest mass accretion rates for the whole simulation time. The model with a heating factor of hf = 1.1 even shows a slight increase of the accretion rate after $t \sim 3\,\mathrm{s}$. The accretion rate for the simulation with the highest heating factor declines fastest, which is a result of the early shock expansion, where a significant amount of matter is pushed outwards in the beginning of the simulation. We find that additional rotation reduces the amount of matter that is accreted onto the PNS. The simulation where a steady neutrino-driven wind develops, $\Omega_0 = 0.2 \cdot 2\pi\,\mathrm{rad\,s^{-1}}$, has a vanishing mass accretion rate as soon as the wind forms.

We present the evolution of the PNS mass in the right panel of Fig. 7.4. The masses decrease with increasing heating factor and approximately saturate after $t \sim 1 - 2\,\mathrm{s}$. This is correlated with the mass accretion rate and the energetics of the shock, which pushes a significant amount of matter away from the PNS. The additional rotation results in a slightly lower PNS mass. The simulation with a heating factor of hf = 1.1 shows no saturation for the PNS mass, which can be attributed to the increased mass accretion.

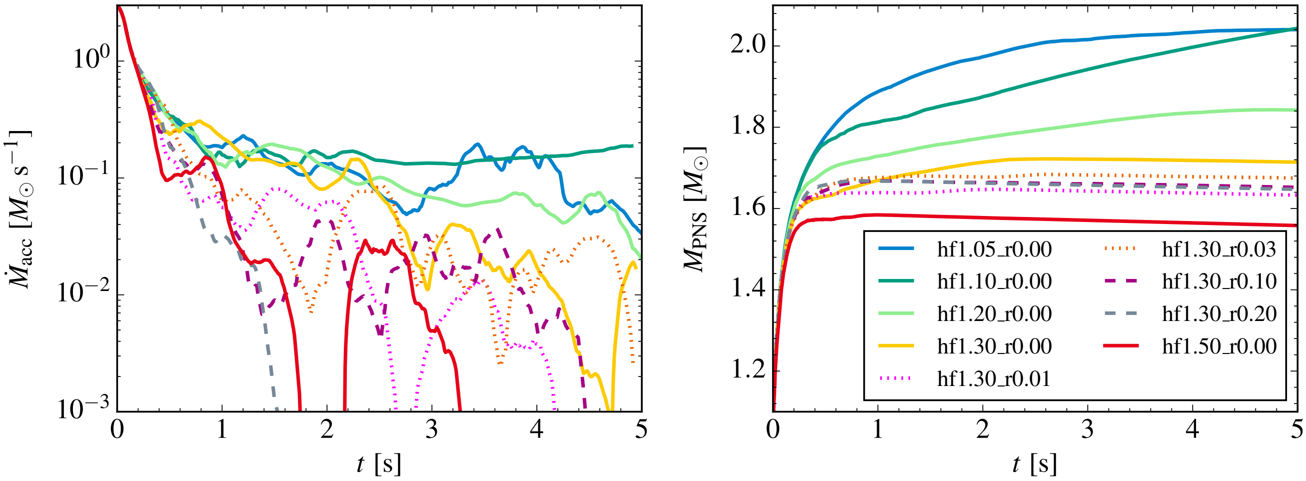

Figure 7.4.: Mass accretion rate at 500 km (left) and PNS mass (right) as a function of time.

To investigate the impact of rotation on neutrino properties, we show the electron antineutrino energy luminosities in three different angular directions for the first second in Fig. 7.5. We focus on the cases with a heating factor of hf = 1.3 and chose antineutrinos, as the effect is more pronounced. At the poles, which correspond to the rotational axis, the luminosities are reduced for rotational cases, as also discussed in Ref. [189]. This is a result of the additional rotation. Matter that is accreted at the poles is moved away from the rotational axis, which slightly increases the luminosities of the rotating cases in the equatorial plane. We do not observe any correlation among the neutrino energies.

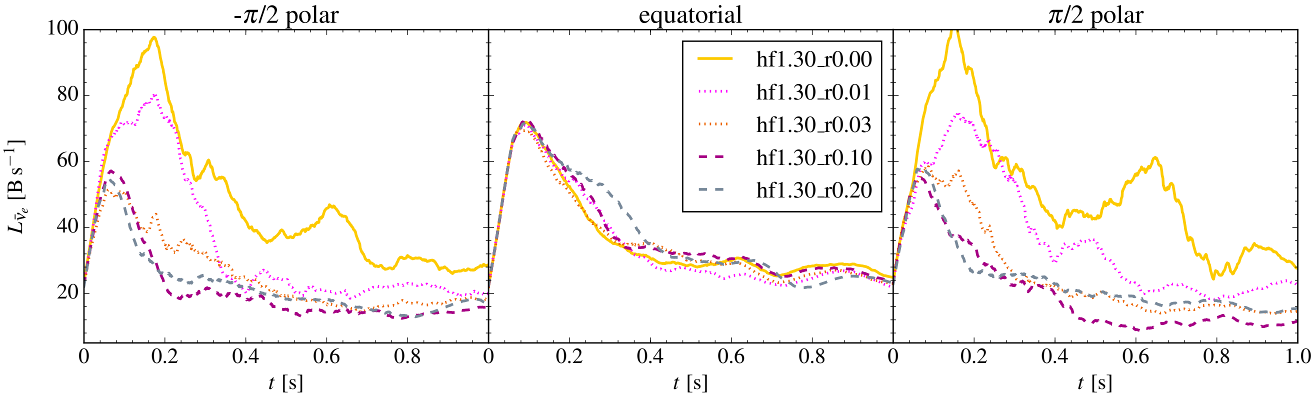

Figure 7.5.: Electron antineutrino energy luminosity as a function of time at three different angles.

An illustration of this "re-distribution" of matter due to rotation is shown in Fig. 7.6. We calculate the percentage of the mass difference 0.2 s after bounce for the simulation domain with the highest rotation, $\Omega_0 = 0.2 \cdot 2\pi \,\mathrm{rad\,s^{-1}}$, and the case without rotation, and normalize it to the non-rotating case. Negative values (blue) correspond to less mass in the rotating case compared to the non-rotating one, and vice versa for positive values (red). Note that the z-axis is the rotational axis. For the rotating case, more matter is moved to the equatorial plane than in the non-rotating case and is simultaneously reduced at the poles, which agrees with the neutrino luminosities in Fig. 7.5. Further, the shock surfaces for the two models are visible.

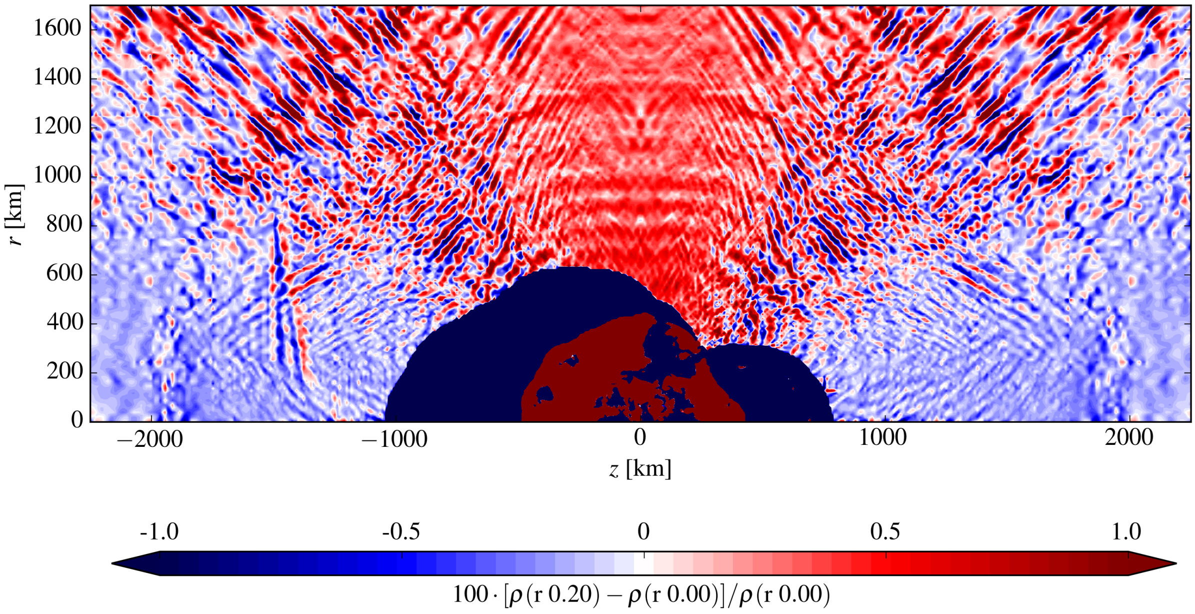

Figure 7.6.: Relative mass difference for the rapidly rotating model, $\Omega_0 = 0.2 \cdot 2\pi \,\mathrm{rad\,s^{-1}}$, compared to the non-rotating one 0.2 s after bounce.

Figure 7.7 shows the integrated energy luminosities for electron neutrinos and electron antineutrinos for the long-time evolution with a heating factor of hf = 1.3. We find smaller neutrino luminosities for simulations that include rotation, as observed in Ref. [189]. This is correlated with the accretion rates discussed in Fig. 7.4, since a larger mass accretion rate results in higher neutrino luminosities [32]. The neutrino luminosity for the rapidly rotating model, $\Omega_0 = 0.2 \cdot 2\pi \,\mathrm{rad\,s^{-1}}$, which has a vanishing accretion rate as a result of its steady neutrino-driven wind, exhibits a smaller luminosity after $t \sim 2\,\mathrm{s}$. For electron antineutrinos, we observe a slightly enhanced luminosity for the non-rotating case and a higher peak within the first 20 ms, as already seen in Fig. 7.5.

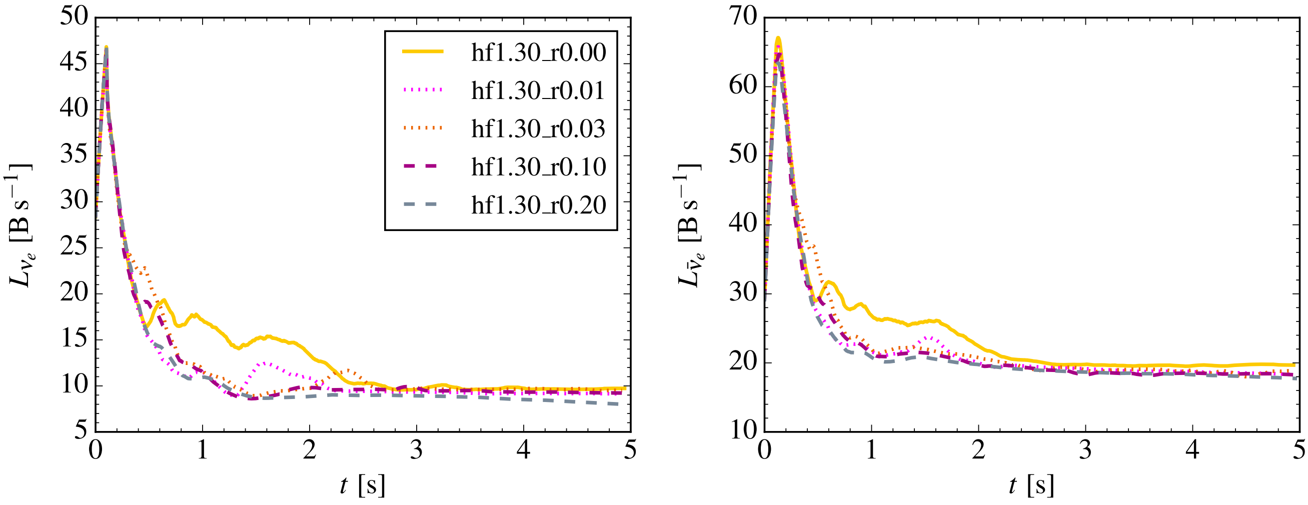

Figure 7.7.: Evolution of the energy luminosity for electron neutrinos (left) and electron antineutrinos (right).

7.3 Shock morphology

The additional rotation influences the shock morphology. Following Ref. [186], we calculate a shock deformation parameter d_{shock}:

$$d_{\text{shock}} = \frac{\max[R_s(\theta)\cos\theta - \min(R_s(\theta)\cos\theta)]}{2\cdot\max(R_s(\theta)\cos\theta)} - 1\,, \tag{7.3}$$

where $R_s(\theta)$ denotes the shock radius as a function of angle θ. A value of 0 corresponds to a spherical shock expansion. Positive numbers correspond to a prolate deformation, negative to oblate. We present our calculation of the deformation parameter in Fig. 7.8.

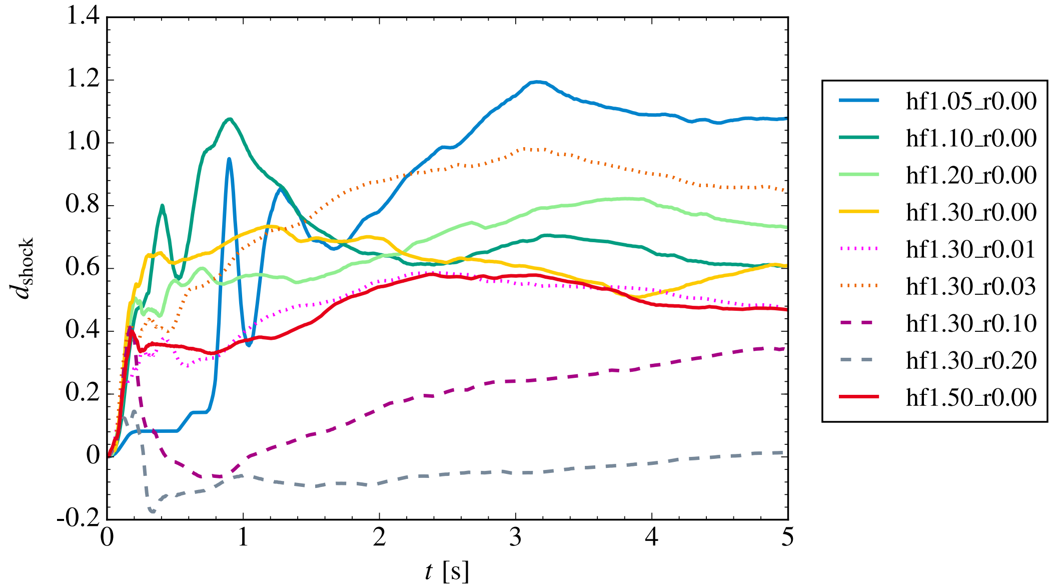

Figure 7.8.: Shock deformation parameter as a function of time. A value of 0 corresponds to a spherical surface.

The simulations without additional rotation consistently exhibit a prolate deformation, which is found to be a consequence of the cylindrical symmetry in simulations (see, e.g., Ref. [195]). Moderate rotation or different heating factors show no impact in the shock morphology. For more rapidly rotating models, $\Omega_0 = 0.1$ and $0.2 \cdot 2\pi\,\mathrm{rad\,s^{-1}}$, the shock expansion is almost spherical. We illustrate the shock morphology by comparing snapshots of the specific internal energy for cases with and without rotation in Fig. 7.9 (hf = 1.3, no rotation) and Fig. 7.10 (hf = 1.3, rapid rotation, $\Omega_0 = 0.2 \cdot 2\pi\,\mathrm{rad\,s^{-1}}$). The model without rotation, Fig. 7.9, shows a strong shock expansion to one pole. In Fig. 7.10, we observe an almost spherical shock surface with a neutrino-driven wind in the center.

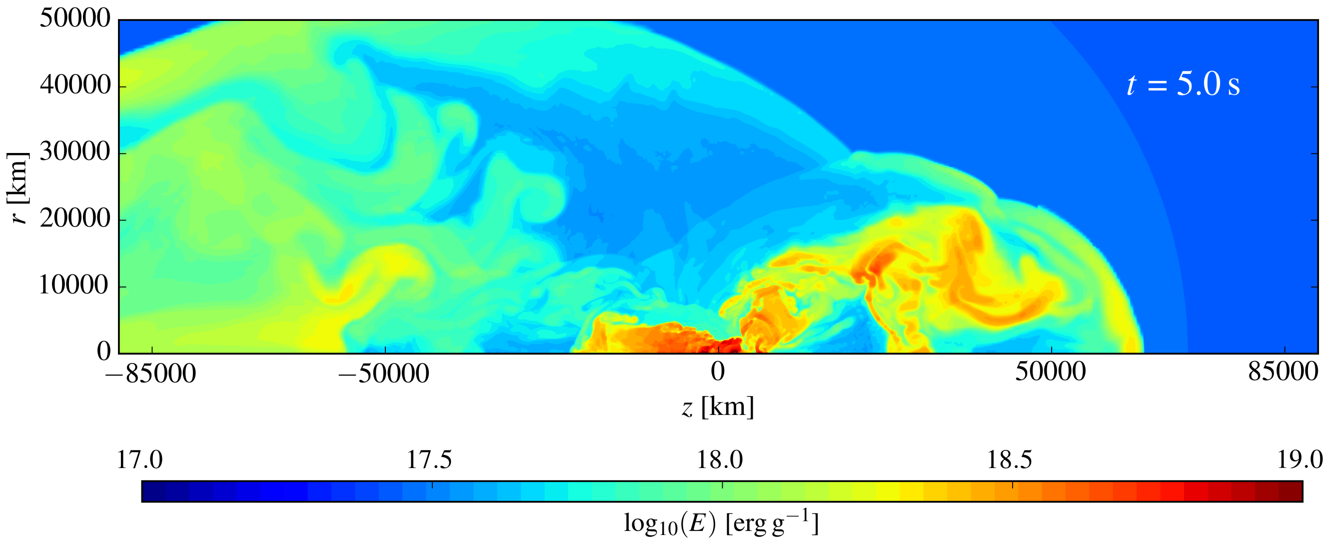

Figure 7.9.: Specific internal energy for the model hf1.30_r0.00 at the end of the simulation.

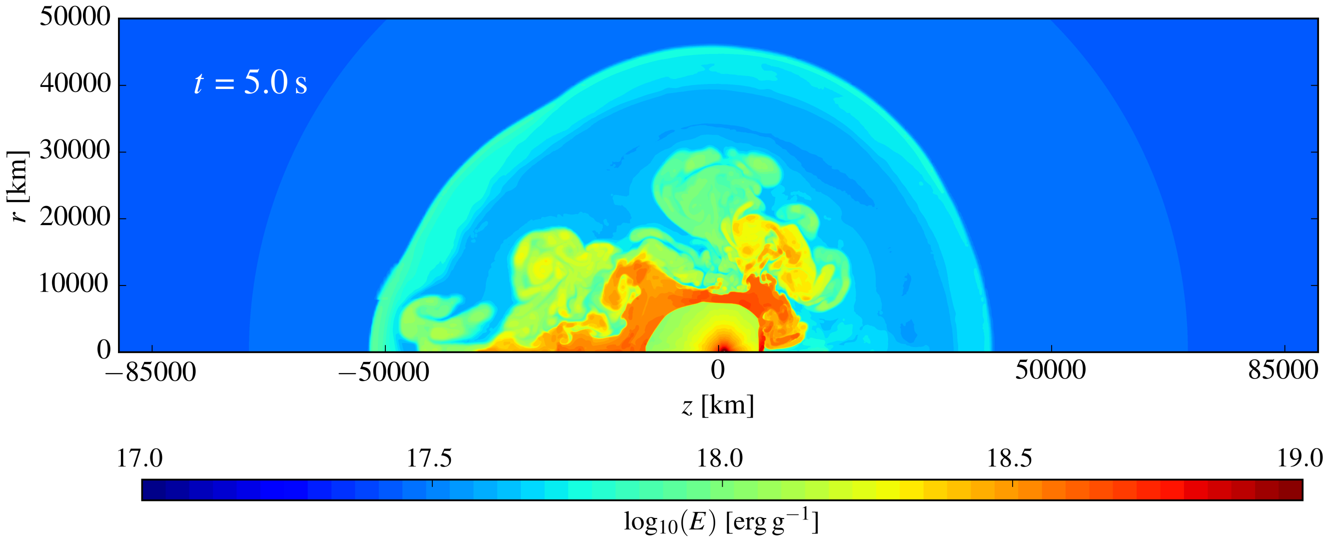

Figure 7.10.: Same as Fig. 7.9, but for the model hf1.30_r0.20 with a neutrino-driven wind. Note that the domain is the same.

7.4 Comparison with M1

The gray neutrino leakage scheme is a simplified treatment that does not evolve the neutrino distribution function, see also Sec. 3.4.2. As a result, the electron fraction evolution, and consequently the entropy, yield inaccurate results. This needs to be considered for nucleosynthesis calculations. To estimate the differences in the electron fraction, we run additional, two-dimensional simulations with the M1 neutrino transport scheme from Ref. [82] for the same progenitor and resolution with various heating factors. We compare the diagnostic energy to find two comparable simulations in Fig. 7.11.

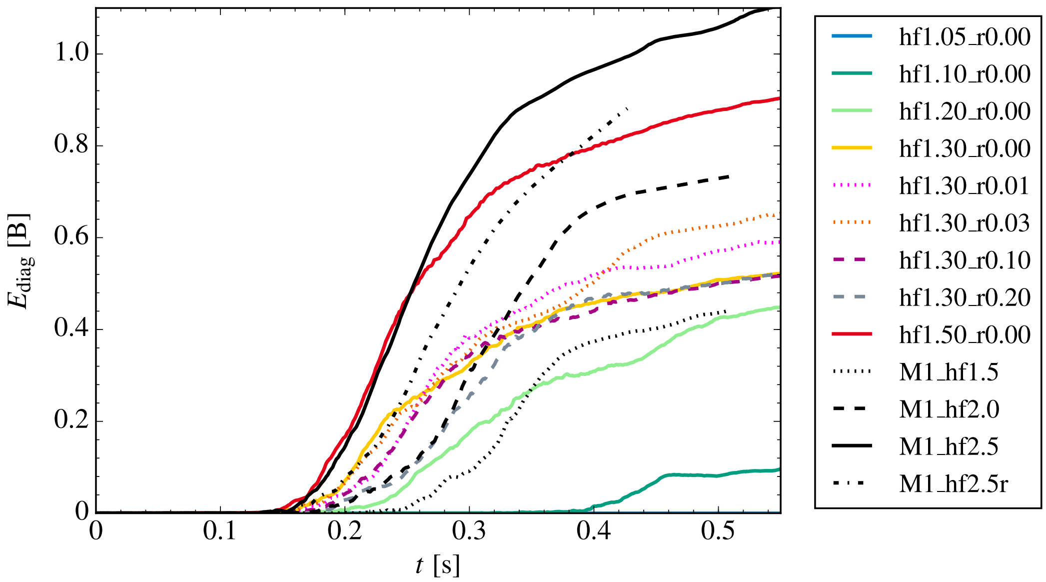

Figure 7.11.: Diagnostic energy with additional simulations performed with the M1 neutrino transport scheme.

As simulations with a more sophisticated neutrino treatment are computationally more expensive, we can only compare the first 500 ms after bounce at this point. Within these results, we chose to discuss the leakage simulation with a heating factor of hf = 1.2 and the M1 simulation with a heating factor of hf = 1.5.

We present spherically averaged profiles for entropy S, electron fraction Y_e, radial velocity v_r, and specific neutrino energy deposition rate $\dot{Q}_\nu$, as a function of radius and time for the simulation performed with the neutrino leakage on the left hand side in Fig. 7.12. The PNS radius is contoured as a solid line where the density is equal to $\rho \sim 10^{11}\,\mathrm{g\,cm^{-3}}$, and the average shock radius is marked with a dashed line in the two upper panels. Inside the shock, between the PNS radius and the shock surface, the entropy increases with time due to the heating by neutrinos. The electron fraction is minimal at the neutrinosphere, close to the surface of the PNS, and approaches $Y_e \sim 0.5$ towards the shock surface. The accretion of matter is visible in the velocity profiles, where blue colors mark matter that is accreted onto the PNS, and red colors represent positive velocities, where matter moves outwards. The energy deposition by neutrinos is shown in the last row. Blue colors indicate where neutrino cooling dominates, close to the surface of the PNS. Red colors show where the energy deposition by neutrinos is larger than the neutrino cooling, illustrating where neutrinos deposit energy behind the shock. The white contour between these to regions corresponds to the gain radius, where neutrino heating is equal to neutrino cooling.

We present the analogous spherically averaged profiles for the simulation performed with the M1 neutrino transport scheme on the right hand side in Fig. 7.12. While the radial velocity and the energy deposition look similar compared to the results obtained with the leakage, entropy and electron fraction show differences. For the simulation obtained with the leakage scheme, values for Y_e inside the PNS, close to its surface, are $Y_e \lesssim 0.1$, while values obtained with M1 are $Y_e \sim 0.15$. Also inside the shock, matter is more neutron-rich in the case of the leakage compared to M1. This also impacts the entropy.

These differences have important implications for nucleosynthesis calculations, which depend on the electron fraction and entropy (see, e.g., Refs. [45, 203]). The comparison with M1 enables us to estimate uncertainties of the electron fraction, which can be used in the nucleosynthesis calculations. While global properties in the simulation, e.g., the shock revival and propagation, can be captured with a neutrino leakage, this does not hold for the evolution of the electron fraction and thermodynamic properties associated with it.

We note again that all of the discussed results are preliminary and solely aim to provide a first overview, a careful analysis is still ongoing.

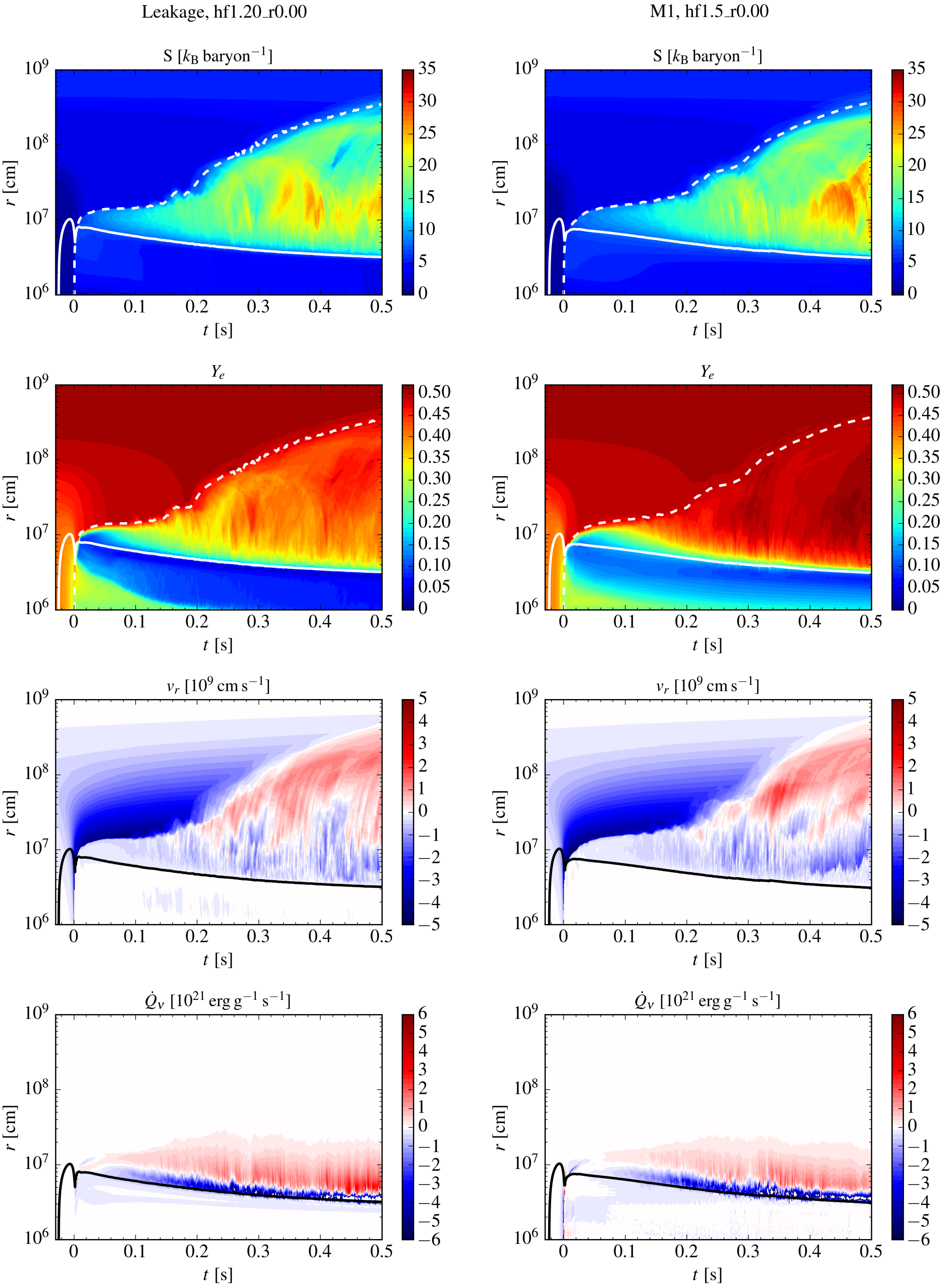

Figure 7.12.: From top to bottom: Color coded entropy, electron fraction, radial velocity, and neutrino energy deposition as a function of spherically averaged radius and time. The left hand side shows profiles for a simulation performed with a neutrino leakage, the right hand side performed with the M1 neutrino transport scheme.

8 Summary and Outlook

Numerical simulations of core-collapse supernovae (CCSN) are essential to explore physics at the extremes and understanding the conditions that are relevant for nucleosynthesis. The equation of state (EOS) is a key ingredient in simulations, which determines the contraction behavior of the proto-neutron star (PNS), and thus impacts neutrino energies and the explosion dynamics. However, the EOS for hot and dense matter is still not fully understood and uncertainties in EOS models strongly affect the outcome of the simulation. The goal of this thesis was to investigate the impact of uncertainties in the EOS on CCSN simulations, and further extend the nuclear EOS to arbitrarily small densities and temperatures. This enabled us to perform long-time CCSN simulations, following the shock behavior up to several seconds after bounce.

In the first part of this thesis, we presented the first systematic study on the impact of uncertainties of nuclear matter properties in the EOS in CCSN simulations [176]. We computed different EOS tables, where we systematically varied the effective mass, incompressibility, symmetry energy, and nuclear saturation point from the Lattimer & Swesty (LS) EOS [120] to the Shen *et al.* EOS [157]. Both are widely used in CCSN simulations, however, they differ in their underlying theory and nuclear physics input, which affects the outcome of the simulation. The generated EOS tables enabled us to trace the effect of varying the nuclear matter properties in CCSN simulations that were performed with the FLASH code [77, 161], using a 15 $M_\odot$ progenitor [36] and an M1 neutrino transport scheme [74, 82]. We found that the contraction behavior of the PNS is mainly governed by the effective mass. This is a result of changes in the pressure, due to the effective mass, which affect the density. Larger effective masses lead to lower pressures at nuclear densities and a lower thermal index, which implies a more rapid contraction of the PNS. When we changed the value of the effective mass in the LS EOS to the value of the Shen EOS, the PNS radii agreed after approximately $t \sim 400\,\mathrm{ms}$. However, this simulation still results in a successful explosion in contrast to the simulation performed with the Shen EOS.

We further varied the incompressibility, symmetry energy, and nuclear saturation point from the values of the LS EOS to the Shen EOS. These changes lead to marginal modifications of the PNS contraction compared to the effective mass. The EOS models with a larger incompressibility and symmetry energy still result in successful explosions. The model where we changed all nuclear matter properties, including the saturation point, to the values in the Shen EOS fails to explode, which agrees with the simulation performed with the original Shen EOS. The different explosion dynamics can be traced to changes in the PNS interior that occur due to the varied nuclear matter properties. We found higher central pressures for smaller effective masses. The incompressibility determines the slope of the pressure, resulting in stiffer EOS for larger incompressibility and symmetry energy. The model that is as similar as possible to the original Shen EOS yields the highest pressure, as a result of the smaller saturation density, and agrees with the Shen EOS. Increasing the pressure reduces the central density in all our EOS models, influencing the PNS contraction. Our results showed that entropy, temperature, and electron fraction in the PNS interior are affected by changes in the nuclear matter properties as well. The electron fraction and entropy in the PNS interior slightly increase with a higher value for the symmetry energy [179, 180], and are approximately constant after bounce. The behavior of the central temperature follows Fermi liquid theory scaling, $S \sim m^* T/\rho^{2/3}$ [182], implying that the temperature increases with smaller effective masses. Further enlarging the symmetry energy results in higher temperatures, due to the larger entropy, while increasing the incompressibility yields lower temperatures, as a result of the smaller density.

Moreover, we calculated the thermal index for our EOS models from the respective simulation. We compared the results to the thermal index of an ideal gas of non-relativistic fermions with a density-dependent effective mass, and found excellent agreement. At the mean-field level in uniform matter, thermal nucleonic contributions to the EOS are completely determined by the effective mass. Larger effective masses lead to a lower thermal index and therefore lower thermal pressures. Finally, we verified that our variations in the EOS give reasonable modifications to the mass-radius (MR) relation of cold neutron stars. Decreasing the effective mass, as well as enlarging the incompressibility, increases the maximum mass of cold neutron stars, as a result of changes in the pressure. Varying the symmetry energy to the value of the Shen EOS enlarges the neutron star radius. Modifying all nuclear matter properties to the Shen values results in a similar MR curve compared to the original Shen EOS. This suggests that the MR relation is mainly governed by nuclear matter properties and not the underlying theory.

We tested our EOS models in the simulation code GR1D [74, 89], which is based on a relativistic formulation of the hydrodynamic equations, and chose two different neutrino transport schemes, the M1 transport scheme [74] and a gray neutrino leakage [89, 118]. The simulations with M1 in GR1D are performed without enhanced heating and fail to explode. However, the PNS radii entirely agree with the results obtained with the FLASH code. Additionally, our findings show that the leakage scheme does not reproduce the electron fraction accurately compared to the previous M1 values, as expected, which originates from the simplified deleptonization. This affects the entropy and consequently the temperature. Attempts to adapt the electron fraction profile in the deleptonization scheme to values obtained with M1 still failed to reproduce transport results. We concluded that a gray leakage scheme is not adequate to investigate the impact of nuclear matter properties in the PNS interior.

In the second part of this thesis, we presented our approach for an extension of the nuclear EOS to low densities and temperatures. With this, we were able to perform the first long-time CCSN simulations in FLASH for exploding models, following the shock expansion up to five seconds after bounce. We investigated different CCSN scenarios varying the rotational profile and the explosion energetics by enhancing the neutrino energy deposition in the neutrino leakage scheme.

The first step was to develop an EOS transition. We described our formalism for an EOS extension and tested it for various nuclear EOS and different progenitors in spherical symmetry. Additionally, we verified its functionality in cylindrically symmetric simulations and for various neutrino schemes, including a gray leakage [117], advanced spectral leakage [79], and an M1 transport scheme [82].

With this extension of the EOS, we performed long-time CCSN simulations in FLASH, with a gray neutrino leakage [117] and a 15 $M_\odot$ progenitor [36]. We investigated the impact of rotation and artificial heating in cylindrically symmetric simulations, running a total of 24 simulations, including 6 different heating factors and 7 additional rotational profiles. Out of the 24 simulations, 13 do not result in a successful explosion. An increased heating of at least 5 % is necessary to revive the shock wave, and additional rotation seems to be less favorable for the onset of an explosion. Neutrino-driven winds form in 5 of our models and appear to be supported by additional rotation. We investigated 9 exploding cases in detail, including 5 different heating factors and 5 rotational profiles. As the models with an increased heating of 10 % and added rotation fail to explode, we plan to run additional models with rotation and a heating of 20 %.

We found that simulations with higher heating factors yield earlier explosions. The diagnostic energy is largest for the highest heating factor and decreases with smaller heating. Rapid rotation slightly delays the explosion time, although not significantly (less than 50 ms), whereas moderate rotation has no visible impact on the shock propagation. For models where a steady neutrino-driven wind develops, the diagnostic energy saturates and is smaller compared to cases without a wind. This is a result of the constant mass outflow that prevents matter from being accreted onto the PNS. The mass accretion rate is reduced for higher heating factors. This is correlated with the early shock expansion, where a significant amount of matter is carried away from the PNS at an early stage, also resulting in smaller PNS masses and less accretion. Additional rotation decreases the mass accretion and slightly impacts the PNS mass. Further, the neutrino luminosities are affected by rotation, see also Ref. [189]. At the poles, which correspond to the rotational axes, matter is moved away from the PNS towards the equatorial plane. This reduces the neutrino luminosities at the poles for rotating cases, leading to smaller integrated luminosities. We additionally investigated the impact of rotation on the shock morphology. Models without additional rotation show a prolate expansion along the poles, which is attributed to the cylindrical symmetry [195]. For the two rapidly rotating models, the shock expansion is almost spherical.

Finally, we compared the simulations with a neutrino leakage scheme to simulations performed with an M1 transport. As the latter is computationally more expensive, we were solely able to compare the first 500 ms after bounce. We chose two simulations where the diagnostic energies are approximately equal in order to explore similar explosion dynamics. While the spherically averaged profiles of shock radius, neutrino energy deposition, and radial velocity are in reasonable agreement, electron fraction and also entropy show significant differences. This is a result of the electron fraction that is not accurate in the neutrino leakage scheme, which needs to be considered for future nucleosynthesis calculations.

The results presented in this thesis provided a first, systematic analysis of the impact of uncertainties in the EOS in CCSN simulations, and further opened the possibility to perform long-time simulations with the FLASH code.

Having an overview how individual nuclear matter properties in the EOS affect supernova simulations, we can work towards improving the EOS for astrophysical applications with ab initio theories and updated nuclear physics input. This requires combined effort from astrophysics, nuclear experiments, theoretical calculations, and observations. Moreover, the era of gravitational wave detection has only begun [30]. Measurements of binary neutron star mergers and core-collapse supernovae will help to further constrain the EOS, e.g., [145, 146]. Systematic explorations of EOS uncertainties in multi-dimensional simulations are yet to be performed and may provide new insights.

Performing long-time simulations is a next step to close the gap between supernova simulations and the observation of stellar remnants [204]. Investigating the factors that are crucial for the explosion mechanism and conducting nucleosynthesis studies provides more pieces for the supernova puzzle. The fast advances that are made in high-performance computing will enable us to perform three-dimensional, long-time simulations, and also include an improved neutrino transport. Finally, the next galactic supernova will contribute greatly to our understanding.

A Simulation Details

Chapter 4. Equation of State

Figure 4.1: M1 simulation with FLASH from Chapter 5 with the LS220 EOS.

Figure 4.7: Density, temperature, and electron fraction from the leakage simulation in Chapter 6 with the LS220 EOS (without hybrid). Evaluated with the LS code [178] and the Timmes EOS [205].

Figure 4.8: Same as Fig. 4.7.

Chapter 5. Equation of State Effects in Core-Collapse Supernovae

FLASH

Version: FLASH 4.2.2, branch: `master`, commit: 94adcaf, Date: 08.09.2018, Cluster: Europium

```
./setup CoreCollapse/M1 —auto —1d +spherical —objdir "${simulationDirName}/src"
—nxb=20 threadBlockList=False +pm4dev threadWithinBlock=False
+newMpole +spark —site eu.tu—darmstadt.de \
——with—unit=physics/Eos/EosMain/Nuclear \
——with—unit=physics/RadTrans/RadTransMain/M1/twoStep m1_groups=18 || exit 1
```

Gravitational potential: GR [82].
Solver: Spark [206].

domain	nblockx	lrefine_max	interpol_order	cfl	mpole_effpotnum
$1 \cdot 10^9$ cm	10	10	2	0.4	1000

GR1D

Version: GR1Dv2, branch: `master`, commit: 2e0b746, Date: 13.07.2017

	grid_custom_rad1	grid_custom_dx1	radial_zones	number_groups
M1	20.0d5	3.0d4	600	18
Leakage	20.0d5	1.0d4	1500	-

Chapter 6. Equation of State Transition

Version: FLASH 4.2.2, branch: `new_ccsn_nucleo`, commit: 5788a46, Date: 14.09.2018

Gravitational potential: Newtonian.
Solver: Unsplit [85, 86].

Setup line without hybrid:

```
./setup CoreCollapse —auto —1d +spherical +uhd —objdir "${simulationDirName}/src"
—nxb=16 threadBlockList=False +pm4dev threadWithinBlock=False +newMpole
——with—unit=physics/Eos/EosMain/Nuclear
——with—unit=physics/RadTrans/RadTransMain/NeutrinoLeakage
——with—unit=physics/sourceTerms/Deleptonize/DeleptonizeMain || exit 1
```

Setup line with hybrid:

```
./setup CoreCollapse —auto —1d +spherical +uhd —objdir m"${simulationDirName}/src"
—nxb=16 threadBlockList=False +pm4dev threadWithinBlock=False +newMpole
——with—unit=physics/Eos/EosMain/Hybrid
——with—unit=physics/RadTrans/RadTransMain/NeutrinoLeakage
——with—unit=physics/sourceTerms/Deleptonize/DeleptonizeMain || exit 1
```

Note: To have the same resolution despite a different simulation domain, the refinement level (lrefine_max) has to be adopted. Increasing the domain by a factor of 2, requires one more level in refinement.

	domain	nblockx	lrefine_max	order	cfl	leak_numTht
w/o hybrid	$4 \cdot 10^9$ cm	5	11	3	0.5	37
hybrid	$6.4 \cdot 10^{10}$ cm	5	15	3	0.5	37

Leakage

Version: FLASH 4.2.2, branch: `master`, commit: 94adcaf, Date: 09.07.2018, Cluster: Lichtenberg

```
./setup CoreCollapse/Tracer —auto —2d +cylindrical —objdir leak_hyb_uhd/source
—nxb=16 —nyb=16 —site max.tu—darmstadt.de threadBlockList=False
+pm4dev threadWithinBlock=False +newMpole +uhd
——with—unit=physics/RadTrans/RadTransMain/NeutrinoLeakage
——with—unit=physics/sourceTerms/Deleptonize
——with—unit=physics/Eos/EosMain/Hybrid
```

Gravitational potential: Newtonian.
Solver: Unsplit [85, 86].

domain x/-y/y	nblockx/y	lrefine_max	interpol_order	cfl	leak_numTht
$1.6 \cdot 10^{10}$ cm	20/40	11	3	0.5	37

M1

Version: FLASH 4.2.2, branch: `master`, commit: 7e777ac, Date: 08.09.2018, Cluster: Europium

```
./setup CoreCollapse/M1 —auto —2d +cylindrical —objdir "${simulationDirName}/source"
—nxb=16 —nyb=16 threadBlockList=False +pm4dev threadWithinBlock=False
 +newMpole +spark —site eu.tu—darmstadt.de \
——with—unit=physics/Eos/EosMain/Hybrid \
——with—unit=physics/RadTrans/RadTransMain/M1/twoStep m1_groups=18 || exit 1
```

Gravitational potential: GR [82].
Solver: Spark [206].

domain x/-y/y	nblockx/y	lrefine_max	interpol_order	cfl	mpole_effpotnum
$1.6 \cdot 10^{10}$ cm	20/40	11	2	0.4	1000

Bibliography

[1] Image Credit: ESO, `https://www.eso.org/public/images/eso0708b/`, accessed: 16.11.2018.

[2] A. S. Eddington, Observatory **43**, 341 (1920).

[3] H. A. Bethe, Phys. Rev. **55**, 434 (1939).

[4] E. M. Burbidge, G. R. Burbidge, W. A. Fowler, and F. Hoyle, Rev. Mod. Phys. **29**, 547 (1957).

[5] A. G. W. Cameron, Publ. Astron. Soc. Pac. **69**, 201 (1957).

[6] W. Baade, and F. Zwicky, Phys. Rev. **46**, 76 (1934).

[7] J. Chadwick, Nature **129**, 312 (1932).

[8] A. Hewish, S. J. Bell, J. D. H. Pilkington, P. F. Scott, and R. A. Collins, Nature **217**, 709 (1968).

[9] D. H. Staelin, and E. C. Reifenstein, III, Science **162**, 1481 (1968).

[10] M. I. Large, A. E. Vaughan, and B. Y. Mills, Nature **220**, 340 (1968).

[11] Image Credit: NASA and the Night Sky Network, `https://imagine.gsfc.nasa.gov/science/objects/stars1.html`, accessed: 08.12.2018.

[12] S. A. Colgate, and M. H. Johnson, Phys. Rev. Lett. **5**, 235 (1960).

[13] S. A. Colgate, W. H. Grasberger, and R. H. White, Astron. J. **66**, 280 (1961).

[14] J. R. Wilson, Astrophys. J. **163**, 209 (1971).

[15] S. A. Colgate, and R. H. White, Astrophys. J. **143**, 626 (1966).

[16] H. A. Bethe, and J. R. Wilson, Astrophys. J. **295**, 14 (1985).

[17] H.-T. Janka, *Supernovae und kosmische Gammablitze* (Spektrum Akademischer Verlag, 2011).

[18] W. D. Arnett, J. N. Bahcall, R. P. Kirshner, and S. E. Woosley, Annu. Rev. Astron. Astrophys. **27**, 629 (1989).

[19] W. Hillebrandt, and P. Hoflich, Rep. Prog. Phys. **52**, 1421 (1989).

[20] A. Burrows, J. Hayes, and B. A. Fryxell, Astrophys. J. **450**, 830 (1995).

[21] M. Herant, W. Benz, W. R. Hix, C. L. Fryer, and S. A. Colgate, Astrophys. J. **435**, 339 (1994).

[22] H.-T. Janka, and E. Mueller, Astrophys. J. Lett. **448**, L109 (1995).

[23] T. Melson, H.-T. Janka, and A. Marek, Astrophys. J. Lett. **801**, L24 (2015).

[24] E. J. Lentz, S. W. Bruenn, W. R. Hix, A. Mezzacappa, O. E. B. Messer, E. Endeve, J. M. Blondin, J. A. Harris, P. Marronetti, and K. N. Yakunin, Astrophys. J. Lett. **807**, L31 (2015).

[25] Image Credit: David Malin / Australian Astronomical Observatory, `https://www.aao.gov.au/news-media/media-releases/Supernova1987A-30`, accessed: 03.12.2018.

[26] J. M. Lattimer, and M. Prakash, Phys. Rep. **621**, 127 (2016).

[27] J. M. Lattimer, and Y. Lim, Astrophys. J. **771**, 51 (2013).

[28] J. Antoniadis *et al.*, Science **340**, 1233232 (2013).

[29] P. B. Demorest, T. Pennucci, S. M. Ransom, M. S. E. Roberts, and J. W. T. Hessels, Nature **467**, 1081 (2010).

[30] B. P. Abbott *et al.* (The LIGO Scientific Collaboration and the Virgo Collaboration), Phys. Rev. Lett. **121**, 161101 (2018).

[31] H.-T. Janka, Annu. Rev. Nucl. Part. Sci. **62**, 407 (2012).

[32] H.-T. Janka, "Neutrino-driven explosions," in *Handbook of Supernovae* (Springer International Publishing AG, 2017) p. 1095.

[33] H. A. Bethe, Rev. Mod. Phys. **62**, 801 (1990).

[34] R. Kippenhahn, A. Weigert, and A. Weiss, *Stellar Structure and Evolution* (Springer-Verlag Berlin Heidelberg, 2012).

[35] S. Woosley, and T. Janka, Nat. Phys. **1**, 147 (2005).

[36] S. E. Woosley, A. Heger, and T. A. Weaver, Rev. Mod. Phys. **74**, 1015 (2002).

[37] H.-T. Janka, K. Langanke, A. Marek, G. Martínez-Pinedo, and B. Müller, Phys. Rep. **442**, 38 (2007).

[38] F. Hoyle, and W. A. Fowler, Astrophys. J. **132**, 565 (1960).

[39] A. Burrows, Rev. Mod. Phys. **85**, 245 (2013).

[40] H. T. Janka, T. Melson, and A. Summa, Annu. Rev. Nucl. Part. Sci. **66**, 341 (2016).

[41] D. Arnett, Can. J. Phys. **45**, 1621 (1967).

[42] H.-T. Janka, Astron. Astrophys. **368**, 527 (2001).

[43] B. Müller, Publ. Astron. Soc. Aust. **33**, e048 (2016).

[44] A. Burrows, and J. Goshy, Astrophys. J. Lett. **416**, L75 (1993).

[45] S. Wanajo, B. Müller, H.-T. Janka, and A. Heger, Astrophys. J. **852**, 40 (2018).

[46] R. C. Duncan, S. L. Shapiro, and I. Wasserman, Astrophys. J. **309**, 141 (1986).

[47] Y.-Z. Qian, and G. Wasserburg, Phys. Rep. **333**, 77 (2000).

[48] Y.-Z. Qian, and G. J. Wasserburg, Astrophys. J. **559**, 925 (2001).

[49] A. Arcones, and F. K. Thielemann, J. Phys. G **40**, 013201 (2013).

[50] F. S. Kitaura, H.-T. Janka, and W. Hillebrandt, Astron. Astrophys. **450**, 345 (2006).

[51] T. Fischer, S. C. Whitehouse, A. Mezzacappa, F.-K. Thielemann, and M. Liebendörfer, Astron. Astrophys. **517**, A80 (2010).

[52] Image Credit: ESA/Hubble, NASA, `https://apod.nasa.gov/apod/ap170305.html`, accessed: 21.10.2018.

[53] J. M. Blondin, A. Mezzacappa, and C. DeMarino, Astrophys. J. **584**, 971 (2003).

[54] J. M. Blondin, and A. Mezzacappa, Nature **445**, 58 (2007).

[55] R. Fernández, Astrophys. J. **725**, 1563 (2010).

[56] M. Ugliano, H.-T. Janka, A. Marek, and A. Arcones, Astrophys. J. **757**, 69 (2012).

[57] O. Pejcha, and T. A. Thompson, Astrophys. J. **801**, 90 (2015).

[58] T. Ertl, H. T. Janka, S. E. Woosley, T. Sukhbold, and M. Ugliano, Astrophys. J. **818**, 124 (2016).

[59] J. M. Lattimer, and M. Prakash, Science **304**, 536 (2004).

[60] L. D. Landau, Phys. Z. Sowjetunion **1**, 285 (1932).

[61] Image Credit: NASA, ESA, J. Hester, A. Loll (ASU); Acknowledgment: Davide De Martin (Skyfactory), `https://apod.nasa.gov/apod/ap111225.html`, accessed: 03.11.2018.

[62] Image Credit and Copyright: CEDIC Team - Processing: Wolfgang Leitner, `https://apod.nasa.gov/apod/ap150101.html`, accessed: 03.11.2018.

[63] J. R. Oppenheimer, and G. M. Volkoff, Phys. Rev. **55**, 374 (1939).

[64] J. M. Lattimer, and M. Prakash, Phys. Rep. **442**, 109 (2007).

[65] K. Hebeler, J. M. Lattimer, C. J. Pethick, and A. Schwenk, Phys. Rev. Lett. **105**, 161102 (2010).

[66] E. Müller, "Simulation of Astrophysical Fluid Flow," in *Computational Methods for Astrophysical Fluid Flow* (Springer-Verlag Berlin Heidelberg, 1998) p. 343.

[67] K. Huang, *Statistical mechanics* (Wiley, 1987).

[68] D. H. Weinberg, *Radiative Gas Dynamics* (Lecture notes, Ohio State University, 2007) `http://www.astronomy.ohio-state.edu/~dhw/A825/notes2.pdf`.

[69] B. Ryden, *Radiative Gas Dynamics* (Lecture notes, Ohio State University, 2011) `http://www.astronomy.ohio-state.edu/~ryden/ast825/ch1-3.pdf`.

[70] R. Käppeli, and S. Mishra, Astron. Astrophys. **587**, A94 (2016).

[71] M. Zingale, *Introduction to Computational Astrophysical Hydrodynamics* (The Open Astrophysics Bookshelf, 2018) `http://bender.astro.sunysb.edu/hydro_by_example/CompHydroTutorial.pdf`.

[72] B. Müller, H.-T. Janka, and H. Dimmelmeier, Astrophys. J. Suppl. **189**, 104 (2010).

[73] T. Kuroda, K. Kotake, and T. Takiwaki, Astrophys. J. **755**, 11 (2012).

[74] E. O'Connor, Astrophys. J. Suppl. Ser. **219**, 24 (2015).

[75] FLASH center, `http://flash.uchicago.edu/site/flashcode/`, accessed: 15.11.2018.

[76] B. Fryxell, E. Müller, and D. Arnett, *Hydrodynamics and nuclear burning* (Max-Planck-Inst. für Physik und Astrophysik, 1989).

[77] B. Fryxell, K. Olson, P. Ricker, F. X. Timmes, M. Zingale, D. Q. Lamb, P. MacNeice, R. Rosner, J. W. Truran, and H. Tufo, Astrophys. J. Suppl. Ser. **131**, 273 (2000).

[78] A. Dubey, K. Antypas, M. K. Ganapathy, L. B. Reid, K. Riley, D. Sheeler, A. Siegel, and K. Weide, Parallel Comput. **35**, 512 (2009).

[79] K.-C. Pan, C. Mattes, E. O'Connor, S. M. Couch, A. Perego, and A. Arcones, J. Phys. G **46**, 014001 (2019).

[80] M. Rampp, and H. T. Janka, Astron. Astrophys. **396**, 361 (2002).

[81] A. Marek, H. Dimmelmeier, H. T. Janka, E. Muller, and R. Buras, Astron. Astrophys. **445**, 273 (2006).

[82] E. O'Connor, and S. M. Couch, Astrophys. J. **854**, 63 (2018).

[83] P. Colella, and P. Woodward, J. Comput. Phys. **54**, 174 (1984).

[84] P. Woodward, and P. Colella, J. Comput. Phys. **54**, 115 (1984).

[85] D. Lee, and A. E. Deane, J. Comput. Phys. **228**, 952 (2009).

[86] D. Lee, J. Comput. Phys. **243**, 269 (2013).

[87] P. MacNeice, K. M. Olson, C. Mobarry, R. de Fainchtein, and C. Packer, Comput. Phys. Commun. **126**, 330 (2000).

[88] E. O'Connor, `http://www.GR1Dcode.org`, accessed: 15.11.2018.

[89] E. O'Connor, and C. D. Ott, Class. Quant. Grav. **27**, 114103 (2010).

[90] E. Gourgoulhon, Astron. Astrophys. **252**, 651 (1991).

[91] J. V. Romero, J. M. A. Ibanez, J. M. A. Marti, and J. A. Miralles, Astrophys. J. **462**, 839 (1996).

[92] M. Liebendörfer, Astrophys. J. **633**, 1042 (2005).

[93] E. O'Connor *et al.*, J. Phys. G **45**, 104001 (2018).

[94] R. W. Lindquist, Ann. Phys. **37**, 487 (1966).

[95] H.-T. Janka, F. Hanke, L. Hüdepohl, A. Marek, B. Müller, and M. Obergaulinger, Prog. Theor. Exp. Phys. **2012**, 01A309 (2012).

[96] A. Mezzacappa, and S. W. Bruenn, Astrophys. J. **405**, 637 (1993).

[97] H.-T. Janka, and W. Hillebrandt, Astron. Astrophys. Suppl. Ser. **78**, 375 (1989).

[98] K. Sumiyoshi, and S. Yamada, Astrophys. J. Suppl. Ser. **199**, 17 (2012).

[99] S. W. Bruenn, Astrophys. J. Suppl. Ser. **58**, 771 (1985).

[100] M. Liebendoerfer, S. C. Whitehouse, and T. Fischer, Astrophys. J. **698**, 1174 (2009).

[101] A. Perego, S. Rosswog, R. M. Cabezón, O. Korobkin, R. Käppeli, A. Arcones, and M. Liebendörfer, Mon. Not. R. Astron. Soc. **443**, 3134 (2014).

[102] M. Ruffert, H.-T. Janka, and G. Schaefer, Astron. Astrophys. **311**, 532 (1996).

[103] F. Hanke, B. Müller, A. Wongwathanarat, A. Marek, and H.-T. Janka, Astrophys. J. **770**, 66 (2013).

[104] I. Tamborra, F. Hanke, B. Müller, H.-T. Janka, and G. Raffelt, Phys. Rev. Lett. **111**, 121104 (2013).

[105] M. Shibata, K. Kiuchi, Y. Sekiguchi, and Y. Suwa, Prog. Theor. Phys. **125**, 1255 (2011).

[106] C. Y. Cardall, E. Endeve, and A. Mezzacappa, Phys. Rev. D **88**, 023011 (2013).

[107] O. Just, M. Obergaulinger, and H. T. Janka, Mon. Not. R. Astron. Soc. **453**, 3386 (2015).

[108] R. B. Lowrie, D. Mihalas, and J. E. Morel, J. Quant. Spec. Radiat. Transf. **69**, 291 (2001).

[109] J. I. Castor, Astrophys. J. **178**, 779 (1972).

[110] C. Levermore, J. Quant. Spec. Radiat. Transf. **31**, 149 (1984).

[111] G. N. Minerbo, J. Quant. Spec. Radiat. Transf. **20**, 541 (1978).

[112] J. A. Pons, J. M. Ibanez, and J. A. Miralles, Mon. Not. R. Astron. Soc. **317**, 550 (2000).

[113] E. M. Murchikova, E. Abdikamalov, and T. Urbatsch, Mon. Not. R. Astron. Soc. **469**, 1725 (2017).

[114] E. O'Connor, `https://github.com/evanoconnor/nulib`, accessed: 04.11.2018.

[115] C. J. Horowitz, Phys. Rev. D **65**, 043001 (2002).

[116] A. Burrows, S. Reddy, and T. A. Thompson, Nucl. Phys. A **777**, 356 (2006).

[117] S. M. Couch, and E. O'Connor, Astrophys. J. **785**, 123 (2014).

[118] S. Rosswog, and M. Liebendörfer, Mon. Not. R. Astron. Soc. **342**, 673 (2003).

[119] C. D. Ott, E. Abdikamalov, P. Mösta, R. Haas, S. Drasco, E. O'Connor, C. Reisswig, C. A. Meakin, and E. Schnetter, Astrophys. J. **768**, 115 (2013).

[120] J. M. Lattimer, and F. D. Swesty, Nucl. Phys. A **535**, 331 (1991).

[121] M. Hempel, T. Fischer, J. Schaffner-Bielich, and M. Liebendörfer, Astrophys. J. **748**, 70 (2012).

[122] A. S. Schneider, L. F. Roberts, and C. D. Ott, Phys. Rev. C **96**, 065802 (2017).

[123] `https://stellarcollapse.org/microphysics`, accessed: 25.11.2018.

[124] E. O'Connor, and C. D. Ott, `https://stellarcollapse.org/equationofstate`, accessed: 04.11.2018.

[125] A. S. Schneider, L. F. Roberts, and C. D. Ott, `https://bitbucket.org/andschn/sroeos`, accessed: 04.11.2018.

[126] F. Schwabl, *Statistische Mechanik* (Springer-Verlag Berlin Heidelberg, 2006).

[127] K. Hebeler, J. M. Lattimer, C. J. Pethick, and A. Schwenk, Astrophys. J. **773**, 11 (2013).

[128] K. Hebeler, J. D. Holt, J. Menendez, and A. Schwenk, Annu. Rev. Nucl. Part. Sci. **65**, 457 (2015).

[129] C. Drischler, K. Hebeler, and A. Schwenk, Phys. Rev. C **93**, 054314 (2016).

[130] D. Mihalas, and B. W. Mihalas, *Foundations of radiation hydrodynamics* (Oxford University Press, 1984).

[131] C. Iliadis, *Nuclear Physics of Stars* (Wiley-VCH, 2008).

[132] J. M. Lattimer, Annu. Rev. Nucl. Part. Sci. **62**, 485 (2012).

[133] J. M. Lattimer, and A. W. Steiner, Eur. Phys. J. A **50**, 40 (2014).

[134] M. Oertel, M. Hempel, T. Klähn, and S. Typel, Rev. Mod. Phys. **89**, 015007 (2017).

[135] E. Fonseca *et al.*, Astrophys. J. **832**, 167 (2016).

[136] H. Shen, H. Toki, K. Oyamatsu, and K. Sumiyoshi, Prog. Theor. Phys. **100**, 1013 (1998).

[137] K. Hebeler, T. Duguet, T. Lesinski, and A. Schwenk, Phys. Rev. C **80**, 044321 (2009).

[138] K. Hebeler, S. K. Bogner, R. J. Furnstahl, A. Nogga, and A. Schwenk, Phys. Rev. C **83**, 031301(R) (2011).

[139] C. Wellenhofer, J. W. Holt, N. Kaiser, and W. Weise, Phys. Rev. C **89**, 064009 (2014).

[140] C. Drischler, T. Krüger, K. Hebeler, and A. Schwenk, Phys. Rev. C **95**, 024302 (2017).

[141] C. Drischler, K. Hebeler, and A. Schwenk, Phys. Rev. Lett. **122**, 042501 (2019).

[142] S. Shlomo, V. M. Kolomietz, and G. Colò, Eur. Phys. J. A **30**, 23 (2006).

[143] K. Hebeler, and A. Schwenk, Phys. Rev. C **82**, 014314 (2010).

[144] T. Krüger, I. Tews, K. Hebeler, and A. Schwenk, Phys. Rev. C **88**, 025802 (2013).

[145] B. P. Abbott *et al.* (LIGO Scientific Collaboration and Virgo Collaboration), Phys. Rev. X **9** (2019).

[146] S. De, D. Finstad, J. M. Lattimer, D. A. Brown, E. Berger, and C. M. Biwer, Phys. Rev. Lett. **121**, 091102 (2018).

[147] E. R. Most, L. R. Weih, L. Rezzolla, and J. Schaffner-Bielich, Phys. Rev. Lett. **120**, 261103 (2018).

[148] A. Bauswein, O. Just, H.-T. Janka, and N. Stergioulas, Astrophys. J. Lett. **850**, L34 (2017).

[149] T. H. R. Skyrme, Phil. Mag. **1**, 1043 (1956).

[150] T. H. R. Skyrme, Nucl. Phys. **9**, 615 (1958).

[151] D. Vautherin, and D. M. Brink, Phys. Rev. C **5**, 626 (1972).

[152] J. Lattimer, C. Pethick, D. Ravenhall, and D. Lamb, Nucl. Phys. A **432**, 646 (1985).

[153] J. M. Lattimer, and D. G. Ravenhall, Astrophys. J. **223**, 314 (1978).

[154] S. Schäfer, *Equation of state effects in core–collapse supernovae*, Master's thesis, TU Darmstadt (2018).

[155] S. Schäfer, H. Yasin, A. Arcones, and A. Schwenk, *in prep.* (2018).

[156] H. Shen, H. Toki, K. Oyamatsu, and K. Sumiyoshi, Nucl. Phys. A **637**, 435 (1998).

[157] H. Shen, H. Toki, K. Oyamatsu, and K. Sumiyoshi, Astrophys. J. Suppl. Ser. **197**, 20 (2011).

[158] H. Yukawa, Proc. Phys. Math. Soc. Jap. **17**, 48 (1935).

[159] Y. Sugahara, and H. Toki, Nucl. Phys. A **579**, 557 (1994).

[160] A. Marek, H.-T. Janka, and E. Müller, Astron. Astrophys. **496**, 475 (2009).

[161] S. M. Couch, Astrophys. J. **765**, 29 (2013).

[162] M. Hempel, and J. Schaffner-Bielich, Nucl. Phys. A **837**, 210 (2010).

[163] A. W. Steiner, M. Hempel, and T. Fischer, Astrophys. J. **774**, 17 (2013).

[164] G. Shen, C. J. Horowitz, and S. Teige, Phys. Rev. C **82**, 015806 (2010).

[165] E. Chabanat, P. Bonche, P. Haensel, J. Meyer, and R. Schaeffer, Nucl. Phys. A **635**, 231 (1998).

[166] H. Toki, D. Hirata, Y. Sugahara, K. Sumiyoshi, and I. Tanihata, Nucl. Phys. A **588**, c357 (1995).

[167] B. G. Todd-Rutel, and J. Piekarewicz, Phys. Rev. Lett. **95**, 122501 (2005).

[168] A. W. Steiner, J. M. Lattimer, and E. F. Brown, Astrophys. J. **722**, 33 (2010).

[169] J. R. Stone, and P. G. Reinhard, Prog. Part. Nucl. Phys. **58**, 587 (2007).

[170] F. X. Timmes, `http://cococubed.asu.edu/code_pages/chemical_potential.shtml`, accessed: 21.10.2018.

[171] F. X. Timmes, and D. Arnett, Astrophys. J. Suppl. Ser. **125**, 277 (1999).

[172] F. X. Timmes, and F. D. Swesty, Astrophys. J. Suppl. Ser. **126**, 501 (2000).

[173] F. X. Timmes, `http://cococubed.asu.edu/code_pages/fermi_dirac.shtml`, accessed: 24.11.2018.

[174] D. G. Yakovlev, and D. A. Shalybkov, Adv. Space Res. **8**, 707 (1988).

[175] D. Yakovlev, R. Syunyaev, and D. Shalybkov, *Degenerate Cores of White Dwarfs and Envelopes of Neutron Stars: Thermodynamics and Plasma Screening in Thermonuclear Reactions* (Harwood Academic Publishers, 1989).

[176] H. Yasin, S. Schäfer, A. Arcones, and A. Schwenk, arXiv:1812.02002.

[177] Y. Suwa, T. Takiwaki, K. Kotake, T. Fischer, M. Liebendörfer, and K. Sato, Astrophys. J. **764**, 99 (2013).

[178] J. M. Lattimer, and F. D. Swesty, `http://www.astro.sunysb.edu/dswesty/lseos.html`, accessed: 04.11.2018.

[179] H. Bethe, G. Brown, J. Applegate, and J. Lattimer, Nucl. Phys. A **324**, 487 (1979).

[180] T. J. Mazurek, G. E. Brown, and J. M. Lattimer, Astrophys. J. **229**, 713 (1979).

[181] M. Baldo, and G. F. Burgio, Prog. Part. Nucl. Phys. **91**, 203 (2016).

[182] G. Baym, and C. J. Pethick, *Landau Fermi–Liquid Theory* (Wiley-Blackwell, 2007).

[183] A. Bauswein, H.-T. Janka, and R. Oechslin, Phys. Rev. D **82**, 084043 (2010).

[184] C. Constantinou, B. Muccioli, M. Prakash, and J. M. Lattimer, Phys. Rev. C **92**, 025801 (2015).

[185] S. E. Woosley, and A. Heger, Phys. Rep. **442**, 269 (2007).

[186] L. Scheck, K. Kifonidis, H.-T. Janka, and E. Müller, Astron. Astrophys. **457**, 963 (2006).

[187] A. Heger, S. E. Woosley, and H. C. Spruit, Astrophys. J. **626**, 350 (2005).

[188] K. Nakamura, T. Kuroda, T. Takiwaki, and K. Kotake, Astrophys. J. **793**, 45 (2014).

[189] A. Summa, H.-T. Janka, T. Melson, and A. Marek, Astrophys. J. **852**, 28 (2018).

[190] C. L. Fryer, and A. Heger, Astrophys. J. **541**, 1033 (2000).

[191] R. Buras, M. Rampp, H.-T. Janka, and K. Kifonidis, Phys. Rev. Lett. **90**, 241101 (2003).

[192] K. Kotake, S. Yamada, and K. Sato, Astrophys. J. **595**, 304 (2003).

[193] R. Walder, A. Burrows, C. D. Ott, E. Livne, I. Lichtenstadt, and M. Jarrah, Astrophys. J. **626**, 317 (2005).

[194] C. D. Ott, A. Burrows, T. A. Thompson, E. Livne, and R. Walder, Astrophys. J. Suppl. Ser. **164**, 130 (2006).

[195] K. Kotake, K. Sato, and K. Takahashi, Rep. Prog. Phys. **69**, 971 (2006).

[196] A. Marek, and H.-T. Janka, Astrophys. J. **694**, 664 (2009).

[197] Y. Suwa, K. Kotake, T. Takiwaki, S. C. Whitehouse, M. Liebendörfer, and K. Sato, Publ. Astron. Soc. Jpn. **62**, L49 (2010).

[198] M. Obergaulinger, O. Just, and M. Aloy, J. Phys. G **45**, 084001 (2018).

[199] C. L. Fryer, and M. S. Warren, Astrophys. J. **601**, 391 (2004).

[200] J. A. Harris, W. R. Hix, M. A. Chertkow, C. T. Lee, E. J. Lentz, and O. E. B. Messer, Astrophys. J. **843**, 2 (2017).

[201] M. Eichler, K. Nakamura, T. Takiwaki, T. Kuroda, K. Kotake, M. Hempel, R. Cabezón, M. Liebendörfer, and F.-K. Thielemann, J. Phys. G **45**, 014001 (2018).

[202] N. Nishimura, T. Takiwaki, and F. K. Thielemann, Astrophys. J. **810**, 109 (2015).

[203] J. Bliss, M. Witt, A. Arcones, F. Montes, and J. Pereira, Astrophys. J. **855**, 135 (2018).

[204] A. Wongwathanarat, H.-T. Janka, E. Müller, E. Pllumbi, and S. Wanajo, Astrophys. J. **842**, 13 (2017).

[205] Timmes, F. X., `http://cococubed.asu.edu/code_pages/eos.shtml`, accessed: 15.12.2018.

[206] S. M. Couch, *in prep.* (2019).

Acknowledgments

An dieser Stelle möchte ich mich bei allen bedanken, die zum Entstehen dieser Arbeit in irgendeiner Form beigetragen haben.

Allen voran bedanke ich mich bei meiner Doktormutter Almudena Arcones. Seit mehr als sechs Jahren darf ich Teil der Arbeitsgruppe sein, die im Laufe der Jahre fast schon so etwas wie eine Familie geworden ist. Danke für all Deine Unterstützung, Ratschläge und die vielen Diskussionen, bei denen ich unendlich viel von Dir lernen konnte. Mit Dir zusammen zuarbeiten ist eine große Inspiration für mich. Außerdem möchte ich mich dafür bedanken, dass Du es mir ermöglicht hast, an so vielen Konferenzen, Workshops und Schools teilzunehmen.

Weiterhin möchte ich mich bei Achim Schwenk für das Zweitgutachten dieser Dissertation, und aber vor allem für das wunderbare "effektive Masse" Thema bedanken. Die Arbeit hat mir unglaublich viel Spaß gemacht, und ich habe viel in den letzten Jahren über die Kernphysik von Dir gelernt.

Besonderer Dank gilt den Menschen, mit denen ich die letzten Jahre sehr eng zusammen gearbeitet habe. Allen voran Sabrina Schäfer, für die weltbeste Zusammenarbeit in den letzten zwei Jahren. Die Arbeit mit Dir hat mir sehr, sehr viel Freude bereitet, und ich bin ziemlich dankbar dafür, dass wir so zueinander gefunden haben. Ich bedanke mich bei Carlos Mattes für unendlichen FLASH Support und bei Max Witt für all die "dirty hacks", die mein Leben erleichtert haben.

Außerdem möchte ich mich bei all den Menschen in der Astrogruppe (seit Anbeginn der Zeit!) bedanken. Bei Julia Bliss, für all Deine Unterstützung in den letzten sechs Jahren. Bei der "Boulder-Crew" Max J. und Jonas, insbesondere Jonas für sein unendliches Python-Wissen. Außerdem Albino, Camilla, Dirk, Federico, Marcella, Marius, Martin, Moritz, Paul, Takami und Wida. Die fachlichen Gespräche, verrücktesten Themen beim Mittagessen, und diverse off-topic Aktivitäten haben immer viel Spaß gemacht.

Für die prima Arbeitsatmosphäre bedanke ich mich beim ehemaligen Büro Nummer 1, und dem jetzigen Büro 103. Insbesondere Sandra, mit der ich die ersten Jahre "Rücken-an-Rücken" gesessen habe. Danke für all unsere Gespräche, Basteleien und die schönen Momente außerhalb der Physik.

Ein großes Dankeschön geht an Almudena, Carlos, Max W., Sabrina, Stefan und Takami für das (teilweise) Korrekturlesen dieser Arbeit. Insbesondere an Almudena und Stefan, die alles gelesen haben.

Im Laufe meines Studiums durfte ich ganz wunderbaren Menschen begegnen, die große Teile des Wahnsinns sehr viel besser gemacht haben. Shoutout to Andi, Fabi, Manuel, Stefan, Toni und sämtliche Menschen in der Fachschaft Physik. Außerdem die Spielegruppe "Gigantischer Gewinn" für wunderbare Dienstag Abende mit Anna, Bastian, Pia, Stefan und Toni.

Von Herzen bedanke ich mich bei meinen Yogamädels Sonia und Stef, die mit ihrer wunderbaren Hingabe ganz viel Leichtigkeit in mein Leben gebracht haben. Tausend Dank für all Eure Unterstützung abseits der Physik. Ich bin unendlich dankbar, dass es Euch gibt!

Ich möchte mich bei meiner Familie für all die Unterstützung, seit schon immer, bedanken. Bei meinen Eltern, Doris und Suheil, die immer an mich geglaubt haben und jede noch so bescheuerte Idee unterstützt haben. Bei meinem Bruder Liam, der mich seit Jahren zu Höchstleitungen antreibt. Ohne Euch wäre das alles überhaupt nicht möglich gewesen.

Das Beste zum Schluss! Ein ganz besonderer Dank geht an Stefan. Ohne Dich, und Deine blöden Wortwitze, wäre ich schon längst verrückt geworden. Danke für Dein Verständnis, Deine unendliche Unterstützung und Deine Hilfe in den letzten Wochen, Monaten und Jahren and thank you for making me food so I don't die! Ich kann mir niemand besseren an meiner Seite vorstellen.

Diese Arbeit wurde durch den Helmholtz-University Young Investigator Grant Nr. VH-NG-825 und von der Deutschen Forschungsgemeinschaft durch den SFB 1245 (Projektnummer 279384907) unterstützt.

Die Simulationen wurden auf dem Lichtenberger Hochleistungsrechner der TU Darmstadt (Project ID: 646) und auf dem Cluster der Arbeitsgruppe, gefördert durch den European Research Council Grant No. 677912 EUROPIUM, durchgeführt.

Ich bedanke mich bei Sean Couch (FLASH) und Evan O'Conner (GR1D) für das zur Verfügung stellen ihrer Codes! Außerdem bei Evan für all seine open-source Routinen zu EOS Tabellen. Und inspiriert durch Alex Bartl: Danke an die open-source Community, die wunderbare Dinge wie Python und Latex möglich machen, und natürlich an alle Menschen, die wichtige Fragen auf stackoverflow gestellt und beantwortet haben.

> "Remember to look up at the stars and not down at your feet. Try to make sense of what you see and wonder about what makes the universe exist. Be curious. And however difficult life may seem, there is always something you can do and succeed at. It matters that you don’t just give up."
>
> – Stephen Hawking

Curriculum Vitae

Hannah Yasin

May 8th, 1990	Born in Frankfurt am Main, Germany
July 8th, 2009	Abitur, Ziehenschule Frankfurt, Germany
2009 - 2013	Bachelor studies, TU Darmstadt, Germany
May 23rd, 2013	Bachelor's degree, thesis title: "Study of the neutrinosphere and electron fraction in neutrino-driven winds, jet-like supernovae and neutron star mergers"
2013 - 2015	Master studies, TU Darmstadt, Germany
July 31st, 2015	Masters's degree, thesis title: "Short gamma ray bursts triggered by neutrino-antineutrino annihilation"
2015 - 2018	Doctoral studies and member of the scientific staff, TU Darmstadt, Germany

Erklärung gemäß §9 Promotionsordnung

Hiermit versichere ich, dass ich die vorliegende Dissertation selbstständig angefertigt und keine anderen als die angegebenen Quellen und Hilfsmittel verwendet habe. Alle wörtlichen und paraphrasierten Zitate wurden angemessen kenntlich gemacht. Die Arbeit hat bisher noch nicht zu Prüfungszwecken gedient.

Darmstadt, den 11. Dezember 2019

(Hannah Yasin)